2-9-2018 10:30 AM

Direct Sheet Molding Compound process (D-SMC)

Atieh Motaghi, *The University of Western Ontario*

Supervisor: Dr. Andrew N. Hrymak, *The University of Western Ontario*

A thesis submitted in partial fulfillment of the requirements for the Doctor of Philosophy degree in Chemical and Biochemical Engineering

Abstract

The combination of highly crosslinked resin and long glass fiber reinforcement in direct sheet molding compound (D-SMC) provides the parts with high physical properties and low density suitable for large interior and exterior automotive applications. Different stages of D-SMC process including maturation zone and compression molding are studied using mathematical analysis, numerical simulation and experimental investigations.

An analytical analysis is used to calculate the pressure and velocity in the first section of maturation zone and then the permeability of fiber bundle is calculated by simulation and the agreement between the available empirical equation and simulation was obtained. The flow is simulated in the next section of maturation zone using Ansys CFX and it was found the interlocking chain belt plays an important role in impregnation of bundles with paste.

The microstructure of fiber glass bundles in compression is investigated in a flat plaque mold. Analyses of the bundle deformation, including bending and deformation of the tow shape, are done for the charge and specific sites within a square plaque part for 30 percent and 62 percent of initial charge mold area coverages. Microscopy and micro-computed tomography (micro-CT) of the samples clarify the microstructure of the bundles after flow. The bundles at the part edge and corner deform more than the bundles close to center of the mold in both initial charge cases. The bundles flatten at all positions and bundle bending is mainly observed at the corner. The tow width changes and tow deflections are higher in the samples of 30 percent mold area coverage. The micro-CT images show that the bundles keep their cohesion and stay straight within the middle of the flow path position, but bend at the edge of the mold. Mold filling simulation using Moldflow^{TM} (Autodesk) predict fiber tow orientation through the thickness using the reduced-strain closure (RSC) models for fiber distribution for 30 and 62 percent initial mold area coverage. The measured value of orientation from micro-CT images confirms the random orientation through the thickness, consistent with the RSC model.

The Carreau viscosity model explains the behaviour of the D-SMC paste. Another viscosity model for suspensions of high volume of planar randomly oriented glass bundles defines the flow behaviour in the process and is used to simulate a flow field. An open source CFD software

package of OpenFOAM solves the equation of mass and momentum along with the introduced viscosity model by the volume of fluid technique in the three dimensional system. The simulation results show the plug flow profile at all positions and times during the process. To study bundle movement and deformation during the process, it is assumed that regions of very high viscosity with the same dimension of bundles represent bundles at different positions of the mold. The results reveal that the bundles close to the edges and corners of the mold moved more than bundles in the middle and diagonal positions. Moreover, the velocity profile shows higher velocity at these locations. Experimentally, the red bundles are placed at different locations of the charge and track during the process. The calculated movement distances of the bundles at different locations from the experiment and the OpenFOAM simulation follow the same trends and therefore agree.

In D-SMC, there is a viscosity variation through thickness because of temperature gradient and glass bundle volume fraction variation. The charge is placed between two hot plates of mold which are then closed to squeeze the charge and filled the mold. The layers of charge close to the hot mold plates act as lubricant for layers of charge in center. Because of greater resistance of charge in the center to flow, the hotter lubrication layer may flow preferentially before core layers of charge. The simulation is run using Ansys Polyflow to study the preferential flow in D-SMC process. Several stacks of charges on top of each other are used for compression molding. The flow is simulated for two charges to investigate the evolution of interface during mold filling Images of cross sections from experimental samples are used to validate the simulation analysis.

Key words

Composite materials, fiber orientation, direct sheet molding compound (D-SMC), numerical simulation, OpenFOAM, Ansys CFX, Ansys Polyflow, Moldflow, micro computed tomography (μCT), Bird Carreau viscosity model, rheology

Acknowledgements

I would like to thank my supervisor, Dr. Andrew Hrymak, for his unwavering support and guidance. He encouraged me during every single step of my research, patiently supervised me during the thesis, gave me freedom to explore new ideas and providing me opportunities for scientific advancement and personal improvement.

I would like to thank my committee members, Dr. Wankei Wan and Dr. Kibret Mequanint for their time and advice and the examiners, Dr. Leonardo Simon, Dr. Jeffrey Wood, Dr. Paul Charpentier, Dr. Amin Rizkalla.

I would like to thank the Fraunhofer Project Center team for helping me producing my samples, Biotron for microscopy, Robarts research institute-Imaging lab and Center for Automotive Material (MARC) for micro computed tomography of the samples.

I would like to thank CBE administrative staff, IT help desk people for the welcoming and friendly environment. I would like to thank my friends in Dr. Hrymak's research group and my office and engineering department for all the talks and support and motivation.

My parents are always my role models in my life. Thanks for their constant support and deep love. Thanks to my sister and brother. Most importantly, I must thank to my husband, Roozbeh, for his enduring patience, understanding, support and love and my little daughter, Yana.

Table of contents

Abstract i

Acknowledgements iii

List of Tables vii

List of Figures viii

Nomenclature xiii

1 Introduction and literature review 1

1.1 Direct sheet molding compound (D-SMC) 1

1.2 Formulation 4

1.3 Impregnation 5

1.4 Compression molding of sheet molding compound 6

1.5 Simulation of compression molding of glass fiber filled polyester SMC 8

1.6 Rheology of fiber filled suspensions 10

1.7 Fiber orientation in polymer processing 13

1.7.1 Folgar-Tucker model 14

1.7.2 Reduced strain closure (RSC) model 15

1.8 Thesis objectives 16

1.9 Thesis Outline 16

1.10 References 17

2 Maturation zone study 23

2.1 Objective 23

2.2 Flow study of material between rolls 25

2.2.1 Simplified flow theory 25

2.2.2 Velocity and pressure profile 27
2.3 Permeability 29
2.3.1 Image analysis 29
2.3.2 Mathematical model of flow into the bundle 29
2.3.3 Result of permeability studies 31
2.4 Flow study in the maturation zone 34
2.4.1 Simulation 34
2.4.2 Result of maturation zone simulation 34
2.5 Conclusion 35
2.6 References 35
3 Microstructure Characterization in Direct Sheet Molding Compound 37
3.1 Abstract 37
3.2 Introduction 38
3.3 Material and process 39
3.4 Characterization of the microstructure 40
3.4.1 Fiber orientation through the thickness 41
3.4.2 In-plane orientation 42
3.4.3 Deflection, fiber width and length 43
3.4.4 Micro computed tomography 44
3.5 Moldflow simulation 44
3.6 Result 45
3.7 Conclusions 57
3.8 References 58
4 Simulation of Compression Molding of Direct-Sheet Molding Compound 60
4.1 Objective 60

4.2 Simulation 61
4.2.1 Methodology 61
4.2.2 Geometry generation and mesh 62
4.2.3 Boundary conditions 63
4.2.4 Constitutive equation 63
4.3 Results for compression molding 66
4.4 Simulation of single bundle deformation in the flow 70
4.5 Results for simulation of single bundle 73
4.6 Experimental validation 73
4.7 Flow patterns in the sheet cross section 75
4.8 Conclusion 76
4.9 References 77
5 Simulation of flow through the thickness direction in DSMC 79
5.1 Objective 80
5.2 Modelling 80
5.2.1 Mathematical modeling 80
5.2.2 Constitutive equation 81
5.2.3 Boundary condition 81
5.2.4 Computational domain and discretization 83
5.2.5 Boundary condition 84
5.2.6 Finite element algorithm 85
5.3 Experimental procedure 85
5.3.1 Material and process 85
5.3.2 Simulation result 86
5.3.3 Experimental result 90

5.4 Conclusion 93
5.5 References 94
6 Conclusion and recommendations 96
6.1 Conclusions 96
6.2 Recommendations for future work 97
Appendix A 99
Appendix B 104

List of Tables

Table 1-1 Difference of SMC and D-SMC process 4

Table 2-1 Parameters used for analysis 27

Table 2-2 Bundle properties..... 29

Table 2-3 Permeability values form simulation and equation 33

Table 3-1 Formulation of D-SMC paste 40

Table 3-2 Parameters for the viscosity model [22]..... 45

Table 3-3 Parameters for the kinetic model [22] 45

Table 3-4 Microstructure parameters measured for charge and sheet at for 62 percent initial mold area coverage 49

Table 3-5 Microstructure parameters measured for charge and sheet at for 30 percent mold area coverage 49

Table 4-1 Formulation of D-SMC paste 65

Table 4-2 Parameters of viscosity model..... 66

Table 4-3 Coordinates of points of interest..... 67

Table 5-1 Parameters of viscosity model..... 83

List of Figures

Figure 1-1 Schematic view of D-SMC process [2]..... 3

Figure 1-2 Compression force applied during compression molding [16]..... 7

Figure 1-3 Squeeze flow pattern a) shear like flow profile b) plug like flow profile 8

Figure 1-4 Steady shear viscosity of SMC of unsaturated polyester versus shear rate for different temperature [38] 11

Figure 1-5 Schematic view of the shear deformation of the suspensions [43] 12

Figure 2-1 Maturation zone a) deaeration unit b) impregnation unit 24

Figure 2-2 Heating and cooling unit 24

Figure 2-3 Notation for analysis of flow 25

Figure 2-4 Pressure profile over the x-direction 28

Figure 2-5 Velocity vectors in the analysis region 28

Figure 2-6 Simulation domain for bundle 30

Figure 2-7 Images of single bundle 31

Figure 2-8 Images of cross section of different bundles in the charge 32

Figure 2-9 Velocity vs. pressure gradient over viscosity 33

Figure 2-10 Geometry of rollers and compound a) compound flow region 34

Figure 2-11 Velocity and strain rate in the flow domain 35

Figure 3-1 Schematic view of D-SMC process 40

Figure 3-2 Positions of samples in the sheet; D: diagonal, M: middle, E: edge, C: corner, positions of the initial charge (30 percent mold area coverage (– – – –) , 62 percent mold area coverage (– · – · –) 41

Figure 3-3 Processed image for the measurement of orientation 42

Figure 3-4 a) Stitched image of corner sample b) measured parameters of $aij, li, Ri,$ φ to quantify the fiber bundle. 43

Figure 3-5 Overview of the bundles in charge 46

Figure 3-6 Overview of sample cross section 47

Figure 3-7 First component (x-x) of local fiber bundle orientation through the thickness at position M, where x and y are the planar directions and z is the thickness direction. 47

Figure 3-8 Second component (y-y) of local fiber bundle orientation through the thickness at position M, where x and y are the planar directions and z is the thickness direction. 48

Figure 3-9 Micro CT of the E sample for 62 percent of initial mold area coverage (voxel size of 20 μ) 50

Figure 3-10 Micro CT of the M sample for 62 percent of initial mold area coverage (voxel size of 50 μ) 51

Figure 3-11 Average cure over time 52

Figure 3-12 First component of fiber orientation for sample M of 62 percent of initial mold area coverage 53

Figure 3-13 First component of fiber orientation for sample M of 30 percent of initial mold area coverage 54

Figure 3-14 First component of fiber orientation for sample D of 62 percent of initial mold area coverage 54

Figure 3-15 First component of fiber orientation for sample D of 30 percent of initial mold area coverage 55

Figure 3-16 First component of fiber orientation for sample E of 62 percent of initial mold area coverage 55

Figure 3-17 First component of fiber orientation for sample E of 30 percent of initial mold area coverage 56

Figure 3-18 First component of fiber orientation for sample C of 62 percent of initial mold area coverage 56

Figure 3-19 First component of fiber orientation for sample C of 30 percent of initial mold area coverage 57

Figure 4-1 Schematic of mold geometry and position of the initial charge..... 62

Figure 4-2 Shear viscosity of D-SMC paste 65

Figure 4-3 Points of interest in the sheet; D: diagonal, M: middle, E: edge, C: corner, positions of the initial charge (30 percent mold area coverage (— · —) , 62 percent mold area coverage (— — —), middle line (----) 66

Figure 4-4 b) Resulting charge edge at 1.2s from 62 percent mold area coverage, d) resulting charge edge at 6.8s from 30 percent mold area coverage..... 67

Figure 4-5 Velocity for 62 percent initial mold area at different positions after 1.2 seconds 68

Figure 4-6 Velocity profile for 62 percent initial mold area coverage through the thickness at M and D positions 68

Figure 4-7 Velocity profile for 30 percent initial mold area coverage at different positions after 1.2 seconds..... 69

Figure 4-8 Velocity profile for 30 percent initial mold area coverage through the thickness at M and D positions 69

Figure 4-9 Compression molding pressure versus strain rate..... 70

Figure 4-10 Single bundle movement in the mold with 5mm thickness a) initial position b) after 1.2 s c) velocity (m/s) at 1.2s..... 72

Figure 4-11 Single bundle movement in the mold with 5mm thickness and symmetry boundary condition a) initial position b) after 1.2s c) velocity (m/s) at 1.2 s 72

Figure 4-12 a) Initial positions of bundles b) After 0.5s c) After 1.2 s 73

Figure 4-13 Bundle positions a) before compression b) after compression for 62percent mold coverage 74

Figure 4-14 Travel distance of bundles at different locations (cm) 75

Figure 4-15 Cross section of the sheet a) two stacks of charges 62 percent initial mold area b) four stacks of charges 30 percent initial mold area (the flow is from the center of mold (left) to end of cavity (right) 76

Figure 5-1 Shear viscosity of paste as a function of shear rate 82

Figure 5-2 Shear viscosity of paste including 20 percent GF as a function of shear rate 82

Figure 5-3 Finite element mesh of computational domain a) two charges with different viscosities b) core charge with two layers of paste on top and bottom 84

Figure 5-4 Isothermal flow over time for core charge with two layers of paste on top and bottom 87

Figure 5-5 Flow and temperature development over time for core charge with two layers of layer of paste on top and bottom 88

Figure 5-6 Isothermal flow development for two layers of charge with paste layer and paste with GF layer 89

Figure 5-7 Temperature and flow development for two layers of charges with paste layer and paste with GF layer 90

Figure 5-8 8 Images of cross section from 30 percent mold area coverage and segmented charge at different positions (1, 2, 3, 4 are images at the positions of right-hand side sheet) 91

Figure 5-9 Images of 30 percent initial mold area coverage and layered with two layers of colored charges on top of two layers of non-colored charges at different positions (1a, 1b, 2a, 2b are images at the positions of right-hand side sheet) 91

Figure 5-10 Images of 30 percent initial mold area coverage and layered with one layer of colored charge on top of one charge of non-colored charge (4 charges in total) at different positions (1a, 1b, 1c are images at the positions of right-hand side sheet) 92

Figure 5-11 Images of 62 percent initial mold area coverage and layered with one non-colored charge on top of one colored charge at different positions 93

Figure 5-12 Microscopy of cross section of charge close to the upper and lower surface 93

Nomenclature

a = minor axis of bundle

a^* = dimensionless average width of bundle

a_{i0} = bundle width in the charge

a_{ij} = bundle width in the sheet

a_{xx} = component of orientation tensor

$\mathbb{A}$ = forth order orientation tensor

A = fiber orientation tensor

$\boldsymbol{A}$ = constant value

A_{fiber} = fiber cross section area

A_{bundle} = bundle cross section area

A_i = frequency factor

b = major axis of bundle

$\boldsymbol{B}$ = constant value

c = concentration

C_I = fiber-fiber interaction coefficient

c_1 = model parameter

c_2 = model parameter

C_p = specific heat

d = fiber diameter

D = strain rate tensor

E_a = activation energy

f = distribution function

f_α = interfacial tension force

f_c = contact force

g = gravity

H_0 = nip distance

h = distance between rolls

H = heat of reaction

k_f = friction coefficient

k_h = hydrodynamic coefficient

k = thermal conductivity

k_p = penalty coefficient

K = permeability tensor

l = fiber length

$\mathbb{L}$ = eingenvectors of orientation tensor

l_i = visible length of bundle

$\mathbb{M}$ = eigenvalues of orientation tensor

m_α = kinetic exponent

n = parameter of Carreau Bird Model

N_f = number of fibers in the bundle

n_α = kinetic exponent

$n_{1\alpha}$ = exponent of viscosity model

P = pressure

P_n = packing stress

Q = flow rate

r = Radius of fibers

r_f = aspect ratio of fiber

R_r= rolls radius

R_i = curvature radius

R = universal gas constant

t = time

T = temperature

T_b = model parameter

$\boldsymbol{T}$ = stress tensor

u = velocity vector

u_c = compression velocity

u_{plate} = velocity of plate

U = roll speed

v_x = velocity in x direction

v_y = velocity in y direction

v_f = volume fraction of fibers in bundle

V_f = Glass bundle volume fraction

W = vorticity tensor

Greek letters

α = degree of cure

α_g = degree of cure at gelation

α_f = volume fraction of fluid

α_a= volume fraction of gas

α_η = average shearing thickness

$\dot{\gamma}$ = shear rate

δ^* = deflection

ϵ = bundle porosity

η = viscosity

η_∞ = viscosity at shear rate of infinity

η_0 = zero shear viscosity

η_f = viscosity of fluid

η_a = viscosity of gas

θ^* = absolute temperature

θ_α^* = absolute reference temperature

θ = out of plane angel

ι = dimensionless parameter

κ = paramter of RSC model

λ = parameter of Carreau Bird Model

ξ = shape parameter

ρ = density

ρ_f = density of fluid

ρ_a = density of gas

ς = dimensionless parameter

τ = model parameter

φ = in plane orientation angel

Υ = dimensionless parameter

1 Introduction and literature review

1.1 Direct sheet molding compound (D-SMC)

The D-SMC process was developed by the Fraunhofer Institute for Chemical Technology and commercialized by Dieffenbacher. The process eliminates the several days' maturation period required for conventional sheet molding compound (SMC) and reduces cycle time of production. The continuous nature of the D-SMC process guarantees a high and constant quality of products compared to the batch process of conventional SMC. In SMC, the preform is wrapped and stored for certain amount of time for thickening (e.g. 1-2 weeks) before use in compression molding [1]. The time and cost of storing the preforms in the D-SMC process are eliminated. D-SMC offers the possibility of real time control over the formulation and process. The main stages of D-SMC are mixing zone, maturation zone and compression molding as shown in Figure 1-1[1].

The process begins with automated dosing of the liquid raw ingredients (e.g. unsaturated polyester resin, low profile additive, peroxides). All the liquid ingredients are mixed in the twin screw extruder at room temperature. Solid ingredients (fillers such as calcium carbonate, thickening and release agent) are added gravimetrically from a side feeder into the extruder. The extruder mixes the liquid and solid ingredients to form a homogenous paste compound [2].

The paste is divided into two equal streams and transferred into doctor boxes as shown in Figure 1-1. The fiber bundles are cut from rovings and distributed across the width of paste layer. The sandwich of paste and fiber passes through a roller section for degassing and impregnation of the resin into the fiber tows, and consistent dispersion where fiber wet out takes place. The impregnated material then moves through a rapid-maturation zone where, in a temperature-controlled environment, the chemical thickening of the D-SMC material takes place within a few minutes. At the end of the maturation zone, the viscosity of mixture increases and then the D-SMC charge is cooled to ambient temperature. The material moves directly onto the automated numerically controlled (NC) cutting table, where it is cut into the required charge pattern and subsequently laid up to form the charge load for the compression molding process [2].

Either manual transfer or a robot picks up the charge and places it in the open tool of a compression-molding press, which then closes and molds the part. Depending on the sheet width, throughput and material formulation, the complete cycle — from compounding through molding — can take as little as 20 minutes[2].

The main features of the D-SMC process are [1, 2];

- Very high efficiency because of lowest possible material costs
- Improved surfaces of the formed parts (class A surface)
- Short cycle time
- Excellent process capability
- Reduced wear on the press dies
- Fewer air inclusions and more homogenous filler dispersion
- No semi finish process
- No semi finish material maturation stage and transportation
- Flexibility in recipe of formulation
- High process stability
- Consistent high material quality

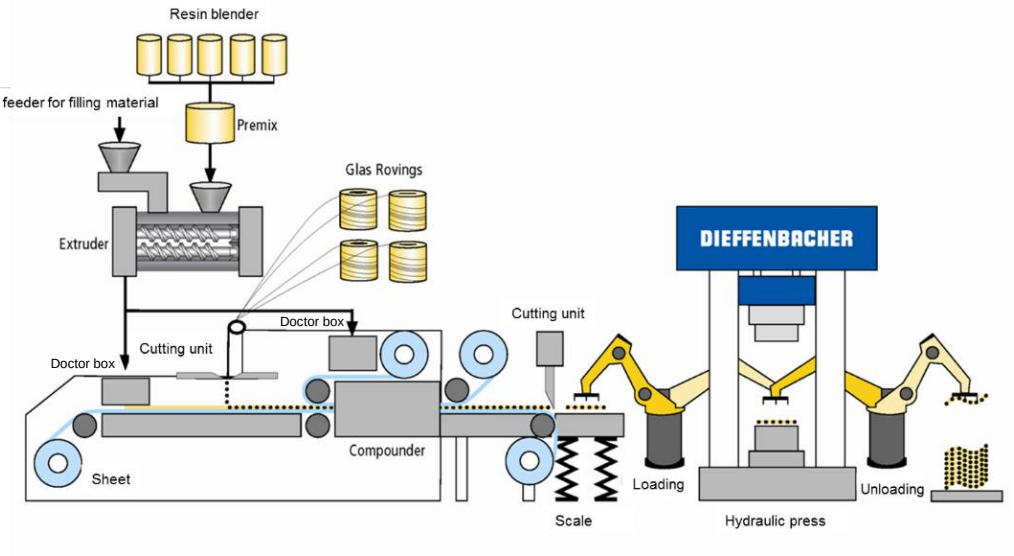

Figure 1-1 Schematic view of D-SMC process [2]

The several maturation periods required by SMC is eliminated in D-SMC. With D-SMC the lengthy interval between compounding raw materials and compression molding can be shortened to minutes. D-SMC is continuous process compared to the SMC process which is batch process. Due to close loop nature of D-SMC process, a high and constant level of quality can be guaranteed that is more challenging in conventional SMC [2].

The scrap in D-SMC process is reduced which has a positive effect on final product costs. Also, the time and cost of storing material for maturation are eliminated because there is no need to wait for material to mature. D-SMC provides the greater flexibility in terms of raw material selection and get close to real time control over formulation changes. The compound consistency is greater in D-SMC material compared to SMC material because of the twin screw extruder is more effective than mixers in conventional SMC. D-SMC provides the opportunity to increase the fiber volume fraction for demanding application. Also, microscopy of D-SMC products shows fewer air inclusion and finer and more homogenous filler dispersion than conventional SMC products [2]. The main differences of SMC and D-SMC are available in Table 1-1 [1, 2].

Table 1-1 Difference of SMC and D-SMC process

	SMC	**D-SMC**
Process	Batch	Continuous
Formulation	--------	More thickening agent is needed.
Cycle time	1-2 weeks	20 minutes
Preparation	Semi finish material during maturation stage and transportation	No semi finish material during maturation and transportation
Preparation	Storing and maturation are needed.	------
Properties	-----	Fewer air inclusions and more homogenous fiber dispersion
	------	Higher amount of fibers can be added.

1.2 Formulation

The combination of highly crosslinked resin and long glass fiber reinforcement in direct sheet molding compound (D-SMC) and sheet molding compound (SMC) provides the parts with improved strength, stiffness, heat resistance and dimensional stability. SMC and D-SMC offer a great application in automotive industry because of high strength to weight ratio, corrosion resistance and low cost. Unsaturated polyester (UP) is one of the most commonly used thermoset resins for SMC and D-SMC. This material has good strength which is required in many demanding applications [1,3]. Approximately, 75 percent of all resins used for formulation is polyester [3]. The most common type of reinforcement in the SMC and D-SMC industry is glass fibers. They offer dimensional stability and good mechanical properties. Normally, glass fibers are in the form of individual bundles and in the range of 25-35 weight percent of SMC/D-SMC. The glass bundles are randomly distributed in the plane of the sheet. The role of the fillers is necessary for the improvement of properties such as chemical and heat resistance, dimensional stability, hardness, surface smoothness and shrinkage. Calcium carbonate is the most common filler in the range of 60-65 weight percent of the paste formulation. Low profile additives (LPA), which are thermoplastic, control shrinkage during the curing process and provide good surface appearance. The amount of LPA used in formulations is typically 2-15 weight percent. Thickening agent is used to increase the viscosity, typically in the range of 0.5-3 weight percent which is necessary for

handling the SMC/D-SMC charge and fiber displacement during molding. Too low a viscosity causes the resin to flow ahead of fibers, and too high a viscosity reduces wet out of the fiber bundles. Thickening agents include magnesium oxide (MgO), magnesium hydroxide, and calcium oxide. The thickening agent increases the viscosity up to 10^5 Pa.s as a result of chain extension by a condensation reaction between the metal oxides and carboxylic acid groups of unsaturated polyester. Han et. al. shows that the zero shear viscosity for unsaturated polyester/MgO mixture increases in thickening period after 450 hour [4]. Other additives such as initiators, mold release, pigments and stabilizers are also used in SMC formulations [1].

1.3 Impregnation

Permeability of fibrous media is a key characteristic of composite manufacturing. The degree of impregnation of a fiber bundle has a significant influence on the quality and performance of final product. In SMC and D-SMC, one layer of randomly dispersed chopped fiber bundles is pressed between two layers of paste.

The permeability of fibrous media is a quality which relates the local velocity of fluid flow to the pressure gradient. In flow perpendicular to the plane of reinforcement either chopped bundles or mat as in SMC and RTM, the permeability can be calculated using the Darcy's law:

$$\langle u \rangle = \frac{K}{\mu} . \langle \nabla p \rangle \qquad (1\text{-}1)$$

In which μ is viscosity of the fluid, p and u are the pressure and average velocity of fluid, respectively. Parameter K is permeability tensor of porous medium which has dimension of m^2 [5].

It is often impossible to determine the analytical expression for permeability of inter tow region because of complex path of flow in this region. One of the most popular approaches in numerically prediction of permeability is solving the Stokes equation and substituting the resulted velocity and pressure gradient from Stokes equation in Darcy equation [6–11]. Within approach, the permeability was obtained for woven fabric preform [6], textile [8,11], thermoplastic yarn [9].

Papathanasiou simulated the permeability for the unit cell containing square packing of fibers inside its perimeter [7,10]. The unit cell was characterized by two porosities: an inter-tow porosity, determined by macroscopic spatial arrangement of tows and intra-tow porosity, determined by

fiber arrangement and concentration inside each tow. It was found that with increasing number of fibers (>37), the intra-tow porosity approached a plateau and consequently the predicted permeability became independent of the number of fibers. Also, the effect of intra-tow porosity on permeability was very significant when inter-tow porosity was low (less than 0.4). At high values of inter-tow porosity the effect was negligible and tow behaved effectively as an impermeable tow and the fluid preferentially flowed around the bundle [7].

Merhi et al. [12] experimentally showed that at the same volume fraction of bundles, the permeability is higher for the bundles with lower volume fraction of fibers. Glass mat thermoplastic (GMT) fabrics exhibit higher permeability than SMC bundles, because bundle in GMT fabrics orients in flow direction which enhanced permeability. Also permeability follows the empirical power law model [9,12]. Shih and Lee [13] also measured the permeability of several glass fiber mats with different fiber architectures. They concluded that the size of the pores outside the fiber twos and the connections between pores plays and important role in determination of the permeability of fibrous media.

Gebart [14] developed equations for transverse local permeability of intratow region of both hexagonal and quadratic arrangement of fibers in tow.

$$K_{hex} = \frac{16}{9\pi\sqrt{6}}\left[\sqrt{\frac{\pi/(2\sqrt{3})}{V_f}-1}\right]^{5/2} R^2 \qquad 1\text{-}2)$$

$$K_{quad} = \frac{16}{9\pi\sqrt{2}}\left[\sqrt{\frac{\pi/4}{V_f}-1}\right]^{5/2} R^2 \qquad 1\text{-}3)$$

Where V_f is volume fraction of fibers and can be defined $(1-\epsilon)$ and ϵ is porosity. R is the radius of the fiber, respectively. These equations are widely used to determine the permeability of intra-tow fibrous media in woven fabrics, aligned fiber, textile reinforcement [6,15,16].

1.4 Compression molding of sheet molding compound

The SMC/D-SMC preform or charge typically has a thickness of 2-6 mm with uncured resin. The cut charge(s) are placed in a hot mold and covers 30 to 70 percent of the mold surface area. The applied pressure on the charge starts by closing the mold and drives the charge to fill the mold.

Complete crosslinking occurs in the mold over time under pressure and heat. Then, the part is ejected from the open mold and the cycle starts over, as shown in Figure 1-2. When $t \leq t_f$, the force increases because of squeezing and heating the charge. At t_f, the charge is pushed to flow into the cavity and at t_c the mold filling is finished and compression of the charge happens to compensate the volume change due to the crosslinking reaction [17].

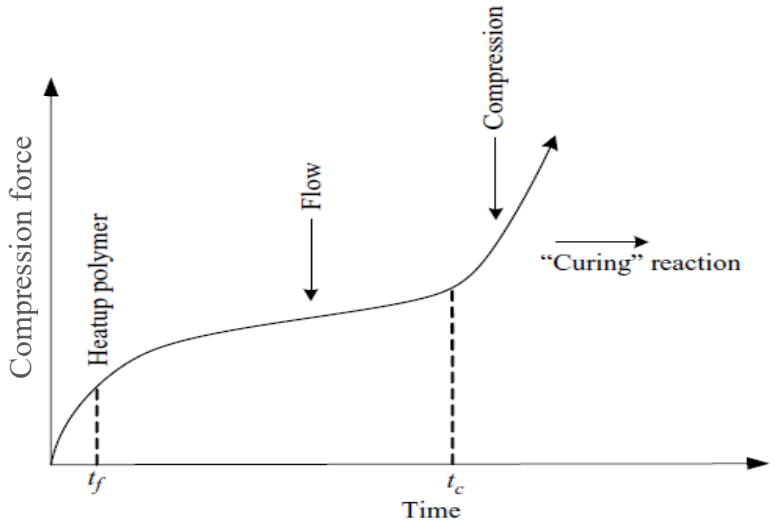

Figure 1-2 Compression force applied during compression molding [16]

The molding cycle time includes mold filling and curing reaction. The filling time is relatively short, compared to curing time . The governing parameters in these two regions are different. The curing reaction is governed by the thermal history, while filling is mainly governed by flow history. The structural properties of the SMC products are developed through the complete cure of the resin.

When a material is squeezed between two parallel plates, the pressure drives the material to flow in the plane of the mold direction [18–20]. Such a flow pattern is similar to compression molding of SMC and as the plate is moving down, there are gradients of velocity in all directions [18]. Figure 1-3 shows two extreme cases during squeeze flow: shear velocity profile and plug flow profile. The shear profile is a result of the assumption of no slip at walls. Plug flow occurs when the material is assumed to completely slip at the walls [20]. The complexity of squeezed flow of SMC is a result of rheological properties, generation of microstructure, curing of the resin, and thermal and flow boundary conditions between resin and mold [21].

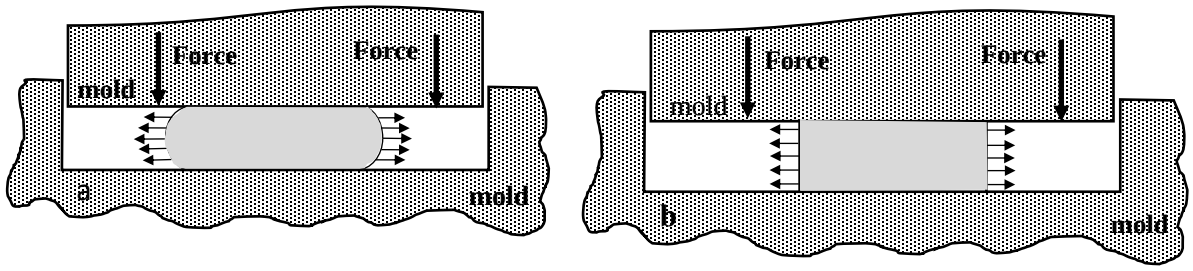

Figure 1-3 Squeeze flow pattern a) shear like flow profile b) plug like flow profile

1.5 Simulation of compression molding of glass fiber filled polyester SMC

All simulations conducted for studying flow in compression molding begin from the governing equations of motion, continuity and energy. One of the most commonly used models is the generalized Hele-Shaw model, which describes the flow in compression molding process [3,22–26]. The boundary conditions for the generalized Hele-Shaw model are as follows: the derivative of pressure is zero ($\frac{\partial P}{\partial n} = 0$) at the mold walls and zero pressure at the free flow front [22,26]. The following assumptions are used:

- The thickness of mold is much smaller than the other dimensions. The mold thickness is changes slowly as a function of x and y.
- The molding compound is incompressible and isotropic.
- The viscosity of the fluid is a function of strain rate, temperature and degree of curing. Viscoelastic effects and normal stress effects are negligible.
- There is a no slip boundary condition at the surfaces of the mold.
- There is no leakage at the mold edges.

The equations were solved for isothermal Newtonian and power law fluids with the power law exponent of 0.2 and 0.4. The shape of charge was compared to the experimental data for 30 percent by weight of GF filled polyester SMC, which was molded isothermally, with good agreement [22].

Barone and Caulk [27] visualized the flow in compression molding by using black and white layers of SMC (polyester/30 weight percent of GF), and by inserting the white charge within the black charge (segmented charge). At a closing speed of mold (10mm/s), the layers extend uniformly with no relative motion between the layers. At a slower closing speed (1.75 mm/s), the layers close to the mold surface move faster than the core layers. This preferential flow of upper

and lower layers adjacent to the mold surfaces is diminished in thinner charges (3 layers). In the case of the segmented charge and fast closing speed (10 mm/s), the boundary between the white and black charges confirm uniform extension and slip at mold surfaces, similar to the layered experiment. But at the slower closing speed of 1.75 mm/s, preferential flow at the center of charge is observed, which might be related to pre-mature gelation in the region close to the hot mold surfaces. Similarly, Odenberger et al. [28] observed the preferential flow of upper and lower layers for GF filled polyester SMC at a relatively low speed of mold closing (2mm/s) and preferential flow at the top and bottom layers, which is similar to the observation by Barone and Caulk [27,29] for high speed closing mold.

Lee et al. [30] simulated the compression by the two dimensional equations of motion, continuity and energy. Fluid behaviour is assumed to be incompressible and isotropic. The equations are solved for non-isothermal Newtonian and power law fluid with Arrhenius dependency on the temperature. The parameters of the Newtonian and power law model are obtained from fitting the data for polyester charge of SMC and the value of zero shear viscosity double to approximate the effect of fibers. The result shows that the velocity profile is flat, except for the thin layer at the mold surface. Because the top layers of charge are in contact with the hot surface of the mold, the viscosity is reduced resulting in a shear rate profile. The velocity profile shows the planar extensional deformation. The velocity plot at later time near the end of squeezing process shows that shear region is thicker as the heat penetrates farther. Also, the velocity profile is flat and there is a little fountain flow at flow front. The result for thick charge (6 layers) of power law fluid is similar to the Newtonian fluid except formation of preferential flow near the mold surfaces.

The phenomenon of fountain flow refers to simple shear flow behind the melt front that is transferred to the combination of shear and extensional flows as a hot fluid element from the core area moves toward the mold wall and subsequently solidifies. Mavridis et al. [31] simulated the fountain flow in compression molding of thermoplastic. The temperature of the mold surfaces is less than the fluid element, which causes the movement of flow to slow and solidification at the surface. In molding of thermoplastics vitrification occurs by cooling. The high initial thickness allows for the variation of flow front velocity which intensifies the fountain effect [31]. But, in the Barone and Caulk work, the temperature of the mold is more than the SMC charge which causes

the preferential flow at the surfaces especially at slow closing speed [27]. Vetrification of SMC occures by cure reaction which is triggered by high temperature and pressure.

1.6 Rheology of fiber filled suspensions

When a suspension of rigid fibers flows in suspending medium, the rheological behavior can be controlled by either matrix fluid or both coupling matrix fluid and fiber orientation evolution. The presence of fibers highly affects the rheology, fiber orientation and flow field. In a homogenous flow field with randomly oriented fibers, all fibers experience the same shear rate as fluid shear and flow field remains unchanged. In the case of non-homogenous flow and pressure flow between parallel plates, the fibers near the wall reorient faster because of the higher shear rate compared to the center line. Therefore, the rheological properties changes and leads to non-parabolic velocity profile.

The shear and extensional behavior of glass mat thermoplastic (GMT) under compression molding was examined by Dweib [32]. The shear and extensional viscosities are derived from a simplified equation of motion with no slip at the wall and power law model for the fluid. Both shear and extensional viscosities are a function of mold geometry, closing speed, GF content and power law parameters [32,33]. Thattaiparthasarthy et al. [33] examined the effect of temperature, fiber length and content on the viscosity of E-glass reinforced polypropylene by using the same approach of Dweib [32]. It is concluded that the fiber content has a more significant effect on shear viscosity than any other parameters such as temperature and fiber length for E-glass/PP system. The effect of fibers on shear viscosity is consistent for thermoplastics and polyester [30,32,33,38].

Thomasset et al. [34] and Ausias et al. [35] proposed the model to describe the shear viscosity considering the effect of fiber content and orientation. The agreement between prediction and experiment for polypropylene containing 20 volume percent GF is reasonable. In this approach, the modeling is based on the dilute suspension in a Newtonian fluid at low shear rate which is far from the realistic situation [35]. Moreover, the interaction between the fibers is ignored which plays an important role in the orientation and rheological properties.

Guo et al. [36] modeled the viscosity of low density polyethylene (LDPE) containing a range of volume fraction of E-GF. Viscosity is the result of contribution of the matrix and fiber. The result reflects the fact that effect of fiber volume fraction and orientation have a diminishing effect

at high shear rate. Their result is also consistent with the modeling done by Ramazani et. al [37] which the fiber matrix interaction have an important effect on shear viscosity of GF reinforced polydimethyl siloxane. Their model also predicts an increase in shear viscosity with increasing the amount of GF and fiber-fiber interaction over the whole range of shear rates.

Lee et al. [38] reported that the shear viscosity of polyester paste of SMC charge without GF could be fitted to the Carreau model (Figure 1-4).

$$\frac{\eta_s - \eta_\infty}{\eta_{0-}\eta_\infty} = [1 - (\lambda\dot{\gamma})^2]^{(n-1)/2} \quad (1\text{-}4)$$

η_0 and η_∞ are the zero shear and infinite viscosities, and λ is the time constant, and n is the power law index.

Their results show that zero shear viscosity, η_0, obey Arrhenius relationship. The paste viscosity, η, is temperature dependent and follows the Arrhenius equation;

$$\eta = \eta_0 e^{\left[\alpha\left(\frac{1}{\theta^*} - \frac{1}{\theta_\alpha^*}\right)\right]} \quad (1\text{-}5)$$

where subscript * represents the absolute temperature scale in Kelvin degree and η_0 is the viscosity at reference temperature θ_α^* , while α is the activation energy [21,38–40]. Lecorre et al. [39] fitted the viscosity of SMC compound to obtain the activation energy.

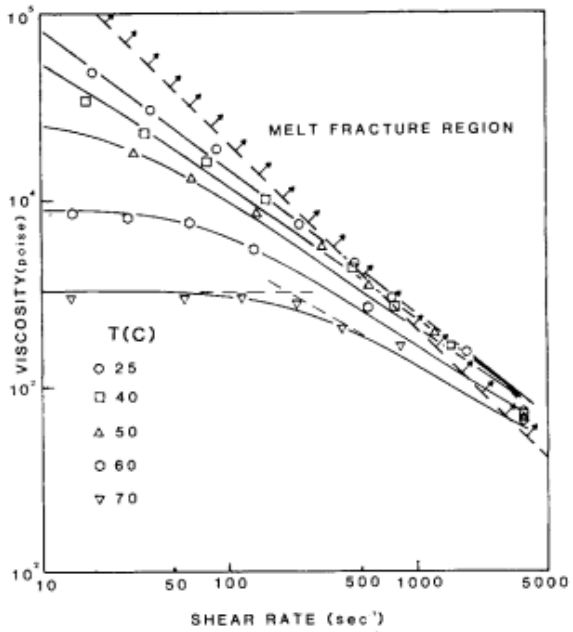

Figure 1-4 Steady shear viscosity of SMC of unsaturated polyester versus shear rate for different temperature [38]

Le Corre et al. [39] also reported that compression and shear viscosities follows the power law behavior for the GF reinforced polyester. Such behavior is reported before the cure reaction started. Their results indicate that the power law exponent (n) was independent of temperature and GF content. Similar to the previous research, the same trend of changing viscosities with temperature and fiber content is observed [32,33]. The shear viscosity is less affected by fiber volume fraction than compression viscosity, which leads to enhanced anisotropy with increasing fiber content.

Dumont et al. [41] also reported power law relationship for the GF reinforced polyester under both simple compression and plane compression molding. Interestingly, the same power law exponent (n=0.44) is reported for plane and simple compression as for shearing [39]. Also, all viscosities are fitted to the second order polynomial function of fiber volume fractions [41]. Similarly, Abrams et al. [42] obtained the forces during the compression using the power law model. The power law exponent of 0.43 is reported for 25 volume percent GF low profile SMC. The assumption of isotropic and power law model is also used by Lee et. al. [30] for simulation of compression molding of fiber reinforced polyester.

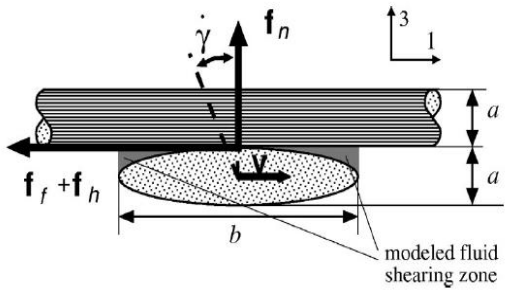

Figure 1-5 Schematic view of the shear deformation of the suspensions [43]

The rheology of the highly planar randomly oriented bundles' suspensions is a result of interaction mechanism at bundles contact points. The interaction forces are the sum of friction (F_f) and lubrication (F_h) at contact points (Figure 1-5). The proposed model for the viscosity η is

$$\eta = \frac{k_f P_n}{\dot{\gamma}} + k_h \frac{16}{\pi^2}\frac{a}{b^2\alpha} f \phi_b^2 \eta_0 \left[1 + \left(\lambda \frac{a}{\alpha}\dot{\gamma}\right)^2\right]^{\frac{n-1}{2}} \quad 1\text{-}6)$$

where $\dot{\gamma}$ is the shear rate and, P_n is the normal packing stress. The first term on the right hand side of the equation represents the frictional force where k_f is the friction coefficient. The second term represents the hydrodynamic lubrication force where k_h is the coefficient of hydrodynamic

lubrication and α is the average shearing thickness of the compound around the contacting bundles. The constants of η_0, λ and n are Carreau parameters of the paste. ϕ_b is the volume fraction of bundles in the compound. The parameter f is a distribution function of in-plane bundle orientation, and its value is 0 for perfect alignment and $^2/_\pi$ for in-plane random orientation [43]. The proposed rheology model includes the yield stress at low shear rate and a power law behavior at high shear stress. Thomasset et. al also reported a yield stress for shear viscosity of compounds of long fiber composites [34].

The above model is based on the assumption that the bundles contain a uniform number of fibers, which are dispersed uniformly in the system. Servais et al. experimentally showed that bundles deform at lower normal packing stress and have a uniform deformed cross section with the minor axis, a, and major axis, b. Another assumption is that flow does not affect the fiber cross section and volume fraction of bundles. The stress direction is perpendicular to the minor axis, and bundles cannot rotate about their own axis because of the resistance at the available contact points through the length. Moreover, bundles are square packed and incompressible at the contact points [43]. The comparison of experiments and model shows that equation 1-6) overestimates the viscosities, which is attributed to the assumptions that ignores the fiber rotation and only sliding of the fibers is considered [43].

1.7 Fiber orientation in polymer processing

Prediction of fiber orientation began with Jeffery's equation [44]. The proposed equation is for dilute suspensions in which fibers do not interact with each other.

The fiber suspensions can be divided into three regimes based on the fiber volume concentration (c) and fiber aspect ratio $\left(\frac{l}{d}\right)$.

Dilute regime. In this region, suspension has sufficiently low concentration of fibers so that fibers can rotate without touching each other. Theoretically, the average distance between fibers is greater than the length of fiber. The constraint defined for this regime is $c < \left(\frac{l}{d}\right)^2$.

Semi-concentrated regime. In this regime, the rotation of fiber is restricted by other fibers. The regime is defined by $\left(\frac{l}{d}\right)^2 < c < (\frac{l}{d})$.

Concentrated regime. In this regime, the fiber rotation and movement can be severely affected by fiber-fiber interaction. Glass fiber composites used for industrial applications typically have fiber concentration in this regime. The constraint defined this regime is $c > (\frac{l}{d})$.

1.7.1 Folgar-Tucker model

Folgar and Tucker developed a model for fiber orientation based on Jeffery's model. They introduced a term that takes into account the interaction between fibers [45]. The following are the assumptions that were made to develop the model for prediction of second order of orientation tensor (a_{ij}) for high aspect ratio particles:

1. The fibers are rigid cylinders with uniform length and diameter.

2. The fibers are sufficiently large so that Brownian motion is negligible.

3. The center of mass of the particles are randomly distributed.

The equation is written as,

$$\frac{Da_{ij}}{Dt} = -\frac{1}{2}\left(W_{ik}a_{kj} - a_{ik}W_{kj}\right) + \frac{1}{2}\xi\left(D_{ik}a_{kj} + a_{ik}D_{kj} - 2D_{kl}a_{ijkl}\right) + 4C_I\dot{\gamma}\left(\delta_{ij} - \alpha a_{ij}\right) \quad (1\text{-}7)$$

With $\boldsymbol{\alpha}$ equal to 3 for three-dimensional and 2 for two-dimensional orientation. In equation (1-7), W_{ik}, D_{ik} and C_I are vorticity, strain rate tensor and fiber-fiber interaction. Parameter of ξ is a shape parameter and constant and function of particle aspect ratio (r_f)

$$\xi = \frac{{r_f}^2 - 1}{{r_f}^2 + 1}. \quad (1\text{-}8)$$

To approximate the fourth order orientation tensor, a_{ijkl}, the closure approximation is used to relate the fourth order orientation tensor to the second order orientation tensor (a_{ij}). The most commonly used approximations are: linear closure, quadratic closure and the hybrid closure [46–48]. The most popular one is hybrid and quadratic closure approximation [36,47,49–51].

The experimental result of Folgar and Tucker [40] shows the dependency of C_I on fiber aspect ratio and fiber volume fraction. Bay [52] suggested an empirical model for C_I,

$$C_I = 0.0184\ exp\ (-0.7148\ c\ \left(\frac{l}{d}\right)). \quad 1\text{-}9)$$

Phan-Thien et al. [48] also fitted a similar empirical model to experimental data.

$$C_I = A\ \left[1 - exp\ (-B\ c\ \left(\frac{l}{d}\right))\right] \quad 1\text{-}10)$$

The parameters of $\boldsymbol{A}$ and $\boldsymbol{B}$ are reported as 0.03 and 0.224, respectively [53]. The value of $\boldsymbol{C_I}$ may range between 0.01-0.0001 [45,52,53].

In simulation of fiber orientation, it is assumed that the flow field is not affected by the fibers (decoupled approach). The flow field is first obtained for the mold filling process with the rheological properties of matrix and processing condition [54–56]. Then, equation 1-7 is solved to obtain the fiber orientation at different mold positions.

The physical meaning of orientation components is related to the principle axis of the fibers. If the value of a_{xx} is close to unity, then it means fibers are oriented to the flow direction (x-direction). The value of 1 indicates the perfect alignment and 0 indicates the fibers are oriented perpendicular to the flow direction [57]. In the injection molding of fiber reinforced plastics, the large value of a_{xx} near the wall reflects the fact that fibers are aligned to the flow direction and because of less shear stress at mid plane fiber orientation is not affected by the flow [51,58–60].

1.7.2 Reduced strain closure (RSC) model

Experiments by Sepehr et al. [61] showed that Folgar-tucker model overestimated the fiber orientation. Later, Wang et al. [62] modified the Folgar-Tucker model to slow down the orientation and achieve better agreement between experiments and model predictions.

The reduced-strain closure model (RSC) reduces the effect of straining by introducing a scalar factor, κ. The equation is

$$\frac{\mathrm{DA}}{\mathrm{Dt}} = (\mathrm{W}.\mathrm{A} - \mathrm{A}.\mathrm{W}) + \xi(\mathrm{D}.\mathrm{A} + \mathrm{A}.\mathrm{D} - 2[\mathbb{A} + (1-\kappa)(\mathbb{L} - \mathbb{M}:\mathbb{A})]:\mathrm{D}) + 2\kappa\mathrm{C_I}\,\dot{\gamma}(\mathrm{I} - 3\mathrm{A}) \quad (1\text{-}11)$$

where $\mathbb{L}$ and $\mathbb{M}$ are functions of the eigenvectors and eigenvalues of the orientation tensor. The $\boldsymbol{\kappa}$ parameter may range from 0 to 1 and is chosen to fit the experiments [62].

1.8 Thesis objectives

The overall objective of the research presented in this thesis was to improve the understanding of different aspects of D-SMC process.

The objectives of this research study are:

1. To determine the pressure and velocity field in maturation zone.
2. To simulate the dependency of permeability to bundle properties by using Ansys CFX software.
3. To study the microstructure of D-SMC parts using micro computed tomography and microscopy as well as determine the orientation.
4. To investigate rheology of the paste and compound.
5. To investigate the bundle deformation in the compression molding.
6. To simulate the orientation in compression molding using Moldflow package.
7. To simulate the flow in compression molding by introducing the viscosity for suspension of high volume of planar randomly oriented glass bundles using OpenFOAM package.
8. To simulate the flow and heat transfer in compression molding with viscosity variation through thickness particularly in the interface of charges and upper and lower mold plates.

1.9 Thesis Outline

Chapter 1. *Introduction and literature review*. This chapter represents the background of this thesis, including D-SMC process, formulation, impregnation and permeability, compression molding of SMC, simulation of compression molding, orientation models, rheology of fiber filled compounds and comparison of preferential flow and fountain flow. The objectives of thesis are provided.

Chapter 2. *Maturation zone study.* This chapter explores the formation of charge in maturation zone, investigating the pressure and velocity field and simulation the permeability.

Chapter 3. *Microstructure Characterization in Direct Sheet Molding Compound*. This chapter reports the microstructure studies on the D-SMC parts including analysis of the bundle bending and tow shape, microscopy and micro-computed tomography of samples at different location of

parts, mold filling simulation with prediction of orientation by Moldflow package. This chapter has been published in *Polymer Composites*.

Chapter 4. *Simulation of Compression Molding of Direct-Sheet Molding Compound.* This chapter presents the simulation of flow by introducing the viscosity model for suspensions of high volume of planar randomly oriented glass bundles, simulation of bundle movement and experimentally track the bundle in compression molding.

Chapter 5. *Simulation of flow through thickness in D-SMC.* This chapter reports the simulation of flow and heat transfer in compression molding. The behavior of resin rich layer close to the mold plates and different viscosities of charges are also considered and the main focus is on the interface of charges and layers close to upper and lower mold plates.

Chapter 6. *Concluding remarks.* This chapter provides summary contributions and concluding remarks for this thesis as well as recommendations for future work.

Chapter 7. *Appendix.* This chapter contains supplementary information for second component of orientation tensor mentioned in chapter 3.

1.10 References

[1] Han CD. Rheology and processing of polymeric materials. 2007.

[2] Malnati P. Formulation flexibility: Direct-SMC. Http://www.compositesworld.com/articles/formulation-Flexibility-Direct-Smc 2012.

[3] Davis AD, Gramann PJ, Rios AC. compression molding. 2003.

[4] Han CDAE, Lem K. Rheology of Unsaturated Polyester Resins . 11 . Thickening Behavior of Unsaturated Polyester and Vinyl Ester Resins 1983;28:763–78.

[5] Kaviany M. Principles of Heat Transfer in Porous Media - M. Kaviany - Google Books. New York: Springer-Verlag; 2012.

[6] Chen Z-R, Lin Ye, Meng Lu. Permeability Predictions for Woven Fabric Preforms. Journal of Composite Materials 2010;44:1569–86.

[7] Papathanasiou TD. A structure-oriented micromechanical model for viscous flow through square arrays of fibre clusters. Composites Science and Technology 1996;56:1055–69.

[8] Swery EE, Meier R, Lomov S V, Drechsler K, Kelly P. Predicting permeability based on flow simulations and textile modelling techniques: Comparison with experimental values and verification of FlowTex solver using Ansys CFX. Journal of Composite Materials 2016;50:601–15.

[9] Gennaro R, Greco A, Maffezzoli A. Numerical simulation of the microscale impregnation in commingled thermoplastic composite yarns. Advances in Polymer Technology 2010;29:122–30.

[10] Papathanasiou TD. On the effective permeability of square arrays of permeable fiber tows. International Journal of Multiphase Flow 1997;23:81–92.

[11] Belov EB, Lomov SV, Verpoest I, Peters T, Roose D, Parnas RS, et al. Modelling of permeability of textile reinforcements: lattice Boltzmann method. Composites Science and Technology 2004;64:1069–80.

[12] Merhi D, Michaud V, Kämpfer L, Vuilliomenet P, Månson J-AE. Transverse permeability of chopped fibre bundle beds. Composites Part A: Applied Science and Manufacturing 2007;38:739–46.

[13] Shih C-H, Lee LJ. Effect of fiber architecture on permeability in liquid composite molding. Polymer Composites 1998;19:626–39.

[14] Gebart BR. Permeability of Unidirectional Reinforcements for RTM Rproduction. Journal of Composite Materials 1992;26:1100–33.

[15] Phelan FR, Wise G. Analysis of transverse flow in aligned fibrous porous media. Composites Part A: Applied Science and Manufacturing 1996;27:25–34.

[16] Wong CC, Long AC, Sherburn M, Robitaille F, Harrison P, Rudd CD. Comparisons of novel and efficient approaches for permeability prediction based on the fabric architecture. Composites Part A: Applied Science and Manufacturing 2006;37:847–57.

[17] Tadmore Z, Gogos CG. Principles of polymer processing. 2006.

[18] Macoskow CW. Rheology Principles, measurments and applications. 1994.

[19] Engmann J, Servais C, Burbidge AS. Squeeze flow theory and applications to rheometry:

A review. Journal of Non-Newtonian Fluid Mechanics 2005;132:1–27.

[20] Servais C, Luciani A, Månson J-AE. Squeeze flow of concentrated long fibre suspensions: experiments and model. Journal of Non-Newtonian Fluid Mechanics 2002;104:165–84.

[21] Dumont P, Orgéas L, Favier D, Pizette P, Venet C. Compression moulding of SMC: In situ experiments, modelling and simulation. Composites Part A: Applied Science and Manufacturing 2007;38:353–68.

[22] Lee C-C, Folgar F, Tucker CL. Simulation of Compression Molding for Fiber-Reinforced Thermosetting Polymers. Journal of Engineering for Industry 1984;106:114.

[23] Osswald TA. General results on the flow of chopped fiber compounds in compression molding 1987.

[24] Advani SG, Tucker CL. A numerical simulation of short fiber orientation in compression molding. Polymer Composites 1990;11:164–73.

[25] Tucker CL, Folgar F. A model of compression mold filling. Polymer Engineering and Science 1983;23:69–73.

[26] Park CH, Lee WI, Yoo YE, Kim EG. A study on fiber orientation in the compression molding of fiber reinforced polymer composite material. Journal of Materials Processing Technology 2001;111:233–9.

[27] Barone MR, Caulk DA. Kinematics of flow in sheet molding compounds. Polymer Composites 1985;6:105–9.

[28] Odenberger PT, Andersson HM, Lundström TS. Experimental flow-front visualisation in compression moulding of SMC. Composites Part A: Applied Science and Manufacturing 2004;35:1125–34.

[29] Barone MR, Caulk DA. A Model for the Flow of a Chopped Fiber Reinforced Polymer Compound in Compression Molding. Journal of Applied Mechanics 1986;53:361.

[30] Lee C-C, Tucker CL. Flow and heat transfer in compression mold filling. Journal of Non-Newtonian Fluid Mechanics 1987;24:245–64.

[31] Mavridis H, Bruce GD, Vancso GJ, Weatherly GC, Vlachopoulos J. Deformation patterns

in the compression of polypropylene disks: Experiments and simulation. Journal of Rheology 1992;36:27.

[32] Dweib MA, Brdaigh CM. Compression molding of glass reinforced thermoplastics: Modeling and experiments. Polymer Composites 2000;21:832–45.

[33] Thattaiparthasarthy KB, Pillay S, Vaidya UK. Rheological characterization of long fiber thermoplastics – Effect of temperature, fiber length and weight fraction. Composites Part A: Applied Science and Manufacturing 2009;40:1515–23.

[34] Thomasset J, Carreau PJ, Sanschagrin B, Ausias G. Rheological properties of long glass fiber filled polypropylene. Journal of Non-Newtonian Fluid Mechanics 2005;125:25–34.

[35] Ausias G, Agassant JF, Vincent M, Lafleur PG, Lavoie PA. Rheology of short glass fiber reinforced polypropylene. Journal of Rheology 1992;36:525.

[36] Guo R, Azaiez J, Bellehumeur C. Rheology of fiber filled polymer melts: Role of fiber-fiber interactions and polymer-fiber coupling. Polymer Engineering & Science 2005;45:385–99.

[37] Ramazani a., Ait-Kadi a., Grmela M. Rheological modelling of short fiber thermoplastic composites. Journal of Non-Newtonian Fluid Mechanics 1997;73:241–60.

[38] Lee LJ, Marker LF, Griffith RM. The rheology and mold flow of polyester sheet molding compound. Polymer Composites 1981;2:209–18.

[39] Lecorre S, Orgeas L, Favier D, Tourabi A, Maazouz A, Venet C. Shear and compression behaviour of sheet moulding compounds. Composites Science and Technology 2002;62:571–7.

[40] Kenny JM, Opalicki M. Processing of short fibre/thermosetting matrix composites. Composites Part A: Applied Science and Manufacturing 1996;27:229–40.

[41] Corre S Le, Favier D, Dumont P, Orge L. Anisotropic viscous behavior of sheet molding compounds (SMC) during compression molding 2003;19:625–46.

[42] Abrams LM, Castro JM. Predicting molding forces during sheet molding compound (SMC) compression molding. I: Model development. Polymer Composites 2003;24:291–303.

[43] Servais C, Luciani A, Månson J-AE. Fiber–fiber interaction in concentrated suspensions: Dispersed fiber bundles. Journal of Rheology 1999;43:1005.

[44] Jeffery GB. The Motion of Ellipsoidal Particles Immersed in a Viscous Fluid. Proceedings of the Royal Society A: Mathematical, Physical and Engineering Sciences 1922;102:161–79.

[45] Folgar F, Tucker CL. Orientation Behavior of Fibers in Concentrated Suspensions. Journal of Reinforced Plastics and Composites 1984;3:98–119.

[46] Advani SG. Closure approximations for three-dimensional structure tensors. Journal of Rheology 1990;34:367.

[47] Kagarise C, Miyazono K, Mahboob M, Koelling KW, Bechtel SE. A constitutive model for characterization of shear and extensional rheology and flow induced orientation of carbon nanofiber/polystyrene melt composites. Journal of Rheology 2011;55:781.

[48] Advani SG, Tucker CL. The Use of Tensors to Describe and Predict Fiber Orientation in Short Fiber Composites. Journal of Rheology 1987;31:751–84.

[49] Kagarise C, Xu J, Wang Y, Mahboob M, Koelling KW, Bechtel SE. Transient shear rheology of carbon nanofiber/polystyrene melt composites. Journal of Non-Newtonian Fluid Mechanics 2010;165:98–109.

[50] Wang Y, Xu J, Bechtel SE, Koelling KW. Melt shear rheology of carbon nanofiber/polystyrene composites. Rheologica Acta 2006;45:919–41.

[51] Oumer AN, Ali AMS, Mamat OB. Numerical Simulation of Fibre Orientation in Simple Injection Molding Processes n.d.

[52] Bay RS. Fiber orientation in injection-molded composites : A comparison of theory and experiment. PhD thesis, University of Illinois at Urbana-Chamaign, 1991.

[53] Phan-thien N, Fan X, Tanner RI, Zheng R. Folgar – Tucker constant for a fibre suspension in a Newtonian fluid 2006;103:251–60.

[54] Vincent M, Giroud T, Clarke A, Eberhardt C. Description and modeling of fiber orientation in injection molding of fiber reinforced thermoplastics. Polymer 2005;46:6719–25.

[55] Jackson WC, Advani SG, Tucker CL. Predicting the Orientation of Short Fibers in Thin Compression Moldings. Journal of Composite Materials 1986;20:539–57.

[56] Bay RS, Tucker CL. Fiber orientation in simple injection moldings. Part I: Theory and numerical methods. Polymer Composites 1992;13:317–31.

[57] Miled H, Silva L, Agassant J, Coupez T. Numerical Simulation of Fiber Orientation and Resulting Thermo-Elastic Behavior in Reinforced Thermo-Plastics. Mechanical Response of … 2008;10:293–313.

[58] Oumer AN, Mamat O. A study of fiber orientation in short fiber-reinforced composites with simultaneous mold filling and phase change effects. Composites Part B: Engineering 2012;43:1087–94.

[59] Vincent M, Devilers E, Agassant J-F. Fibre orientation calculation in injection moulding of reinforced thermoplastics. Journal of Non-Newtonian Fluid Mechanics 1997;73:317–26.

[60] Miled H, Silva L, Coupez T, Agassant JF. Injection Molding of Fibre Reinforced Thermoplastics: Integration of Fibre Orientation and Mechanical Properties Computations. International Polymer Processing 2012;27:547–56.

[61] Sepehr M, Ausias G, Carreau PJ. Rheological properties of short fiber filled polypropylene in transient shear flow. Journal of Non-Newtonian Fluid Mechanics 2004;123:19–32.

[62] Wang J, O'Gara JF, Tucker CL. An objective model for slow orientation kinetics in concentrated fiber suspensions: Theory and rheological evidence. Journal of Rheology 2008;52:1179.

2 Maturation zone study

2.1 Objective

The maturation process includes a continuous forming operation with pairs of rolls that form a mass of paste material and distributed fiber bundles into a charge. The paste in the doctor boxes is spread over the foil, with an adjustable thickness, and the glass bundles are distributed on top of and over the width of paste. Then, a top layer of paste foil covers the glass bundles (Figure 2-1). As shown in Figure 2-1a, the rolls squeeze the foils together with paste and glass bundles at room temperature. At this stage, the air caught in the spreading process is evacuated via the edge area of the foil. The sandwich of paste and bundles passes through the rollers to smoothly deaerate and impregnate the bundles. The foil is transported to impregnation zone to ensure the impregnation of the fiber bundles with paste at room temperature (Figure 2-1b). The rolls move the charge to the heating zone with controlled temperature. The temperature is set depends on the formulation of the paste. The charge is heated by the heating plates in the first and second level. As shown in Figure 2-2, the charge moves in this section while spending enough time for the paste to thicken and gain enough strength and resistance for handling and compression. At last stage of this section, the charge is cooled down to the ambient temperature. The full line of maturation zone provides the optimum impregnation, good binding of the resin onto the bundles and elevated viscosity of the paste in short period. All these parameters are required for the compression molding of application with improved mechanical properties.

When a sandwich of paste and bundles are squeezed in the first section (Figure 2-1a), the flow is laminar into and in between the fiber bundles. By simplifying assumptions, it is possible to make a mathematical analysis of the operation. Having the physical properties of materials, the dimensions of rolls, the speed and gap distance, the velocity field and pressure is calculated in this section.

In the next part, permeability for flow transverse to a unidirectional bundle is investigated. The permeability of single bundle based on the bundle and flow properties is calculated.

When the charge passes through the maturation zone between rolls (Figure 2-1b), the flow is modeled to learn more about this section of the process.

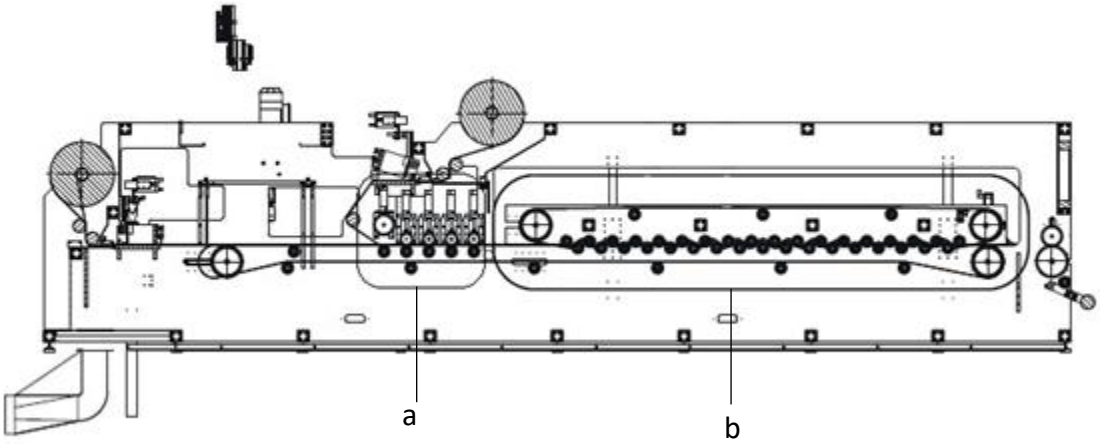

Figure 2-1 Maturation zone a) deaeration unit b) impregnation unit

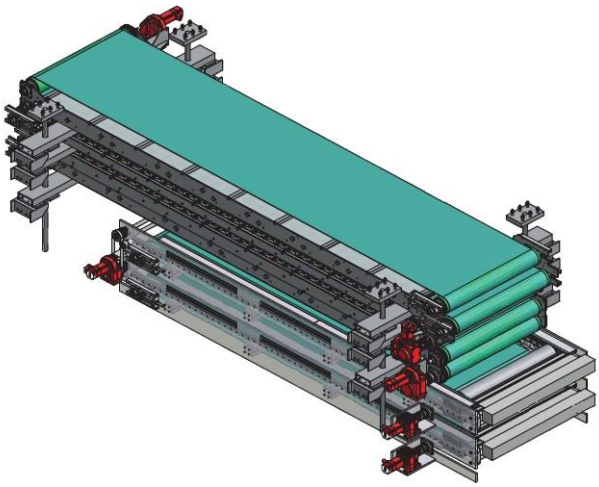

Figure 2-2 Heating and cooling unit

2.2 Flow study of material between rolls

2.2.1 Simplified flow theory

When the paste and bundles pass through the rollers, they experience pressure and flow (Figure 2-1a). The problem is similar to calendaring and used for this analysis. The aim of this section is to calculate the pressure and velocity field.

A rectangular coordinate system as shown in Figure 2-3 is used. The problem is to determine the v_x and v_y components of velocity vector and the pressure P as a function of the position variables x and y.

The equation of continuity reduces to;

$$\frac{\partial v_x}{\partial x} + \frac{\partial v_y}{\partial x} = 0 \tag{2-1}$$

And the x-component of the momentum equation becomes

$$\rho\left[v_x\left(\frac{\partial v_x}{\partial x}\right) + v_y\left(\frac{\partial v_x}{\partial y}\right)\right] = -\left(\frac{\partial P}{\partial x}\right) + \mu\left[\frac{\partial^2 v_x}{\partial x^2} + \frac{\partial^2 v_x}{\partial y^2}\right] \tag{2-2}$$

Where ρ and μ are the density and viscosity of the material.

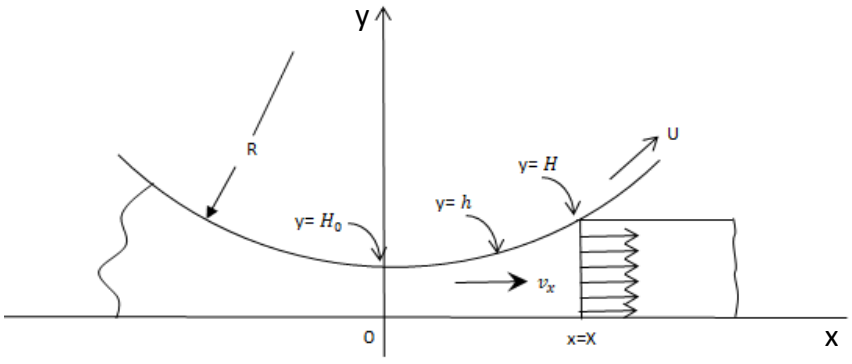

Figure 2-3 Notation for analysis of flow

The rolls have equal size and rotate at the same speed. The radius of the rolls is R_r, their surface speed is U, and their separation at nip is $2H_0$. The region where y-position is positive is considered because of symmetry about the x-axis. Certain simplifying assumptions are made to reduce the equation (2-2) to a manageable form. The left side of equation (2-2) represents the acceleration term. Because the flow is relatively slow and viscous forces are large, it can be ignored. Moreover, it is assumed that the variation of v_x is much less in x-direction than in y-direction. Therefore, the derivatives of v_x with respect to x can be ignored [1] . With these assumption equation (2-2) reduces to

$$\left(\frac{\partial P}{\partial x}\right) = \mu\left(\frac{\partial^2 v_x}{\partial y^2}\right). \tag{2-3}$$

Upon integration and applying the boundary condition the following expression for volumetric flow rate is obtained.

$$Q = 2h\left[U - \frac{h^2}{3\mu}\left(\frac{\partial P}{\partial x}\right)\right] \tag{2-4}$$

A dimensionless independent variable ρ, defined by the equation

$$\iota = \frac{x}{\sqrt{2RH_0}} \tag{2-5}$$

inserted into equation (2-4) which is then rearranged. By using h as a function of x-direction the expression for pressure gradient then obtained.

$$\frac{\partial P}{\partial x} = \frac{\mu U}{H_0}\sqrt{\frac{18R}{H_0}}\left[\frac{\iota^2 - \varsigma^2}{(1+\iota^2)^3}\right] \tag{2-6}$$

The parameter ς is defined by the equation

$$\varsigma^2 = \frac{Q}{2UH_0} - 1 \tag{2-7}$$

Upon integration, the expression for pressure is obtained

$$P = \frac{\mu U}{H_0}\sqrt{\frac{9R_r}{32H_0}}\,[g(\iota,\varsigma) + C] \tag{2-8}$$

Where the function $g(\iota,\varsigma)$ and C are defined by the equations

$$g(\iota,\varsigma) = \left[\frac{\iota^2 - 1 - 5\varsigma^2 - 3\varsigma^2\iota^2}{(1+\iota^2)^2}\right]\iota + (1 - 3\varsigma^2)tan^{-1}\iota \tag{2-9}$$

$$C = 5\varsigma^3. \tag{2-10}$$

The velocity component v_x is obtained by combining equation (2-3) and (2-6),

$$\frac{v_x}{U} = \frac{2+3\varsigma^2(1-\Upsilon^2)-\iota^2(1-3\Upsilon^2)}{2(1+\iota^2)} \tag{2-11}$$

Where

$$\Upsilon = \frac{y}{h}. \tag{2-12}$$

2.2.2 Velocity and pressure profile

The parameters used to calculate the pressure and velocity fields are shown in Table 2-1 Parameters used for analysis. Matlab 14.0 was used to calculate and plot the pressure and velocity field. The zero shear viscosity of paste including 20 percent glass bundles is used. The details of measurement is available in section 5.2.2.

Table 2-1 Parameters used for analysis

Roller radius (R_r)	45mm
Nip (H_0)	1.25 mm
Charge thickness (H)	1.5 mm
Velocity (U)	0.02 m/s
Zero shear viscosity	6832 Pa.s

Figure 2-4 shows the pressure profile over the x-direction which was plotted in Matlab 2014a. The pressure profile shows the maximum before the nip. The viscosity affects the pressure profile [2]. As the pressure is a direct function of viscosity, we chose the constant maximum viscosity to get

the maximum pressure that material experiences through rolls. velocity at regions b and c are flat, therefore there is no shear thinning behavior. at regions a and c there is a variation of velocity and the paste behavior is shear thinning therefore pressure shifts to lower values.

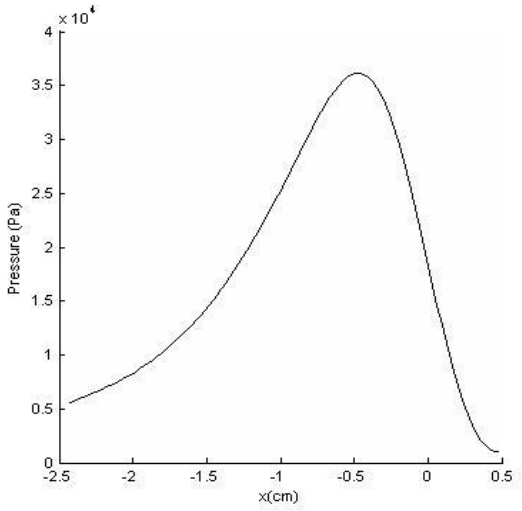

Figure 2-4 Pressure profile over the x-direction

Figure 2-5 shows the velocity vectors in the region of analysis (Figure 2-3). Region d is where the material lost its contact with the rolls and the velocity profile is flat and magnitude of velocity is equal to rolls surface speed. In region b, the compound experiences the maximum pressure and velocity profile are flat and equal to the roll surface speed. Between regions of b and d flow is the forward direction.

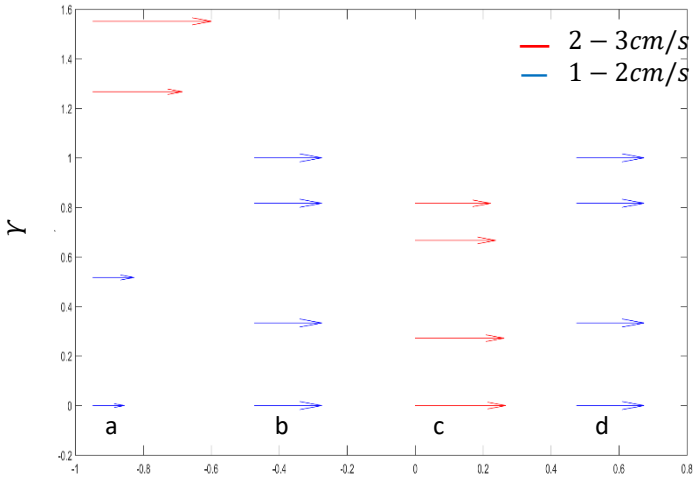

Figure 2-5 Velocity vectors in the analysis region

2.3 Permeability

2.3.1 Image analysis

In order to capture the architecture of the bundles in the charge, images are obtained by Zeiss Axio Imager Z1 upright microscope. Samples are cut from the charge and mounted in the epoxy resin. Surfaces of the cross section of charge are rough because of thickened paste. The samples are not hard enough to be polished and obtain a smooth surface. Therefore, the z-stack option available in the microscope is used. This option allows imaging through a thick section of rough thickness. The images are further processed using deconvolution to improve the resolution and create a single image containing the most "in focus" data from z-stack. Also, using z-stack and stitching options of microscope enable coverage over the large area of interest.

The bundles used in this study are JM EC 2400 272 and provided by Johns Manville. The bundles are slender with elliptical cross section. The imageJ package is used to calculate the average properties of bundles, which are summarized in Table 2-1. Images of the fiber bundle cross section (Figure 2-8) are used to determine the fiber volume fraction in bundle, v_f, as follows:

$$v_f = \frac{N_f \, A_{fiber}}{A_{bundle}} \tag{2-13}$$

Where N_f, A_{fiber} and A_{bundle} are number of fibers in the bundle, fiber cross sectional area and bundle cross sectional area, respectively. The areas of fibers and bundles were measured as shown in Figure 2-7. Figure 2-8 also shows that the fibers in the bundle have a hexagonal arrangement (closest packing).

Table 2-2 Bundle properties

Average minor axis (mm)	0.08±0.02
Average major axis (mm)	0.87±0.12
Fiber diameter (mm)	0.013±0.002
Fiber volume fraction in bundle	0.46±0.07

2.3.2 Mathematical model of flow into the bundle

Darcy`s law models flow in porous media;

$$\langle u \rangle = -\frac{K}{\eta}. \langle \nabla P \rangle \quad (2\text{-}14)$$

Equation 2-14 relates flow rate to the driving pressure gradient in terms of permeability of fibrous preform and viscosity of the resin [3].

The Stokes equation has been used to analyse the flow of fibrous bundles. The equation is:

$$\nabla P = \eta \nabla^2 u \quad (2\text{-}15)$$

Permeability is numerically estimated by solving the flow in simulation domain with Stokes equation and then back substituting resulting velocity and pressure drop into Darcy`s law. Steady, incompressible and laminar flow in fibrous media are considered [4–7]. The paste from top and bottom layers pass through the bundles. In the middle layer of bundles, there is the possibility of having flow into the bundles from both directions. In this simulation, as the majority of bundles are located above and below the middle layer, it is assumed that the flow is in the direction from the top of the bundle and exiting from the bottom (Figure 2-6).

Figure 2-6 shows the simulation domain which created in three-dimensional by Solidworks 2016 and mesh by Ansys meshing with a total element of 1.5 million. The dimensions for the bundle is similar to measured properties. For all the simulation, root mean square normalized value of residuals for velocity and pressure was under 10^{-5} which according to Ansys manual is an indication of tight convergence [8].

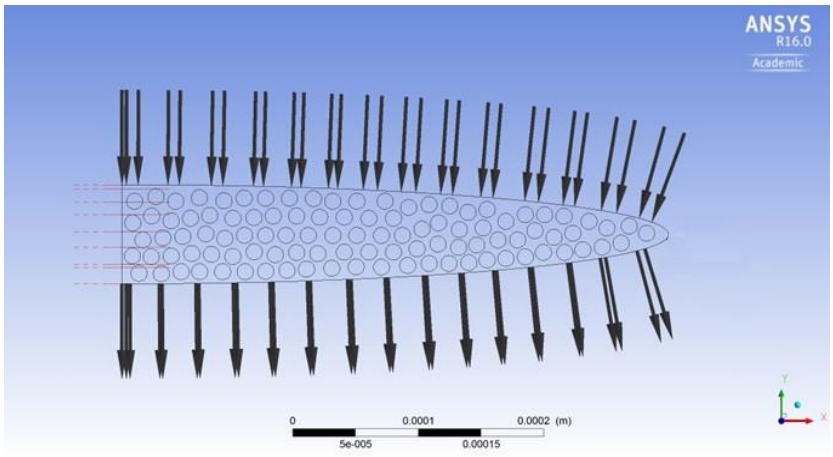

Figure 2-6 Simulation domain for bundle

The boundary condition at solid fiber boundaries includes no slip that was the zero velocity on the surface of fibers [7,9]. At upper boundary of the bundle (inflow) constant pressure and lower

boundary of the bundle (outflow) zero pressure are applied, respectively [7]. The left boundary in Figure 2-8 is assumed to be the axis of symmetry.

The resin used for this simulation is polyester paste, which follows the Carreau rheology model with the zero and infinite shear viscosities of 606 and 16.4 Pa.s and time constant and power law index of 21s and 0.36, respectively. The details of the rheology measurements are given in the 5.2.2.

2.3.3 Result of permeability studies

Figure 2-7 shows the images of the single bundle before distribution on the paste. The fibers are packed and in touch in the bundles. Figure 2-8 shows a cross section of different bundles in the charge after exiting the maturation zone. When the bundles are distributed across the paste and pass through the rolls, the paste is forced into and between the fiber bundles. The fiber bundle shapes change due to the resin flow, pressure, and the close bundled network. Figure 2-8d shows stretched bundles. In Figure 2-8b and c, the fibers within the bundles are spread apart, particularly Figure 2-8c. During impregnation, the progressive force between bundles and paste will not cause a sudden change in fiber movement and increasing viscosity in maturation zone may prevent any rapid bundle deformation.

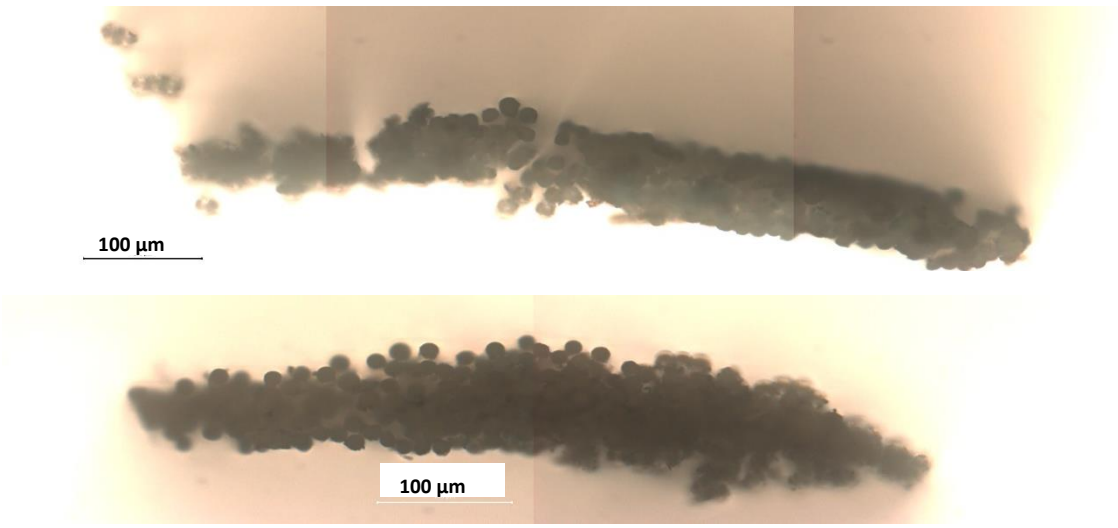

Figure 2-7 Images of single bundle

Centea and Hubert [10,11] proposed the model for the degree of impregnation by quantifying the visible dry tow area. Since no dry fiber tow is observed in images of bundles cross section the degree impregnation of bundles is complete.

The pressure gradient and velocity results from the simulation of Stokes equation (2-15) are shown in Figure 2-9. The pressure gradients are divided by average viscosity to include the effect of viscosity in each simulation result. The slope of the graph shows the permeability of bundle. After linear fitting to Darcy's equation (2-14), the estimate of permeability is obtained (Table 2-3).

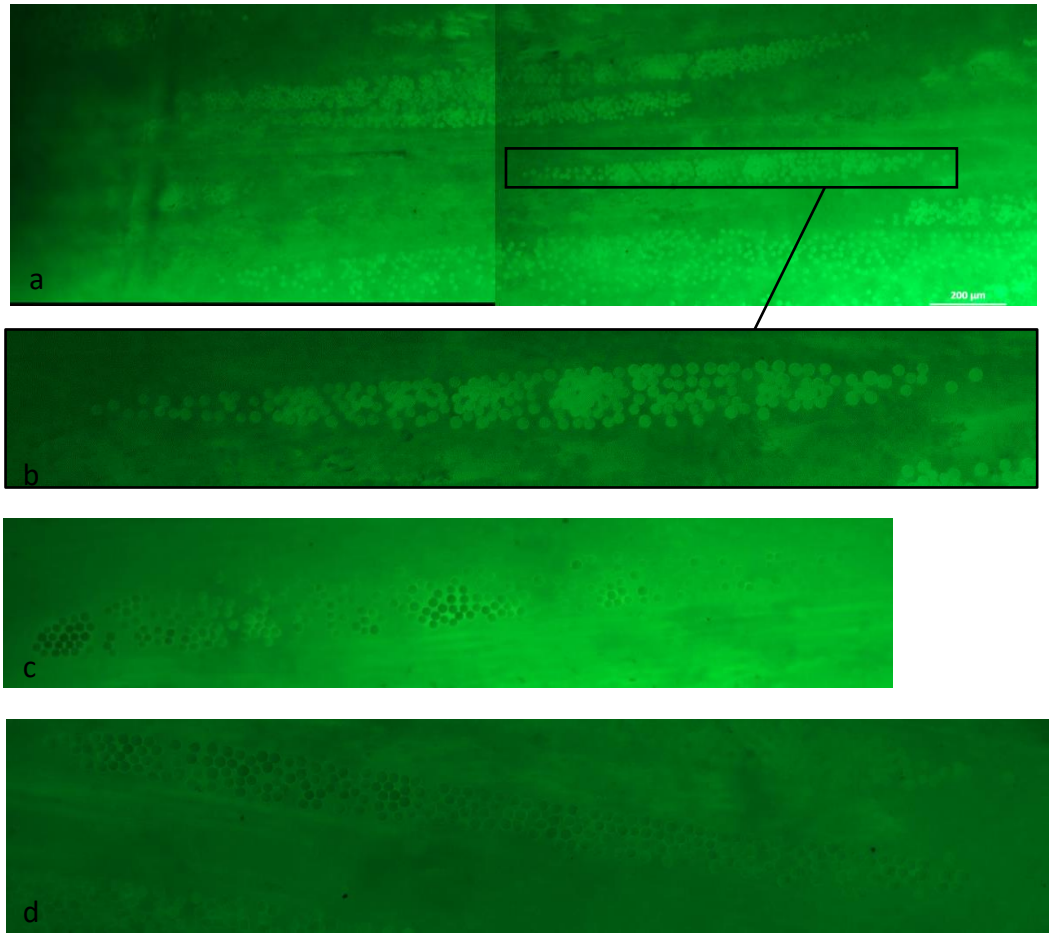

Figure 2-8 Images of cross section of different bundles in the charge

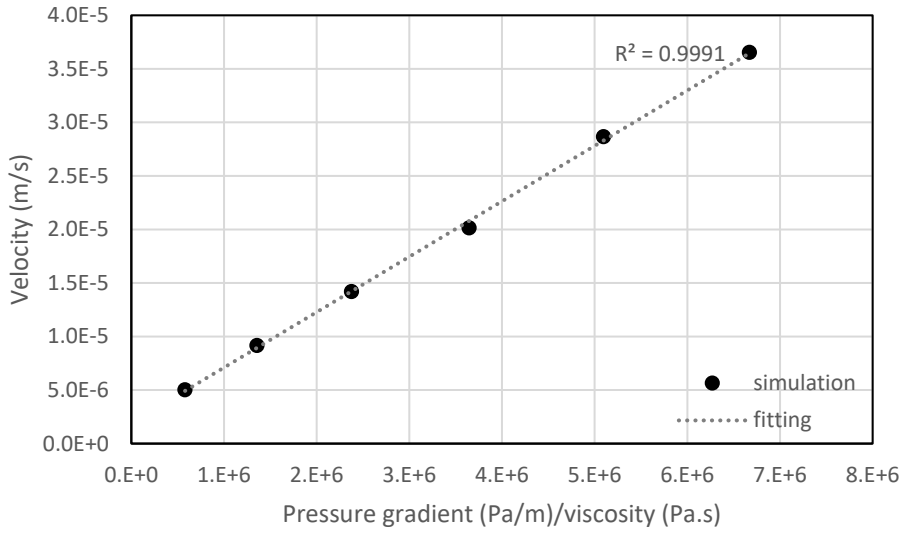

Figure 2-9 Velocity vs. pressure gradient over viscosity

To validate the obtained permeability, the tow permeability relations for flow parallel to hexagonal arrays of solid cylinders proposed by Gebart is used [12,13].

$$K = \frac{16}{9\pi\sqrt{6}}\left(\sqrt{\frac{\pi}{2\sqrt{3}(1-\epsilon)}} - 1\right)^{2.5} r^2 \tag{2-16}$$

$$\epsilon = 1 - N_f \frac{r^2}{ab} \tag{2-17}$$

where a, b and r are the minor and major axis of bundle and radius of fibers and ϵ is tow porosity. The porosity of bundle equation (2-17) was calculated as 0.54 and the value of permeability from simulation and equation (2-16) are shown in Table 2-3.

Table 2-3 Permeability values form simulation and equation

Permeabilty ($m^2 \times 10^{-12}$)	Simulation	Equation (2-16)
K	5.2	1.0

The discrepancy between the permeability obtained from simulation and equation can be related to the configuration of fibers in the bundle also a high ratio of major axis to minor axis of the bundle. Fibers are not totally in a hexagonal arrangement in the bundle to provide the equal path between them for the resin to flow. In the development of equation (2-16), it was assumed spaces

between fibers provide equal paths for the flow while the flow paths are not equal for the arrangement fibers in the bundle.

2.4 Flow study in the maturation zone

2.4.1 Simulation

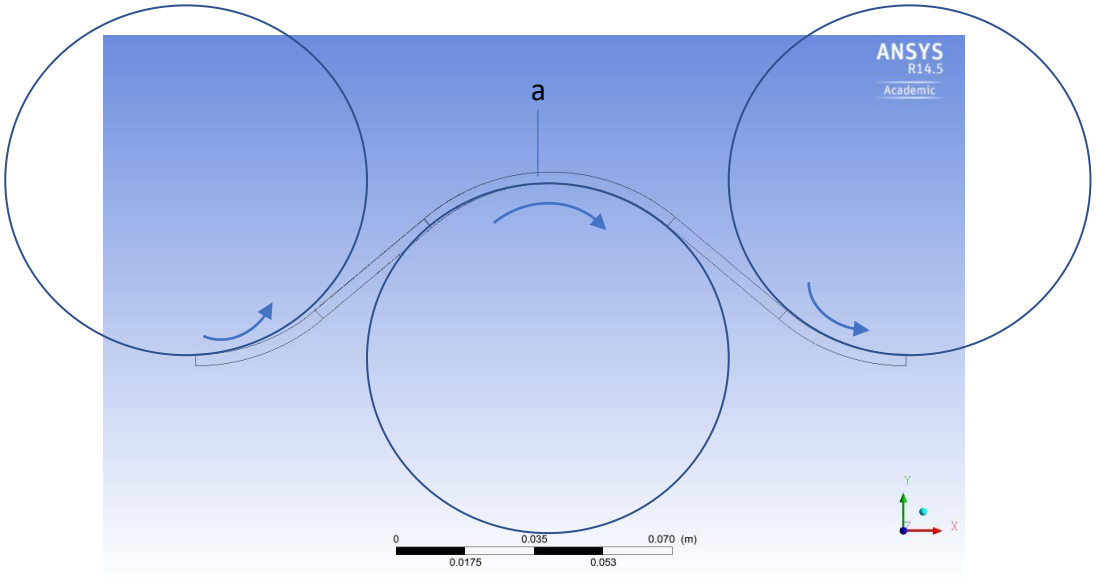

Figure 2-10 Geometry of rollers and compound a) compound flow region

The passing of the compound between rolls in maturation zone (Figure 2-1b) is examined in a commercial package of Ansys CFX 16.0. Geometry and mesh as shown in Figure 2-10 are created in ICEM CFD 16.0. The rolls radius and line speed are available in Table 2-1. Using line speed (2cm/s), rolls co-rotate at 0.44 rad/s. The fluid region consists of five sections in which the linear and rotational velocities are equalized to meet the rolls rotation speed. The viscosity of compound follows the Carreau model with the same values of section 2.2.1. To analyze the flow during maturation zone, steady-state laminar flow of compound is considered on flow domain. Flow through the rolls is simulated by Navier Stokes equation (2-15).

2.4.2 Result of maturation zone simulation

As a compound passes through the rolls, it experiences the constant velocity and shear as shown in Figure 2-11a, b. The rolls co-rotate at the same speed and cannot impose velocity and shear variation through the thickness of compound. Seventeen bottoms rolls operate in the conjunction with the top rolls (Figure 2-1b) to permit impregnation of the bundles. The compound on the foil

is transported through the impregnation section by the under belt together with a top link belt. The belt consists of interlocking chains in which each chain can move a short distance. The belt passes through rolls and opening and closing chains knead the paste and locally cause fiber bundle impregnation and movement. The efficiency of the interlocking chains in impregnating the bundles should be further simulated and experimentally examined. The foil is transported through the smoothing rolls, which is at the end of maturation zone. The smoothing rolls eliminate indentations and undulation by interlocking chains on the surface of the compound.

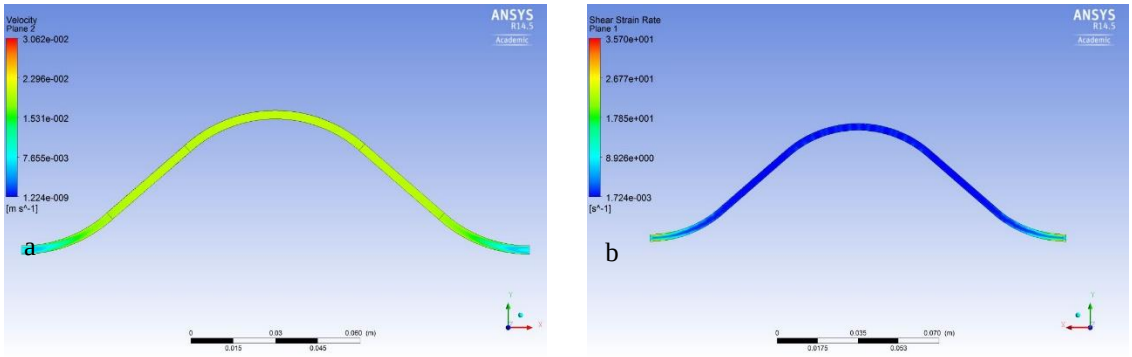

Figure 2-11 Velocity and strain rate in the flow domain

2.5 Conclusion

The numerical analysis of flow in Figure 2-1a shows the maximum pressure occurs before nip. The velocity profile is also presented for flow domain. Images of a cross section of charge show different shapes of bundle cross sections and confirm the impregnation of fibers at the end of maturation zone. The permeability of bundle is also calculated by simulation and compared to the available model. The disagreement is related to the high major to minor axis and also the arrangement of fibers in the bundle. Simulation of flow in Figure 2-1b shows that the impregnation is mainly because of the interlocking chain of transforming belt. The opening and closing the chains leads to local knead of the paste and impregnation of bundles with paste.

2.6 References

[1] James M. McKelvey. Polymer processing. n.d.

[2] Kiparissides C, Vlachopoulos J. Finite element analysis of calendering. Polymer Engineering and Science 1976;16:712–9.

[3] Suresh G. Advani. Flow and Rheology in Polymer Composites Manufacturing. n.d.

[4] Chen Z-R, Lin Ye, Meng Lu. Permeability Predictions for Woven Fabric Preforms. Journal of Composite Materials 2010;44:1569–86.

[5] Papathanasiou TD. A structure-oriented micromechanical model for viscous flow through square arrays of fibre clusters. Composites Science and Technology 1996;56:1055–69.

[6] Swery EE, Meier R, Lomov S V, Drechsler K, Kelly P. Predicting permeability based on flow simulations and textile modelling techniques: Comparison with experimental values and verification of FlowTex solver using Ansys CFX. Journal of Composite Materials 2016;50:601–15.

[7] Gennaro R, Greco A, Maffezzoli A. Numerical simulation of the microscale impregnation in commingled thermoplastic composite yarns. Advances in Polymer Technology 2010;29:122–30.

[8] Simulation Driven Product Development | ANSYS n.d.

[9] Wong CC, Long AC, Sherburn M, Robitaille F, Harrison P, Rudd CD. Comparisons of novel and efficient approaches for permeability prediction based on the fabric architecture. Composites Part A: Applied Science and Manufacturing 2006;37:847–57.

[10] Centea T, Hubert P. Measuring the impregnation of an out-of-autoclave prepreg by micro-CT. Composites Science and Technology 2011;71:593–9.

[11] Centea T, Hubert P. Modelling the effect of material properties and process parameters on tow impregnation in out-of-autoclave prepregs. Composites Part A: Applied Science and Manufacturing 2012;43:1505–13.

[12] Gebart BR. Permeability of Unidirectional Reinforcements for RTM Rproduction. Journal of Composite Materials 1992;26:1100–33.

[13] Phelan FR, Wise G. Analysis of transverse flow in aligned fibrous porous media. Composites Part A: Applied Science and Manufacturing 1996;27:25–34.

3 Microstructure Characterization in Direct Sheet Molding Compound

This chapter has been published as,

A. Motaghi and A. N. Hrymak, "Microstructure characterization in direct sheet molding compound," *Polymer Composites*, Jul. 2017 (DOI: 10.1002/pc.24495)

and presented at,

Polymer Processing Society Conference (PPS30), Ohio, USA, 2014

Automotive Composite Conference and Exhibition (ACCE), Detroit, USA, 2016

3.1 Abstract

The microstructure of fiber glass bundles used in the direct sheet molding compound (D-SMC) was investigated in a flat plaque mold. Analyses of the bundle deformation, including bending and deformation of the tow shape, were done for the charge and specific sites within a square plaque part for 30 percent and 62 percent of initial charge mold area coverages. Microscopy and micro-computed tomography (micro-CT) of the samples clarify the microstructure of the bundles after flow. Samples were taken at different flow locations within the plaque corresponding to increasing flow length from the center. The bundles at the part edge and corner deform more than the bundles close to center of the mold in both initial charge cases. The bundles flattened at all positions and bundle bending was mainly observed at the corner. The tow width changes and tow deflections were higher in the samples of 30 percent mold area coverage. The micro-CT images showed that the bundles keep their cohesion and stay straight within the middle of the flow path position, but bend at the edge of the mold. Mold filling simulation using Moldflow™ (Autodesk) predicted fiber tow orientation through the thickness using the reduced-strain closure (RSC) models for fiber distribution for 30 and 62 percent initial mold area coverage. The measured value of orientation from micro-CT images confirms the random orientation through the thickness, consistent with the RSC model.

3.2 Introduction

Compression molding of sheet molding compounds (SMC) is one of the techniques in manufacturing fiber reinforced composite materials. Charges of SMC consist of glass fiber (15-30 weight percent) reinforced paste. The paste is mainly polyester resin filled with calcium carbonate and other additives. The process includes compression molding of the charge(s) in a hot mold at a specified closing speed. The mold is typically kept closed for 60-120s for curing of material, and then the molded part is ejected [1-3]. Unsaturated polyester (UP) is one of the most commonly used thermoset resins for compression molding. This material has a good strength property while maintaining high resilience that is needed in many demanding applications [4, 5] .

The combination of thermoset resin and a high volume of long glass bundles as reinforcement provides the product with strength, stiffness and dimensional stability. Fiber orientation is of great importance because it has implications on the functional and mechanical performance of the final product. The impregnation and entanglement of long bundles in the composite lead to enhanced physical and mechanical properties [6-8]. The fibrous structure of each bundle contains a few hundreds of fibers, which are exposed to deformation, orientation, consolidation, deflection, breakage and shearing during the process. Several characterization techniques and observation methods were used to study these phenomena. Micro-CT is widely used to visualize the resulting fiber network in a three dimensional image of samples from the final product [3, 9, 10]. The flow history, material rheology, and fiber-fiber contact induce changes in the bundle structure, displacement and evolution of fiber-fiber contact during the compression [11]. Le et al. highlighted the porosity, migration of polymer-matrix, core skin-core regions, orientation, flattening and widening of bundles in compression molding using micro-CT [3]. Dumont et al. used transparent PMMA as a matrix to study the effect of resulting fiber deformation and orientation on the stress level [2]. Centea et al. studied the impregnation of fiber bundles in out-of-autoclave prepegs using the micro-CT method [12-13]. The comparison of the optical method and micro-CT was discussed in the study by Bernasconi et al. [14].

The Folgar-Tucker model has been used to predict the state of orientation tensor of fibers in injection and compression molding [15-16]. The reduced strain closure (RSC) model was introduced to compensate for observed slower alignment of fibers in the process [17] than that

predicted by the Folgar-Tucker model. Moldflow™ is able to predict orientation in polymer processing applications.

In summary, microscopic techniques with image analysis and micro-CT image analysis clarify the fiber bundle microstructure in the samples at different positions. The orientation, deflection, average bundle width change and length were measured to quantify the fiber microstructure characteristics. Moldflow™ simulation has been used to predict the fiber orientation in compression molding using the RSC model.

3.3 Material and process

Unsaturated polyester (UP) is one of the most commonly used thermoset resins for compression molding (SMC). The UP resin (AOC Inc., T320) has a Brookfield viscosity of 2350 cps at 25 °C and specific gravity of 1.06. Each additive in a formulation serves a specific purpose. For example, the inorganic filler, $CaCO_3$, improves dimensional stability, better heat conductance during curing. In the maturation zone, thickening agent increases the viscosity suitable for compression molding [4]. Table 3-1 provides the formulation used in this work.

A twin screw extruder (Figure 3-1) was used to mix the liquid raw materials and solid ingredients to form a homogeneous compound. Two equal streams of paste, which exit the extruder and transferred material into doctor boxes. The glass bundles were cut and distributed across the width of the resin paste sheet as a layer while the paste was moving on a film through the machine. This movement induced the bundles to orient more in the machine direction (x axis) and not in a random orientation ($a_{xx} = 0.54$). The sandwich of paste and fiber passed through a roller section for degassing and tow impregnation, where fiber tow wet out takes place. The impregnated paste and glass fiber tows then moved through a maturation zone within a temperature-controlled environment where the chemical thickening of the composite material takes place within a few minutes. At the end of the zone, the viscosity of the composite material increased, and the charge cooled down to ambient temperature. The material charge moved directly onto the cutting table, where it was cut into the required charge pattern and subsequently laid up to form the charge load for the compression molding process. The charges are placed in the open mold of a compression molding press, which was then closed to mold the charge(s). Depending on the sheet width, throughput (0-350kg/hr) and material formulation, the complete cycle, from compounding through

molding, can take 20 minutes. The residence time in the maturation zone depends on the line speed and can take 6-15 minutes. Figure 3-1 shows the entire D-SMC process [18].

Table 3-1 Formulation of D-SMC paste

Raw Material	Grade	Supplier	[wt.-%]
Unsaturated polyester Resin	T320	AOC Inc.	23.05
Low profile additives	LS N640	AOC Inc.	15.37
Peroxide	Trigonox C	AkzoNobel	0.42
Wetting Agent	W 996	BYK	1.54
Internal Mould Release	Ceasit Ca stearate	Baerlocher	1.92
Water			0.08
Filler (CaCO3)	FL5	Omyacarb	57.63
Thickening Powder	Magchem 200AD	Magnesia Specialties	0.46

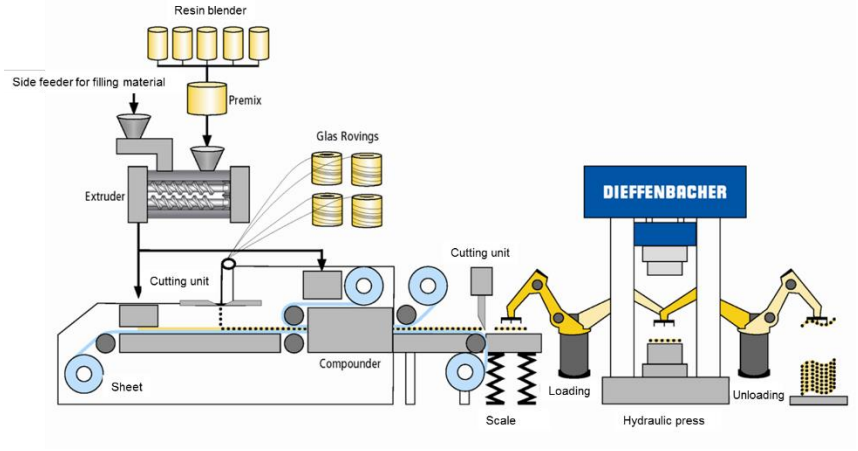

Figure 3-1 Schematic view of D-SMC process

3.4 Characterization of the microstructure

The D-SMC plaque mold dimensions were 457.2 mm by 457.2 mm and thickness of 2.8 mm. Two charges, stacked on each other, each had dimensions of 360 by 360 mm and were initially at the center of the mold and covered 62 percent of the mold area. Four charges each having dimensions of 254 by 254 mm were initially at the center of the mold and covered 30 percent of the mold area. Figure 3-2 shows the positions of the chosen samples in the sheet. The sampling positions of interest were identified as middle (M), diagonal (D), edge (E) and corner (C).

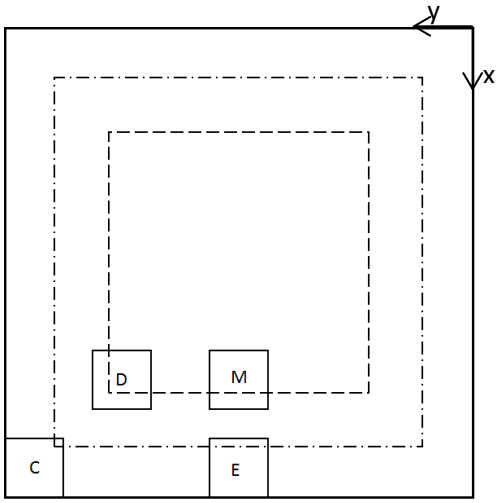

Figure 3-2 Positions of samples in the sheet; D: diagonal, M: middle, E: edge, C: corner, positions of the initial charge (30 percent mold area coverage (– – – –) , 62 percent mold area coverage (– · – · –)

3.4.1 Fiber orientation through the thickness

The sample was mounted in epoxy resin and thickness direction polished on a Struers Roto-Pol 35 polisher with 2-micron diamond powder followed by 1/4-micron diamond powder, both suspended in Pella A Oil. Confocal microscopes, Zeiss LSM 510 DUO Vario and Zeiss SteReo LUMAR V12, provided digital images using laser reflection detector mode and Matlab2014a Image Analysis toolbox was used to interpret the images. The fiber cross section was captured on the image surface as an ellipse, because of the cross-sectional angles due to the fiber orientation, and the major and minor axes were measured to provide the in-plane orientation angle. Figure 3-3 shows the identified fibers in the cross-sectional image plane of which the minor and major axes dimensions were measured. The out-of-plane angle, θ, is given by,

$$\theta = sin^{-1}\left({}^{minor\ axis}/_{major\ axis}\right) \qquad (3\text{-}1)$$

Equation (3-2) calculated the components of the orientation tensor [20, 21].

$$\begin{bmatrix} a_{xx} = \langle sin^2\theta cos^2\varphi \rangle & a_{xy} & a_{xz} \\ a_{xy} & a_{\mathrm{yy}} = \langle sin^2\theta sin^2\varphi \rangle & a_{zx} \\ a_{xz} & a_{yz} & a_{\mathrm{zz}} = \langle cos^2\theta \rangle \end{bmatrix} \qquad (3\text{-}2)$$

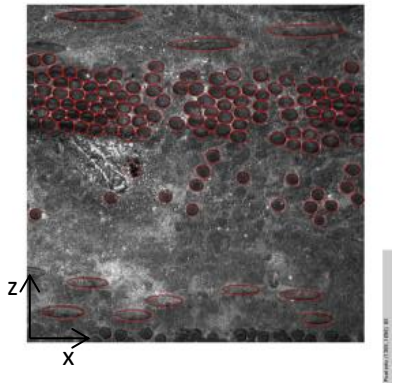

Figure 3-3 Processed image for the measurement of orientation

3.4.2 In-plane orientation

The resin was burnt out of the sample in a furnace at 700°C for 2 hours. Post burn out, two metal meshes held the samples in a sandwich configuration, fixed by clips to prevent the re-orientation of the fiber bundles during the dissolution of additives from the sample. Samples were soaked in vinegar to remove fillers, mainly carbonate calcium, for two days. The samples were dried in an oven at 100° C for 1 hour. The top layers of the sample were removed by tweezers and the Axiolmager Z1 Upright microscope and VHX microscope were used to obtain images of the surface area. Images were stitched to cover the whole area of the 5 by 5 cm sample.

Images of the surface (Figure 3-4) do not have enough contrast to convert to binary image in Matlab. Images were analyzed using Image Pro Premier (Media Cybernetics, Inc., Rockville, MD, USA) and ImageJ [21]. Figure 3-4 b shows the parameters used to measure the in-plane orientation by choosing the two visible ends of bundles to define the 2D orientation vector.

Equation (3-2) was used to calculate the orientation tensor considering the in-plane orientation angle, φ, assuming that the-out-of-plane orientation, θ, is negligible. Analysis was done with 100

bundles in each sample to most accurately describe the in-plane orientation. The 2D orientation vectors are good representations of bundle orientation, if bending is negligible.

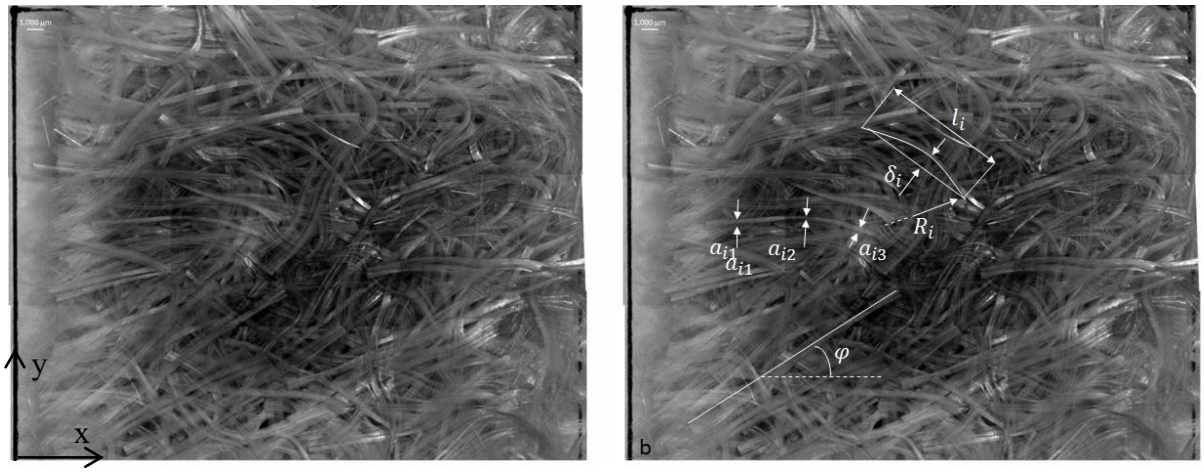

Figure 3-4 a) Stitched image of corner sample b) measured parameters of a_{ij}, l_i, R_i, φ to quantify the fiber bundle.

3.4.3 Deflection, fiber width and length

Figure 3-4b shows the parameters used in calculating deflection. The method includes choosing two points at two visible ends of the bundle with the distance of l_i and measuring curvature radius (R_i) as shown in equation (3-3) [2]. Simple curvature was assumed because very few bundles were observed from the total (less than 10 of 400) that showed complex curvature. Complex curvature was observed mainly in the corner position samples. Relatively few bundles (less than 40 of 400), were observed with bending, and thus the overall observation is that fiber bundle bending was not significant [2].

$$\delta^* = \frac{1}{N}\sum_{i=1}^{N}\frac{|\delta_i|}{l_i} = \frac{1}{N}\sum_{i=1}^{N}\frac{R_i}{l_i}\left(1-\sqrt{1-\left(\frac{l_i}{R_i}\right)^2}\right) \qquad (3\text{-}3)$$

Equation (3-4) defines the dimensionless average width of the bundles for N (~100) bundles. The a_{i0} represents the width of the bundles in the charge. ImageJ measures the distance between two points (a_{ij}) for three different sections along the bundle to measure the bundle width, (Figure 3-4b).

$$a^* = \frac{\sum_{i=1}^{i=N}\sum_{j=1}^{j=3} a_{ij}}{\sum_{i=1}^{i=M} a_{i0}} \qquad (3\text{-}4\ )$$

To measure the bundle length, a tweezer grasped the bundle in such a way as both ends of the bundles were located in the sample area and not affected by the cutting of the samples. ImageJ was used to measure the bundle length at different positions and the averages were calculated.

3.4.4 Micro computed tomography

X-ray micro computed tomography (micro-CT) over a range of spatial resolutions was performed to provide a 3D characterization of the fiber bundles structure. Micro-CT was used to scan samples at M, E, D and C sample positions, after dissolution of the additives to improve resolution of the fiber structure. The micro-CT was performed on a General Electric Lucus RS-9 and Skyscan 1172 high-resolution, and the sample scanned at voxel sizes of 20, 50 and 10 µm with beam energy of 65 and 80kV. The MicroView, Dataview and Skyscan software packages were used to construct and analyze the images.

3.5 Moldflow simulation

The plaque mold filling was simulated using reactive compression molding in Autodesk Simulation Moldflow™ Synergy 2014. The material system of polyester containing 30 percent glass fiber (Menzloit BMC 01) available in Moldflow™ library was used and edited properties to the similar formulation (Table 3-2 and Table 3-3). The reactive viscosity and N-order kinetic models define the viscosity and degree of cure in the filling process. In the viscosity model, equation (3-5) and (3-6), η, $\alpha, \dot{\gamma}, \alpha_g$ and T represent the viscosity, the degree of cure, the shear rate, the degree of cure at gelation and temperature while c_1 , c_2 , n, T_b and τ are the model parameters obtained from curve fitting. In the reactive kinetic model, equations (3-7) and (3-8), R is the universal gas constant, m_α and n_α are the kinetic exponents, E_i and A_i are the activation energy and the frequency factor. The model parameters were chosen from the reference for the similar formulation as shown in Table 3-2 and Table 3-3 and used in Moldflow™ [22].

$$\eta(\alpha, T, \dot{\gamma}) = \frac{\eta_0(T)}{1 + \left(\frac{\eta_0(T)\dot{\gamma}}{\tau}\right)^{1-n_{1\alpha}}} \left(\frac{\alpha_g}{\alpha_g - \alpha}\right)^{(c_1 + c_2\alpha)} \quad (3\text{-}5)$$

$$\eta_0(T) = Bexp(^{T_b}/_{T}) \quad 3\text{-}6)$$

$$\frac{d\alpha}{dt} = (K_1 + K_2\alpha^{m_\alpha})(1-\alpha)^{n_\alpha} \quad (3\text{-}7)$$

$$K_i = A_i \exp\left(-\frac{E_i}{RT}\right), i = 1,2 \tag{3-8}$$

Table 3-2 Parameters for the viscosity model [22]

c_1	1	$n_{1\alpha}$	0.428
c_2	0	τ	3209
α_g	0.1	T_b	6006 K
B	0.004676		

Table 3-3 Parameters for the kinetic model [22]

E_1	149.7 kJ/mol	A_1	1.07×10^{13}
E_2	87.54 kJ/mol	A_2	7.2×10^{10}
m_α	0.711	n_α	1.464
H	415000 J/kg		

The charge of SMC was located at the center of the mold, and the closing speed was 1 mm/s. A 3D mesh with 10 layers through the thickness of 9.1mm for 30 percent initial mold area and 4.52mm for 62 percent mold area coverage was used with the surface mesh size of 3mm for the simulation [23]. The charge was at 50° C and mold surface at 140° C consistent with the experiment.

The reduced-strain closure model (RSC) reduces the effect of straining by introducing a scalar factor, κ. The equation is [17]

$$\frac{\mathrm{DA}}{\mathrm{Dt}} = (\mathrm{W.A} - \mathrm{A.W}) + \lambda(\mathrm{D.A} + \mathrm{A.D} - 2[\mathbb{A} + (1-\kappa)(\mathbb{L} - \mathbb{M}:\mathbb{A})]:\mathrm{D}) + 2\kappa \mathrm{C_I}\,\dot{\gamma}(\mathrm{I} - 3\mathrm{A}) \tag{3-9}$$

where $\mathbb{L}$ and $\mathbb{M}$ are functions of the eigenvectors and eigenvalues of the orientation tensor. The parameter C_I was auto calculated by Moldflow™. The parameter κ was set to 0.1 [17]. As the bundles initially are cut and randomly distributed on the surface of the paste, the in-plane random orientation for charge was used.

3.6 Result

All the observations of bundles in the charge confirm that the bundles were straight with minimal deflection at the end of the maturation zone (Figure 3-5).

Figure 3-5 Overview of the bundles in charge

The orientation through the thickness was calculated based on the cross section of local fibers (Figure 3-3) and the method was explained in fiber orientation through the thickness section. Based on this method, there was no pattern in the fiber orientation through the thickness as shown in Figure 3-7 and Figure 3-8. Also, the distribution of data points in graphs represents the non-random distribution of fiber through the thickness and existence of the resin-rich and fiber-rich regions through the thickness in micro scale (Figure 3-6). The bundles were 2.5 cm long, the same as initially cut. In the fiber orientation through thickness section, the single cross section of fiber represents the orientation of the whole fiber. However, the method explained the in-plane orientation section, is more reliable, because it considers the entire visible length of bundle in the x-y plane.

Figure 3-6 Overview of sample cross section

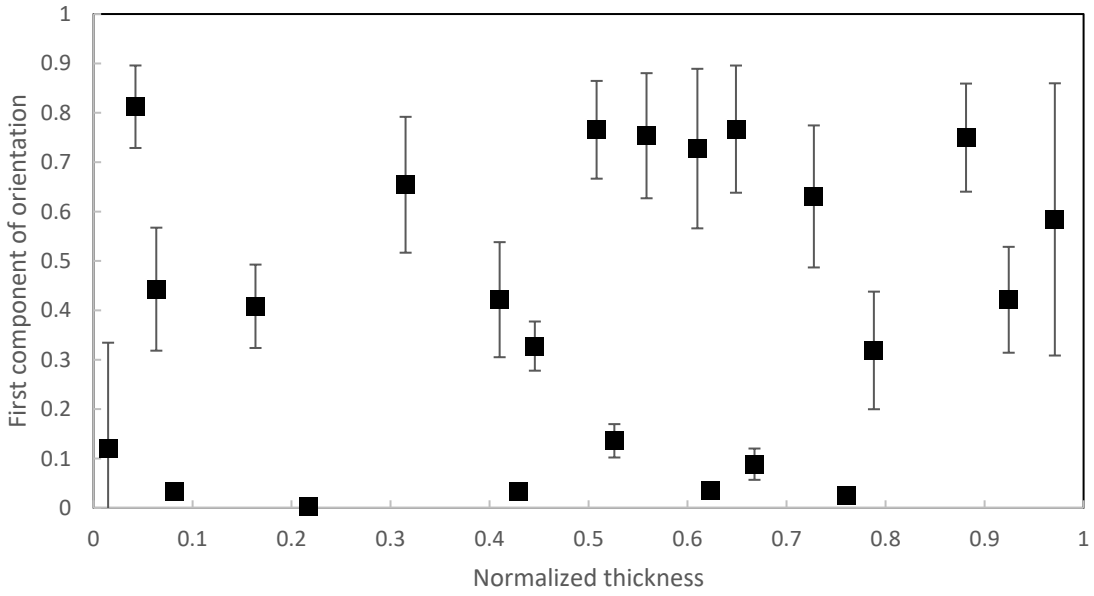

Figure 3-7 First component (x-x) of local fiber bundle orientation through the thickness at position M, where x and y are the planar directions and z is the thickness direction.

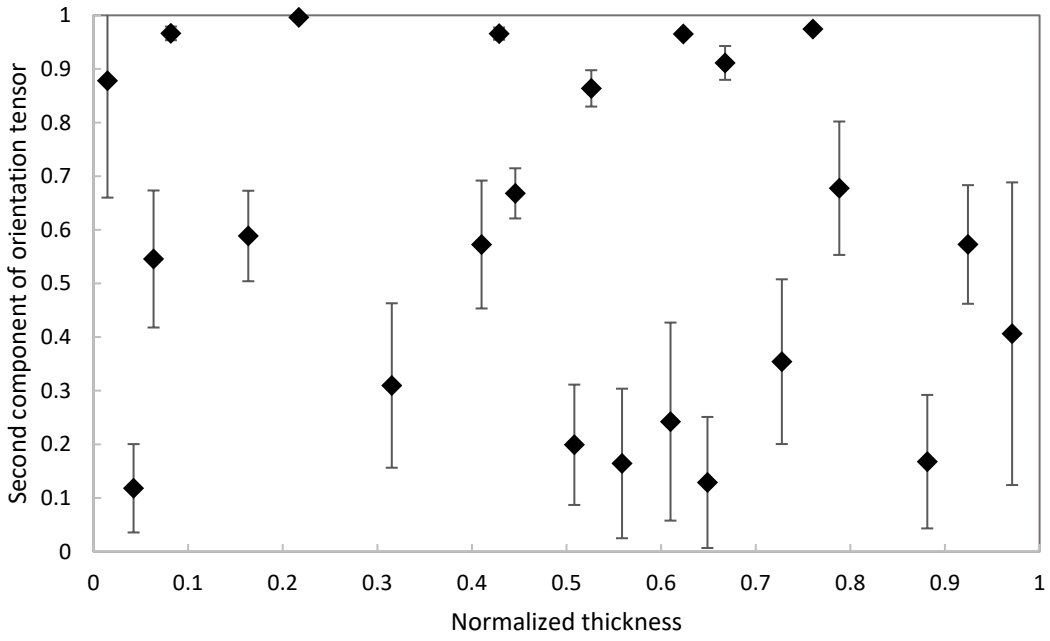

Figure 3-8 Second component (y-y) of local fiber bundle orientation through the thickness at position M, where x and y are the planar directions and z is the thickness direction.

The experimental sample observations confirm that the fiber bundles did not break and they generally held their cohesion through the maturation zone and after compression molding.

The compression molding slightly bent the bundles and deflection values are reported in Table 3-4 and Table 3-5 for 62 and 30 percent initial mold area coverages. The bundles at the middle and diagonal positions had lower deflection value than the edge (E) and corner (C) samples. Other researchers have also reported the same trend in orientation in compression molding [2, 3].

The width change (a^*) of the bundles increased during the compression molding as shown in Table 3-4 and Table 3-5, although there was no discernible trend at the different sample positions. The bundles flatten significantly up to 37 percent more than their initial width. Lee et al. reported the mean value of a^* = 1.48 for high flow length of 33cm [3]. Irrespective of the initial charge area coverage and the positions of the bundles, compression molding caused the flattening of the bundles, as expected. The higher values of the width change for the 30 percent initial mold area coverage were measured due to the higher flow length and higher ratio of initial charge thickness to final thickness.

Table 3-4 Microstructure parameters measured for charge and sheet at for 62 percent initial mold area coverage

Sample	Charge a_{xx}	a^*	δ^*
M	0.46	1.13	0.038
D		1.09	0.044
E		1.22	0.042
C		1.2	0.089

Table 3-5 Microstructure parameters measured for charge and sheet at for 30 percent mold area coverage

Sample	Charge a_{xx}	a^*	δ^*
M	0.45	1.2	0.034
D		1.23	0.039
E		1.23	0.081
C		1.37	0.121

Figure 3-9 and Figure 3-10 show the micro CT images through the thickness at M and E positions at two voxel sizes of 50 and 20 for 62 μm percent mold area coverage, respectively. All the bundles at middle positions remained almost straight through the thickness, but the bundles at the edge positions were bent. There was an accumulation of bundles at the edge because the mold walls stopped the flow.

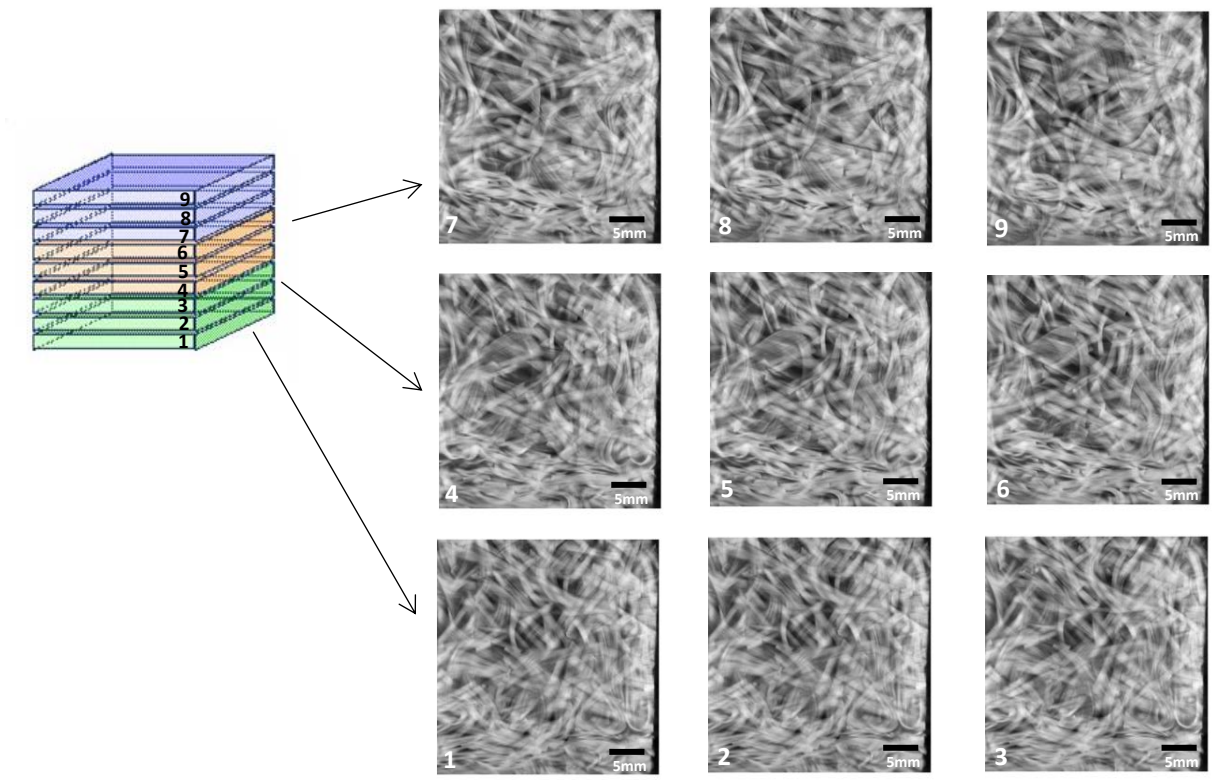

Figure 3-9 Micro CT of the E sample for 62 percent of initial mold area coverage (voxel size of 20 μ)

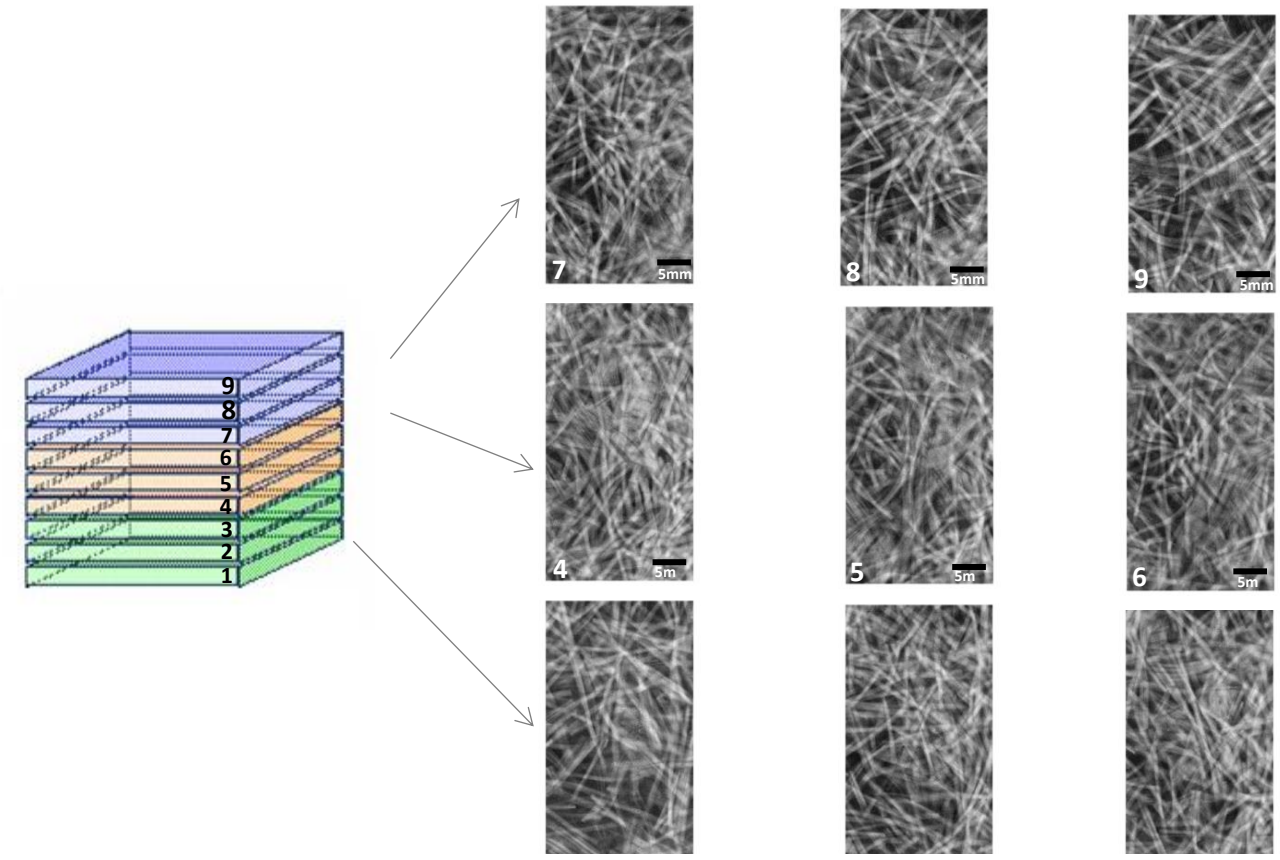

Figure 3-10 Micro CT of the M sample for 62 percent of initial mold area coverage (voxel size of 50 μ)

Moldflow simulation showed that the mold was filled in 1.2 seconds prior to curing and the rise in the temperature and viscosity happened after 5 seconds when the mold was filled and cure started (Figure 3-11). The same trend for the cure over the time in compression molding process of polyester SMC material was observed by Lee [24].

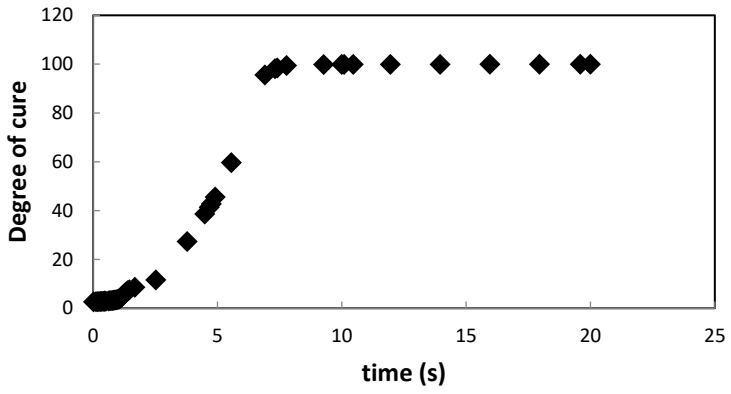

Figure 3-11 Average cure over time

Figure 3-12 to Figure 3-19 show the first component of orientation tensor through thickness for the samples at different positions for 30 and 62 percent initial mold area coverage. The second component of the orientation tensor is also available in the supplementary information. For 62 percent initial mold area coverage, the bundles do not significantly change their orientation compared to initial charge orientation shown in Table 3-4, because of the relatively short flow length during compression molding. Also, the higher orientation values for 30 percent initial mold area coverage confirmed the significance of flow length on the resulting orientation.

Figure 3-12 to Figure 3-13 show the fiber orientation predicted by the RSC model through thickness for sample M. The parameter a_{xx} represents the component of orientation tensor in the x-direction and a_{yy} represents the component of orientation tensor in the y-direction. The orientation components at the middle remained the same as the initial orientation due to low shear rate (c. 4 s^{-1}). The RSC model slowed down the fiber bundle orientation and the orientation did not significantly change during the process. However, the RSC model predicted random orientation through the mold thickness. The experimental orientation values which were measured experimentally from the micro-CT images (Figure 3-10) through the thickness were shown in Figure 3-12 to Figure 3-13. Orientation remained almost unchanged and random for 62 percent initial mold area coverage. For 30 percent initial mold area coverage, the RSC model predictions were in agreement with experimental values.

The first component of the orientation tensor for position E are shown in Figure 3-16 and Figure 3-17 for 30 and 62 percent initial mold area coverage. The experimental orientation values in postion E are in disagreement with the RSC model. The bundles accumulated near the edge

perpendicular to the flow direction as shown in Figure 3-9. Near the edge regions the flow collides with the wall, it is suddenly stopped while flow continues to fill in the neighbouring area. Therefore, bundles near the wall were still exposed to flow because though the wall is an obstacle, bundles reoriented in the direction parallel to the wall.

The results from the RSC model and experiments were in relatively good agreement except for E samples. Bundles within sample C oriented more than other positions.

The existence of resin rich layer at mold surfaces lubricated the relative motion between mold and SMC. Baron and Caulk showed that this layer represents the hydrodynamic friction and slip boundary and in a big surface area and thin thickness mold, the effect is more significant [25, 26]. In SMC process in this work, the temperature of mold surfaces (140 °C) was more than the charge (50 °C). Immediately after charge touched the hot surfaces of the mold, the heat conducted to the adjacent resin rich layer and served as slip layers. Therefore, the charge during filling process underwent the extensional flow which led to constant orientation distribution through the thickness. The result is also consistent with Barone and Caulk's work [26].

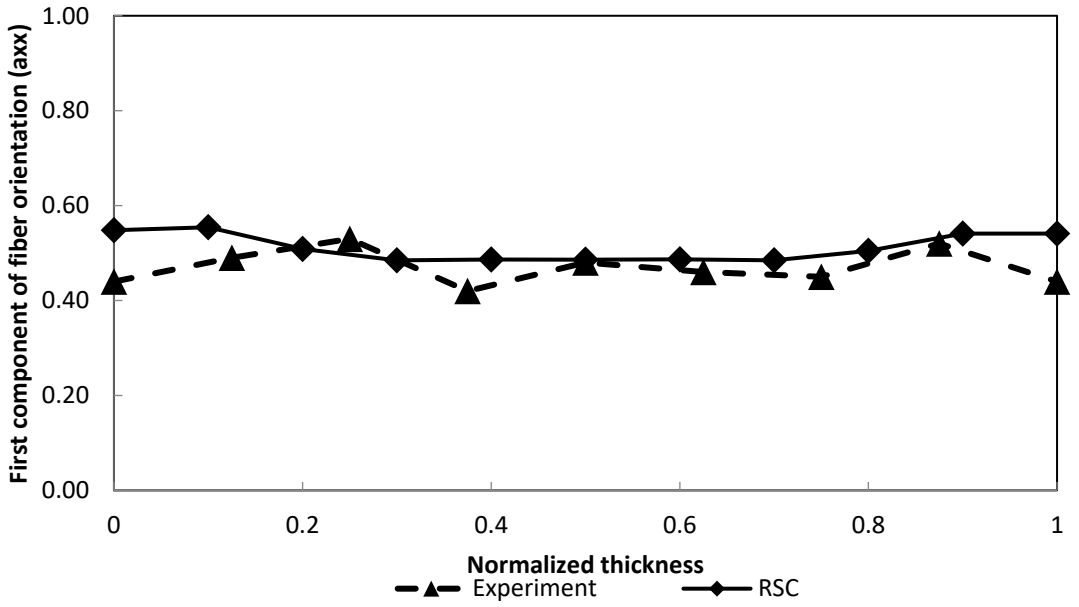

Figure 3-12 First component of fiber orientation for sample M of 62 percent of initial mold area coverage

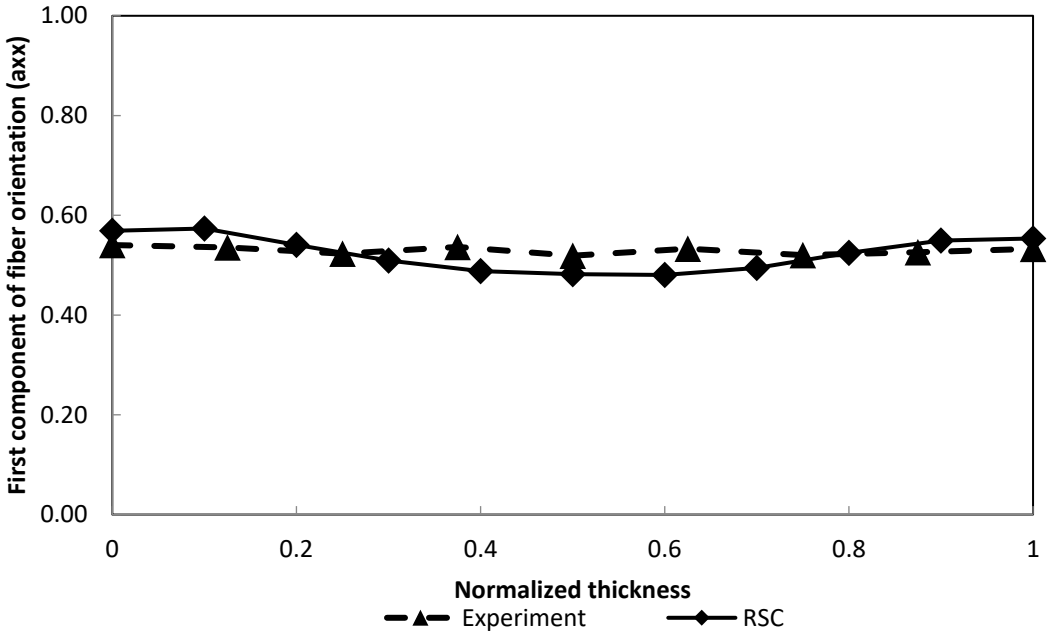

Figure 3-13 First component of fiber orientation for sample M of 30 percent of initial mold area coverage

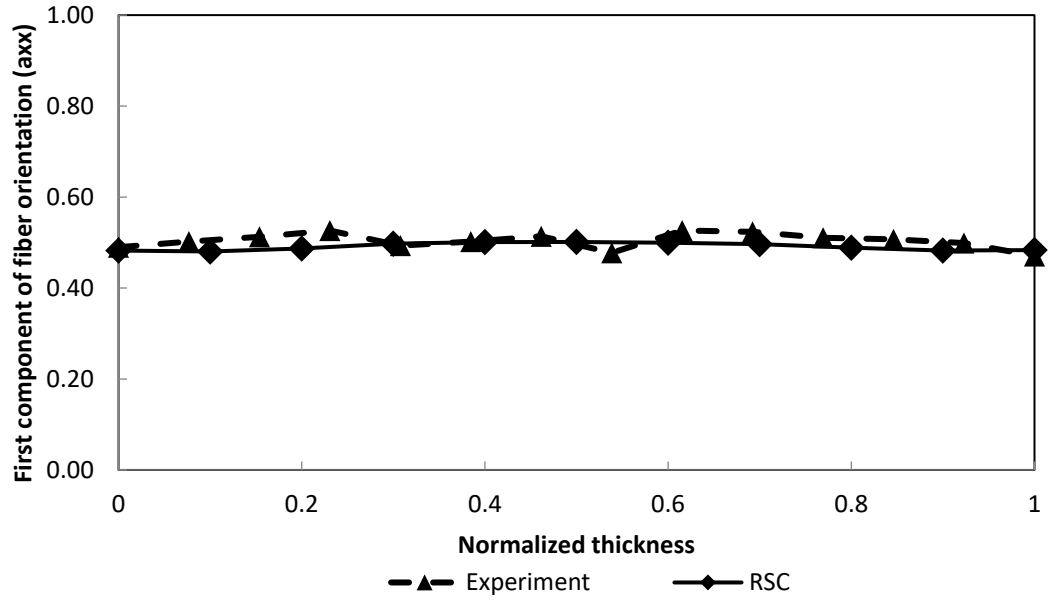

Figure 3-14 First component of fiber orientation for sample D of 62 percent of initial mold area coverage

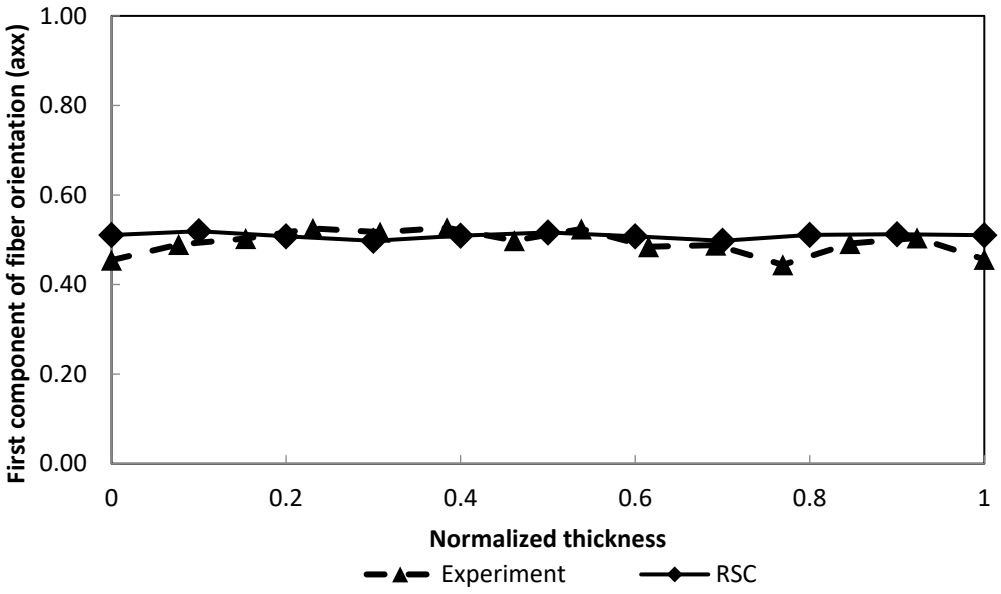

Figure 3-15 First component of fiber orientation for sample D of 30 percent of initial mold area coverage

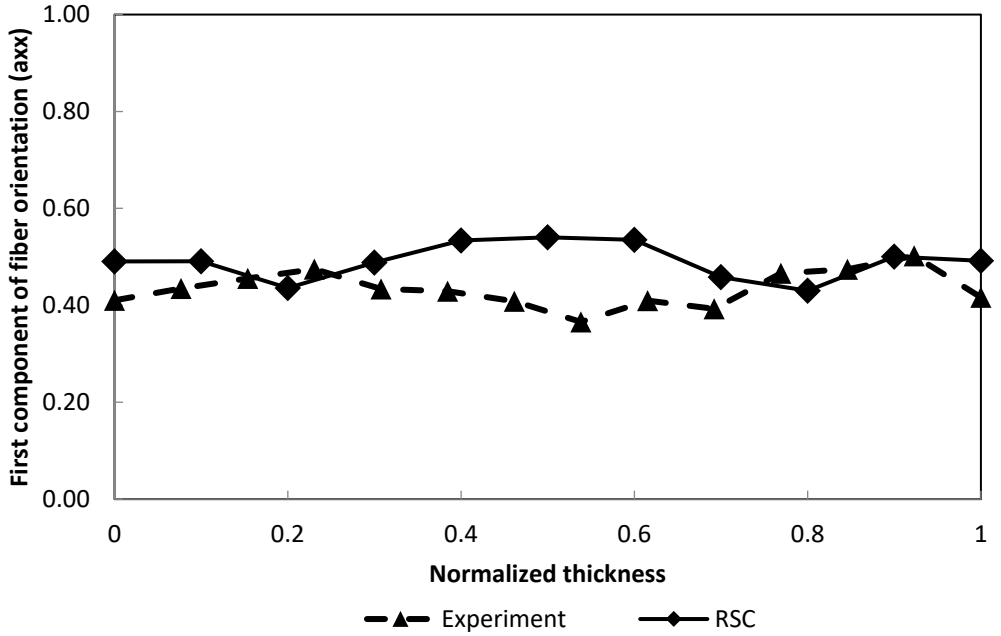

Figure 3-16 First component of fiber orientation for sample E of 62 percent of initial mold area coverage

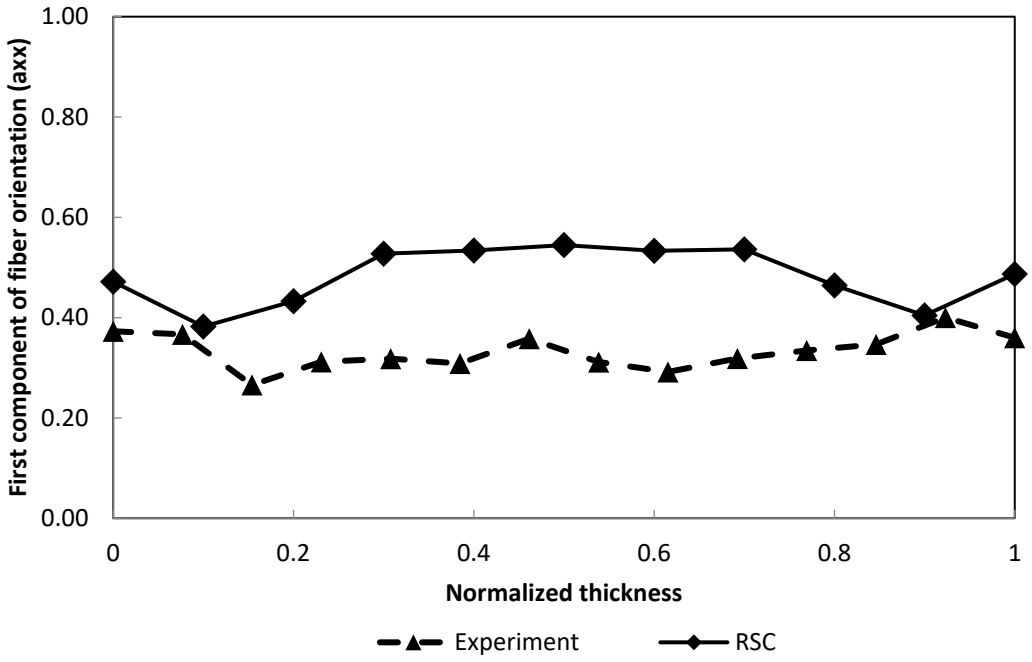

Figure 3-17 First component of fiber orientation for sample E of 30 percent of initial mold area coverage

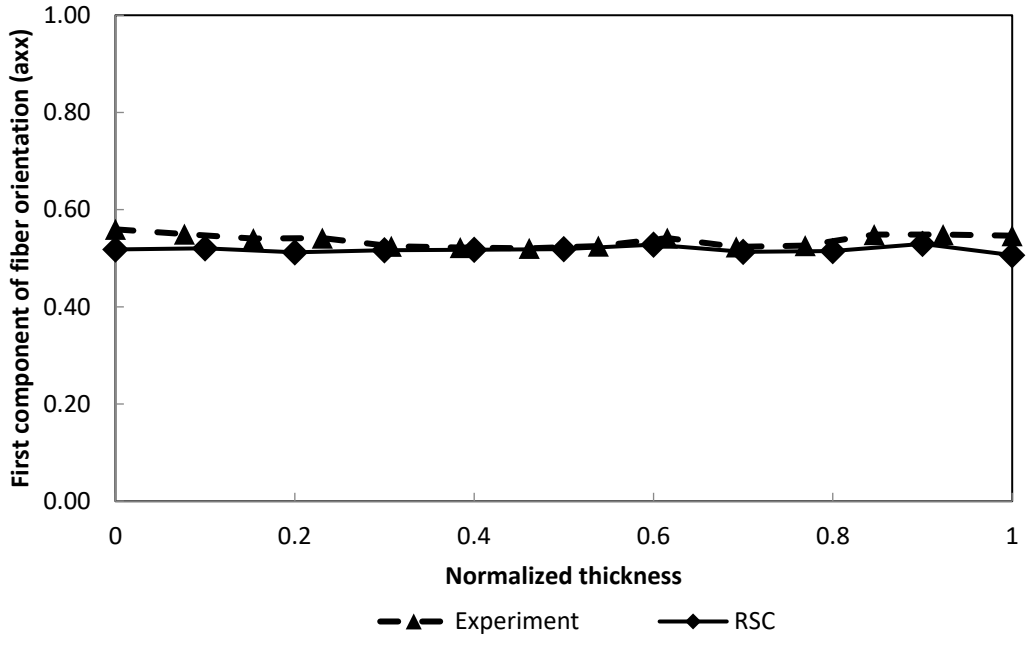

Figure 3-18 First component of fiber orientation for sample C of 62 percent of initial mold area coverage

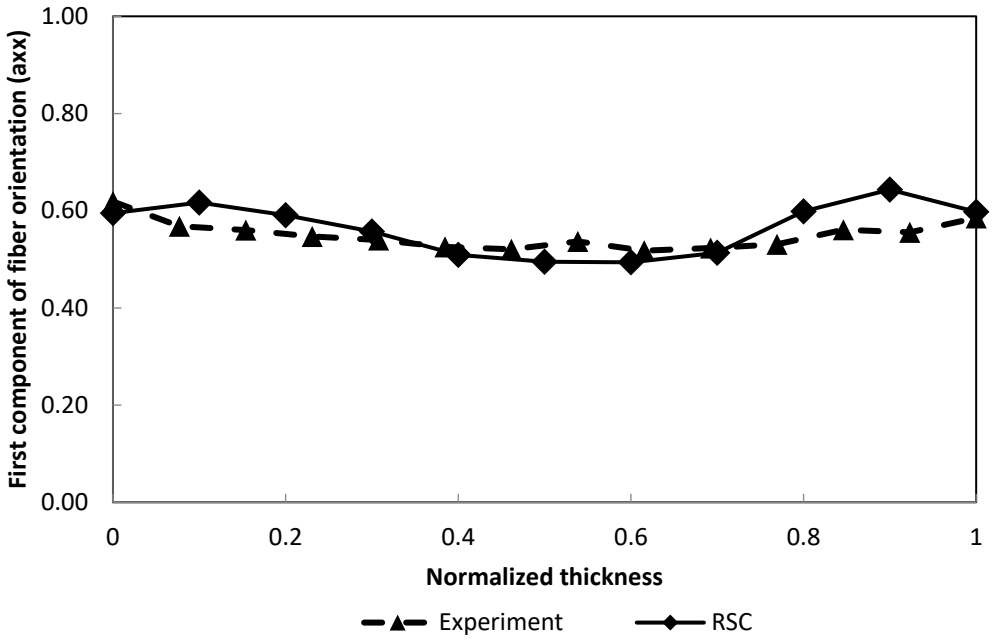

Figure 3-19 First component of fiber orientation for sample C of 30 percent of initial mold area coverage

3.7 Conclusions

In the D-SMC process, the microstructure of 20 percent volume fraction of long bundles was studied before and after processing. The bundles kept their cohesion in the maturation zone and during compression. The microscopy analysis of the charge bundles showed that they remained relatively straight and formed a network of highly connected bundles.

Regardless of the position and initial charge coverage, the bundles flattened in the compression molding process. The bundles flattened up to 37 percent of the initial width in the position C of the 30 percent initial mold area coverage. Overall, the measured deflection of bundles, δ^*, is not significant in the compression molding process. The length measurement confirms that bundles did not break during the process.

Moldflow simulation predicted the resulting fiber tow orientation using the RSC model. Measured values of orientation from micro CT analysis confirm final random orientation for 62 percent initial mold area coverage. The higher values of the first component of orientation tensor in 30 percent initial mold area coverage compared to 62 percent initial mold area coverage confirms the significant effect of flow length on bundle orientation. High volume fraction of long bundles along

with short flow lengths impede bundle orientation far from the random orientation, which is of crucial importance in the design of the complex parts.

3.8 References

[1] Dumont P, Orgéas L, Le Corre S, Favier D. Anisotropic viscous behavior of sheet molding compounds (SMC) during compression molding. International Journal of Plasticity 2003;19:625–46.

[2] Dumont P, Vassal J-P, Orgéas L, Michaud V, Favier D, Månson J-AE. Processing, characterisation and rheology of transparent concentrated fibre-bundle suspensions. Rheologica Acta 2007;46:639–51.

[3] Le T-H, Dumont PJJ, Orgéas L, Favier D, Salvo L, Boller E. X-ray phase contrast microtomography for the analysis of the fibrous microstructure of SMC composites. Composites Part A: Applied Science and Manufacturing 2008;39:91–103.

[4] Han CD. Rheology and processing of polymeric materials. 2007.

[5] Davis BA. Compression molding. 2003.

[6] Dweib MA, Brdaigh CM. Compression molding of glass reinforced thermoplastics: Modeling and experiments. Polymer Composites 2000;21:832–45.

[7] Tseng S-C, Osswald TA. Prediction of Shrinkage and Warpage of Fiber Reinforced Thermoset Composite Parts. Journal of Reinforced Plastics and Composites 1994;13:698–721.

[8] Guiraud O, Orgéas L, Dumont PJJ, Rolland du Roscoat S. Microstructure and deformation micromechanisms of concentrated fiber bundle suspensions: An analysis combining x-ray microtomography and pull-out tests. Journal of Rheology 2012;56:593.

[9] Chalencon F, Orgéas L, Dumont PJJ, Foray G, Cavaillé J-Y, Maire E, et al. Lubricated compression and X-ray microtomography to analyse the rheology of a fibre-reinforced mortar. Rheologica Acta 2009;49:221–35.

[10] Guiraud O, Dumont PJJ, Orgéas L, Favier D. Rheometry of compression moulded fibre-reinforced polymer composites: Rheology, compressibility, and friction forces with mould surfaces. Composites Part A: Applied Science and Manufacturing 2012;43:2107–19.

[11] Latil P, Orgéas L, Geindreau C, Dumont PJJ, Rolland du Roscoat S. Towards the 3D in situ characterisation of deformation micro-mechanisms within a compressed bundle of fibres. Composites Science and Technology 2011;71:480–8.

[12] Centea T, Hubert P. Modelling the effect of material properties and process parameters on tow impregnation in out-of-autoclave prepregs. Composites Part A: Applied Science and

Manufacturing 2012;43:1505–13.

[13] Centea T, Hubert P. Measuring the impregnation of an out-of-autoclave prepreg by micro-CT. Composites Science and Technology 2011;71:593–9.

[14] Bernasconi a., Cosmi F, Hine PJ. Analysis of fibre orientation distribution in short fibre reinforced polymers: A comparison between optical and tomographic methods. Composites Science and Technology 2012;72:2002–8.

[15] Jackson WC, Advani SG, Tucker CL. Predicting the Orientation of Short Fibers in Thin Compression Moldings. Journal of Composite Materials 1986;20:539–57.

[16] Advani SG, Tucker CL. The Use of Tensors to Describe and Predict Fiber Orientation in Short Fiber Composites. Journal of Rheology 1987;31:751–84.

[17] Wang J, O'Gara JF, Tucker CL. An objective model for slow orientation kinetics in concentrated fiber suspensions: Theory and rheological evidence. Journal of Rheology 2008;52:1179.

[18] Malnati P. Formulation flexibility: Direct-SMC. Http://www.compositesworld.com/articles/formulation-Flexibility-Direct-Smc 2012.

[19] Motaghi A, Hrymak A, Motlagh GH. Electrical conductivity and percolation threshold of hybrid carbon/polymer composites. Journal of Applied Polymer Science 2015;132:n/a-n/a.

[20] Bay RS, Tucker CL. Stereological measurement and error estimates for three-dimensional fiber orientation. Polymer Engineering and Science 1992;32:240–53.

[21] Abràmoff MD, Hospitals I, Magalhães PJ, Abràmoff M. Image Processing with ImageJ n.d.

[22] Haider M, Hubert P, Lessard L. Cure shrinkage characterization and modeling of a polyester resin containing low profile additives. Composites Part A: Applied Science and Manufacturing 2007;38:994–1009.

[23] Wang J, Jin X. Comparison of recent fiber orientation models in autodesk moldflow insight simulations with measured fiber orientation data. Polymer Processing Society 26th Annual 2010.

[24] Lee LJ. Curing of compression molded sheet molding compound. Polymer Engineering and Science 1981;21:483–92.

[25] Barone MR, Caulk DA. A Model for the Flow of a Chopped Fiber Reinforced Polymer Compound in Compression Molding. Journal of Applied Mechanics 1986;53:361.

[26] Barone MR, Caulk DA. Kinematics of flow in sheet molding compounds. Polymer Composites 1985;6:105–9.

4 Simulation of Compression Molding of Direct-Sheet Molding Compound

This chapter was presented at International Composite Research Center Conference (ICRC), Germany, 2016

4.1 Objective

The direct sheet molding compound (D-SMC) process provides products with a high volume of fiber bundles with enhanced properties. The Carreau viscosity model has been shown to capture the viscosity behavior of the D-SMC paste. A viscosity model for suspensions of high volume percentage of planar randomly oriented glass bundles is introduced to describe the material viscosity behavior in the process and is used to simulate the filling process. An open source CFD software package, OpenFOAM, is used to solve the equation of mass and momentum, along with the viscosity model, by the volume of fluid technique in the three-dimensional system. OpenFAOM has a great advantage of code customization and in this study, the rheology model for the in-plane randomly fiber bundles suspensions is introduced to OpenFOAM to simulate the compression molding flow of highly concentrated fiber bundles for two phases. OpenFOAM is also used to simulate the single bundle movement and deformation in the compression molding flow at different positions in the mold. Finally, compression molding experiments are done for D-SMC material to study flow and fiber movement through the process for different initial charge mold coverage.

4.2 Simulation

4.2.1 Methodology

Prediction of flow details in the compression process is essential for an industrial application. The open source computational fluid dynamic package (OpenFOAM—Open Source Field Operation and Manipulation) was used to study a compression mold filling by the volume of fluid method (VOF) in a three-dimensional system [1]. The discretization of mass and momentum equations is based on the finite volume method (FVM) a polyhedral mesh [2].

The *interDyMFoam*/*interFoam* solvers in OpenFOAM-2.1.1, based on FVM, solved the conservation of mass and momentum [1]. The *interDyMFoam* solver is similar to *interFoam*, but is able to handle mesh motion and changes in mesh topology including adaptive re-meshing. The solvers apply the volume of fluid method for two immiscible fluids with a defined interface. The volume of fill fraction of domains represents the fraction of different fluids within a finite volume ($\alpha_f = 1 - \alpha_a$).

The equations of mass and momentum for an incompressible fluid describe the system using the local properties (density and viscosity);

$$\nabla.(u) = 0 \tag{4-1}$$

$$\frac{\partial \rho u}{\partial t} + \nabla.(\rho u u) = -\nabla P + \rho g + \nabla.(\eta \nabla u) + f_\alpha \tag{4-2}$$

Where u, ρ and η are the velocity vector, density and viscosity, respectively. Another equation is added to solve simultaneously for the volume fraction at the interface.

$$\frac{\partial \alpha_f}{\partial t} + \nabla.(\alpha_1 u) + \nabla.\left[u_c \alpha_f \left(1 - \alpha_f\right)\right] = 0 \tag{4-3}$$

The u_c is the compression velocity and an additional term in conservation equations to capture the defined interface between two fluids. The parameter of density and viscosity in equation (4-1) to (4-3) are the local volume fraction average.

$$\rho = \alpha_f \rho_f + \alpha_a \rho_a \text{ and } \eta = \alpha_f \eta_f + \alpha_a \eta_a \tag{4-4}$$

The f_α in equation (4-2) is based on the continuum surface force model and represents the interfacial tension force density at the interface where α_f is between 0 and 1 and $f_\alpha = 0$ elsewhere in the domain [3]. The PIMPLE algorithm (pressure implicit method for pressure linked equations) numerically solves the system, which is the combination of PISO algorithm (pressure implicit split operator) and SIMPLE (semi implicit methods pressure linked equations).

The calculations are performed using a self-adapting time step to ensure the stability of the solution. This value is adjustable and based on Courant number, which is defined as $Co = (u/\Delta x)\Delta t$ where Δt is the time step and Δx is the size of the mesh in the direction of velocity, u. The Courant number should be less than 1 at all times of simulation to ensure convergence of the solution. The initial mesh and time step of 0.005 fulfill the Courant number limitation. During the simulation, the solver automatically varies the time step to ensure the Courant number stays below 1.

4.2.2 Geometry generation and mesh

Figure 4-1 shows the schematic of the mold and charge. The square mold with a dimension of 45.7cm contains 100 cells in width and length with 10 layers through the thickness to discretize the problem. The charge initial thickness is 5mm and 11.2 mm for 62 percent and 30 percent coverage of the mold area and is located at the center of a mold [4]. The upper surface of the mold closes at a speed of 1mm/s. The *dynamic mesh dictionary* in the *interDyMFoam* solver manipulates the dynamically changing geometry and re-meshing [1,5].

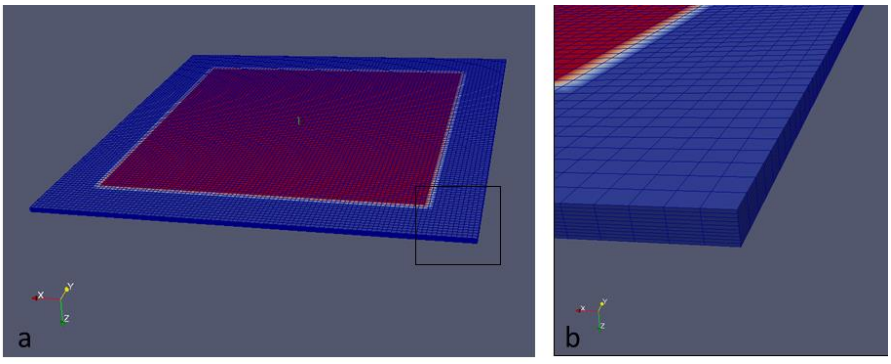

Figure 4-1 Schematic of mold geometry and position of the initial charge

The analysis of mesh dependency on simulation result has been done in the simulation domain. The simulation was run on the initial mesh size of 100 by 100 cells in width and 10 through the

thickness and the velocity residuals were below 10^{-7}. The mesh was refined to 2 times of initial mesh to study the mesh dependency. The velocity residual error was below 10^{-7} and the maximum velocity difference at middle position was less than 0.5 percent. Therefore, comparing the residuals showed that the optimum mesh as a matter of time and accuracy was 100 by 100 cells in width and length and 10 through the thickness.

4.2.3 Boundary conditions

Boundary conditions define the velocity and pressure at the walls, upper and lower surfaces of the mold and at the surfaces of fluid touching the mold. The velocity boundary condition includes 1 mm/s for the upper surface as a closing speed and the bottom surface is static and no-slip boundary condition for the surfaces of fluid (α_f) touching the mold planes. A total value of pressure for the region is set to zero. Total pressure is defined as $P = P_0 + \frac{1}{2}\rho|u|^2$, where P_0 is the atmospheric pressure and when u changes, P is adjusted accordingly [1].

4.2.4 Constitutive equation

The rheology of the in-plane randomly oriented bundles within the resin is a result of an interaction mechanism between bundles at contact points. The interaction forces are the sum of friction and lubrication at contact points. The proposed model by Servais et al. for the viscosity η is

$$\eta = \frac{k_f P_n}{\dot{\gamma}} + k_h \frac{16}{\pi^2}\frac{a}{b^2\alpha_\eta} f V_f^2 \eta_0 \left[1 + \left(\lambda \frac{a}{\alpha_\eta}\dot{\gamma}\right)^2\right]^{\frac{n-1}{2}} \qquad (4\text{-}5)$$

where $\dot{\gamma}$ is the shear rate and, P_n is the normal packing stress [6] . The first term on the right hand side of (4-5) represents the frictional force between fiber bundles, where k_f is the friction coefficient. The second term represents the hydrodynamic lubrication force where k_h is the coefficient of hydrodynamic lubrication and α is the average shearing thickness of the compound around the contacting bundles. The constants of η_0, λ and n are Carreau parameters of the paste. ϕ_b is the volume fraction of bundles in the compound. The a and b are the minor and major axis of the bundles. The parameter f is a distribution function of in-plane bundle orientation, and its value is 0 for perfect alignment and $2/\pi$ for in-plane random orientation [6]. The proposed rheology model includes a yield stress at low shear rate (<0.1 s^{-1}) and a power law behavior at high

shear rates (>10 s^{-1}). For example, the frictional term of the viscosity is dominant in the behavior of the D-SMC material as the shear rate is not high in compression molding.

Packing stress is the result of the average force of interaction within the bundle network. The packing stress, P_n, cannot be derived analytically for the fiber bundles; therefore, the value was measured experimentally. Servais et al. and Toll [6,7] measured the packing stress as a function of volume fraction of bundles. Result by Servais showed that packing stress is higher for a dry network of bundles than impregnated bundles because of lubricating effect at contact points. Also, it was shown that the packing stress is identical for the system of resin with two different viscosities. In this study, the P_n value for 20 percent volume fraction of bundles was used for the chopped glass bundles with the similar bundle dimensions. The yield stress in the highly concentrated fiber bundles exists due to the first term that captures friction between bundles in equation (4-5).

The flow simulation model is based on the assumption that the bundles contain a uniform straight length and number of fibers, which are well dispersed in the system. Experiments by Servais et al. [6] the bundles deform at lower normal packing stress and do not deform when further high stress applied. Therefore, the bundles have constant and fixed minor and major axes. Another assumption is that the flow does not affect the bundle cross section and volume fraction of bundles. The stress direction is perpendicular to the minor axis, and bundles cannot rotate about their own axis because of the resistance due to the contact points through the length of the bundles. Bundles are assumed to be square packed and incompressible at the contact points [6].

The lubrication term is based on the paste rheology, which is assumed to follow the Carreau model:

$$\eta = \eta_0[1 - (\lambda\dot{\gamma})^2]^{(n-1)/2} \qquad (4\text{-}6)$$

η_0 is the zero shear viscosity, and λ is the time constant, and n is the power law index.

An SMC paste is prepared using the ingredients shown in Table 4-1. The parallel plate rheometer (Rheometrics model RDS-II) in a rotational mode with shear rates of 0.5 to 100 (1/s) at 60°C similar to processing conditions measures the viscosity of the paste. The diameter of the plate is 25mm with a gap of 0.75mm.

Table 4-1 Formulation of D-SMC paste

Raw Material	Grade	Supplier	[wt.-%]
Unsaturated polyester Resin	T320	AOC Inc.	23.05
Low profile additives	LS N640	AOC Inc.	15.37
Peroxide	Trigonox C	AkzoNobel	0.42
Wetting Agent	W 996	BYK	1.54
Internal Mould Release	Ceasit Ca stearate	Baerlocher	1.92
Water			0.08
Filler ($CaCO_3$)	FL5	Omyacarb	57.63
Thickening Powder	Magchem 200AD	Magnesia Specialties	0.46

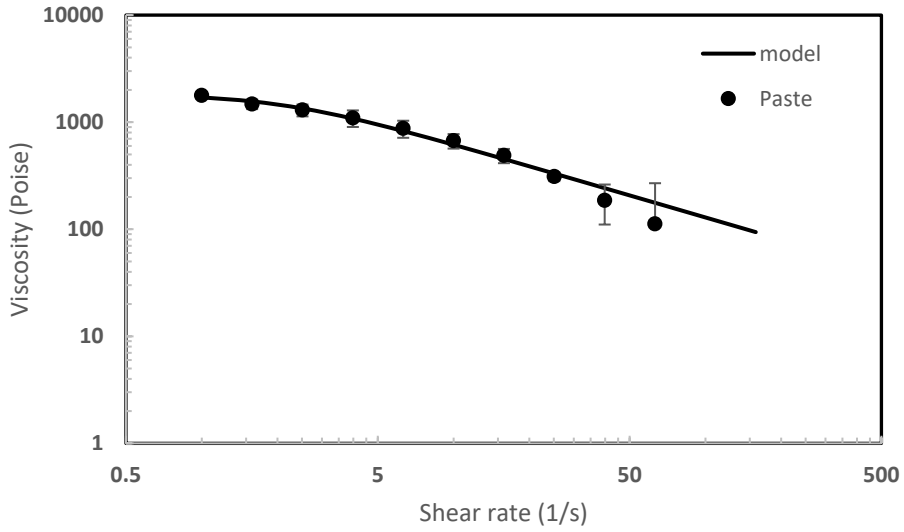

Figure 4-2 Shear viscosity of D-SMC paste

Figure 4-2 shows the shear viscosity of D-SMC paste. The parameters of Carreau model are found by minimizing the sum of squared errors. The fitted Carreau model parameters are given in Table 4-2. The trend and parameters are in agreement with other findings for a similar compound [8].

Servais et al. [6] concludes that k_h and k_f do not depend significantly on bundle volume fraction but k_h depends on the viscosity of the resin. The parameters of k_h and k_f were used from the system of similar zero viscosity resin as shown in as shown in Table 4-2. The proposed viscosity model is introduced to the library of *transportProperies* in OpenFoam and compiled with the available solvers.

Table 4-2 Parameters of viscosity model

$k_f\ (-)^1$	0.09	$a(mm)$	0.1
$k_{\mathrm{h}}(mm^2)^1$	0.53	$b(mm)$	0.5
$P\ (Pa)^1$	10000	$\alpha(\mu)^1$	0.27
$f(-)$	$2/\pi$	$\eta_0\ (poise)$	1830
$\phi(-)$	0.2	$\lambda\ (s)$	0.481
$\rho\ (\frac{g}{cm^3})$	1.86	$n(-)$	0.315

[1] data from reference [6]

4.3 Results for compression molding

In this study, the simulation for compression molding is performed at an isothermal temperature (60 °C), because the mold fills quickly, and the paste cures after completion of molding [9]. Four positions were chosen to report the results, as shown in Figure 4-3, with the coordinates given in

Table 4-3.

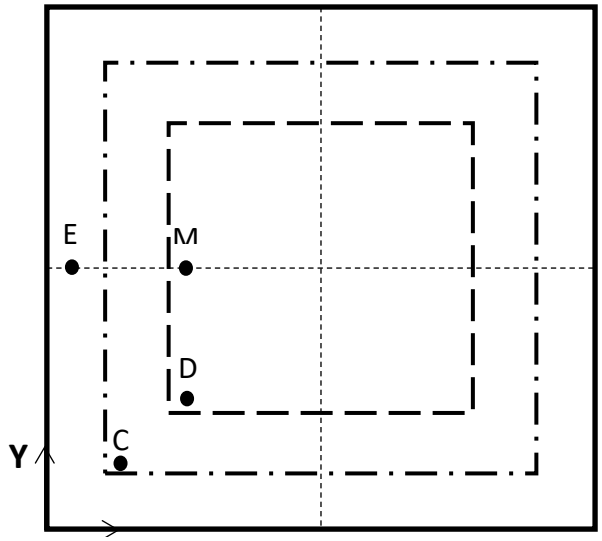

Figure 4-3 Points of interest in the sheet; D: diagonal, M: middle, E: edge, C: corner, positions of the initial charge (30 percent mold area coverage (— · —) , 62 percent mold area coverage (— — —), middle line (----)

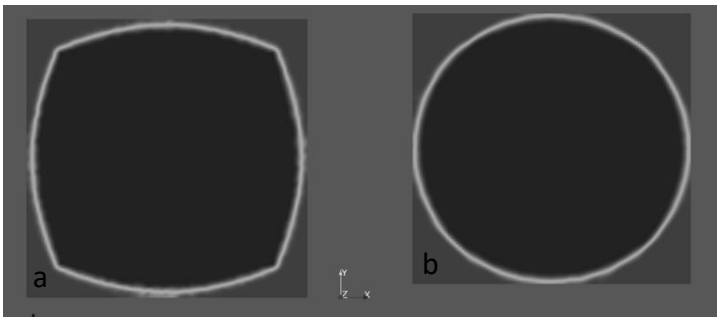

Figure 4-4 b) Resulting charge edge at 1.2s from 62 percent mold area coverage, d) resulting charge edge at 6.8s from 30 percent mold area coverage

Table 4-3 Coordinates of points of interest

Position	x (cm)	y (cm)
M	11.42	22.85
D	11.42	11.42
E	2.42	22.85
C	6	6

Figure 4-4a and b show the charge shape at 1.2 and 6.8 seconds for 62 percent and 30 percent initial mold coverage, respectively. The results are qualitatively similar to the work done by Lee et. al [10]. After 1.2 seconds for 62 percent coverage and 6.8 seconds for 30 percent coverage, the charge first touches the walls of the mold (Figure 4-4 a and b). It is clear that the corners of the charge do not reach the mold wall at the same time as the edge. If the whole charge experiences the same flow length, the properties of the final part will be more homogenous. There is a principle sometimes used in mold design to try to keep flow paths similar.

All the reported velocities in this chapter are the magnitude of the velocity vector. Figure 4-5 shows the velocity at different positions at 1.2 seconds. Positions M and E have the higher velocity because they are in the direction of flow. There is even highest velocity for E because of less flow resistance ahead of the E position. The similar trend of velocity was also reported by Lee et al. [11]. Figure 4-6 shows the velocity profiles for 62 percent initial mold coverage through the thickness for positions M and D after 0.5 and 1.2 seconds. Velocity at position M is higher than position D because M is in the direction of the fluid. Moreover, the velocity at both positions increase with time because the gap is getting smaller with the same volume of fluid. At all positions of the mold, plug flow defines the velocity profiles in the thickness direction.

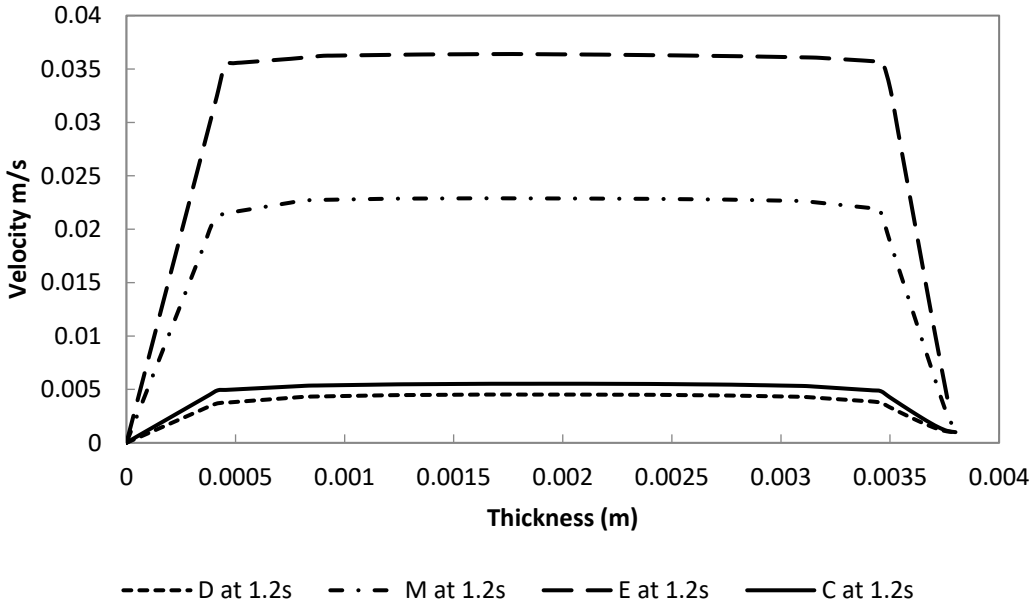

Figure 4-5 Velocity for 62 percent initial mold area at different positions after 1.2 seconds

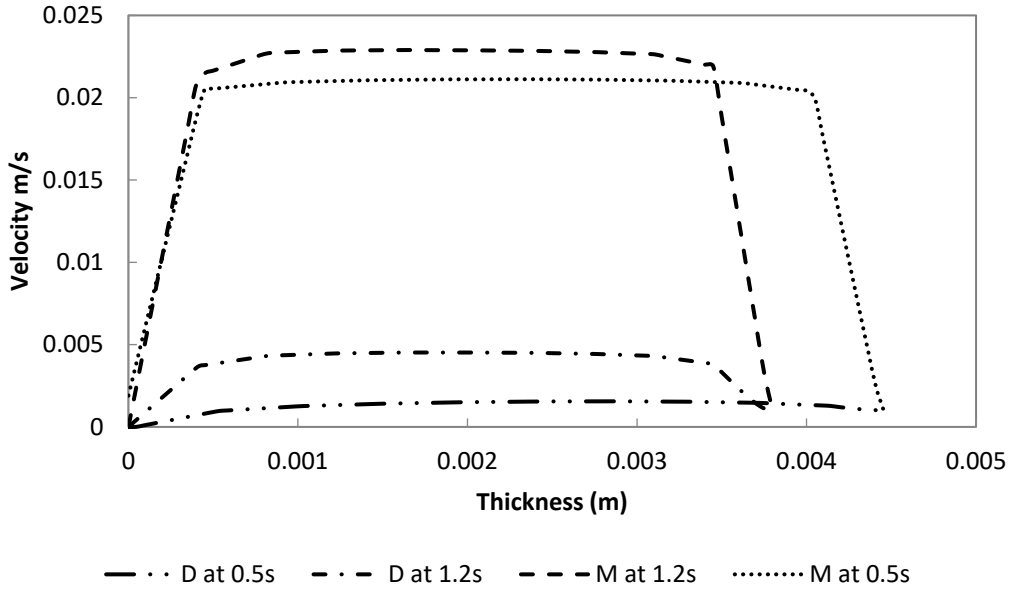

Figure 4-6 Velocity profile for 62 percent initial mold area coverage through the thickness at M and D positions

Figure 4-7 Figure 4-8 show the velocity profiles when the charge covers 30 percent of the mold. The E and D positions experience higher velocity because they are close to the flow front, and there is less flow resistance ahead of them (Figure 4-8). Lee et. al. studied the compression molding of similar systems, and the trend of velocity profile through the thickness is in agreement with the

above-mentioned results [11]. Many studies have confirmed that the flow is predominantly extensional in squeezing the SMC with different closing speeds [12–14].

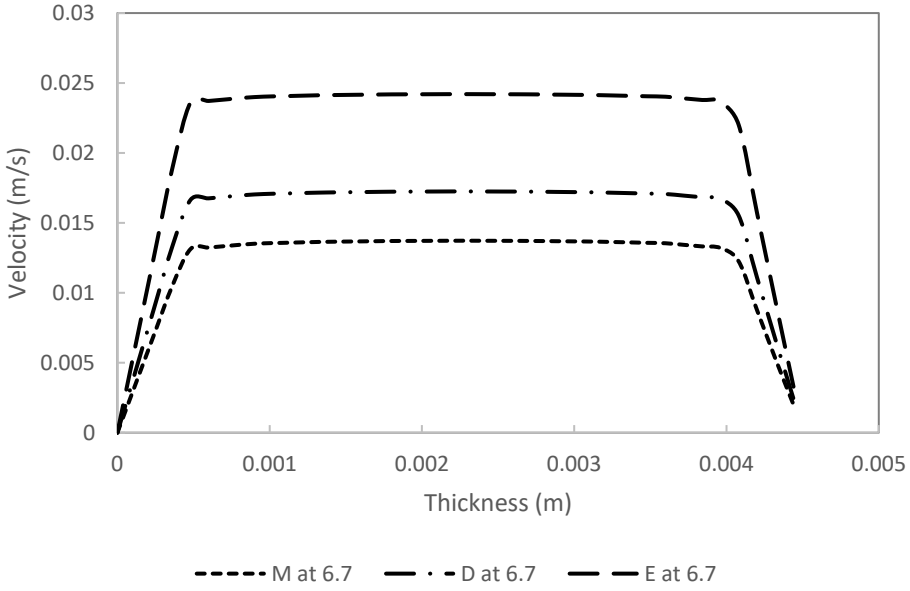

Figure 4-7 Velocity profile for 30 percent initial mold area coverage at different positions after 1.2 seconds

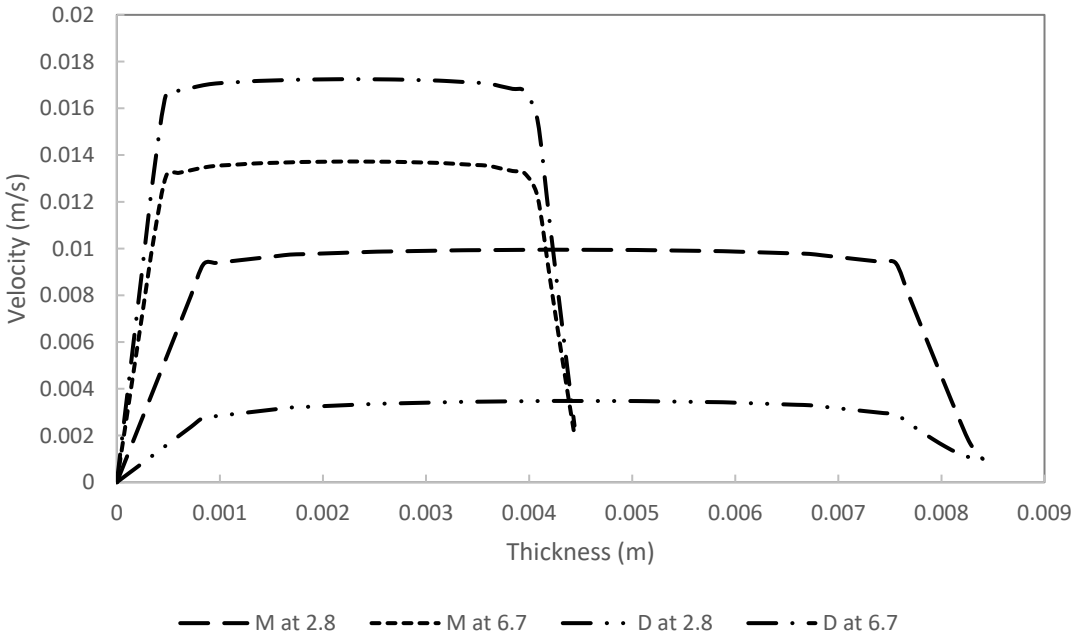

Figure 4-8 Velocity profile for 30 percent initial mold area coverage through the thickness at M and D positions

Figure 4-9 shows the compression molding pressure over the strain rate. The graph compares the pressure from experiments in the literature to the OpenFOAM simulation. The OpenFOAM

pressure is averaged through the half width of mold at a different stage of closing. Servais et al. [15] measured compression molding pressure over the strain rate for polypropylene containing 11 percent volume fraction of glass bundles and Kotsikos et al. [12] also reported the compression molding pressure for SMC at 70 °C (Figure 4-9). The chosen data from the literature are similar to the OpenFOAM simulation in terms of initial separation of the plate and closing speed. The experimental pressures are in agreement with the pressure from OpenFOAM.

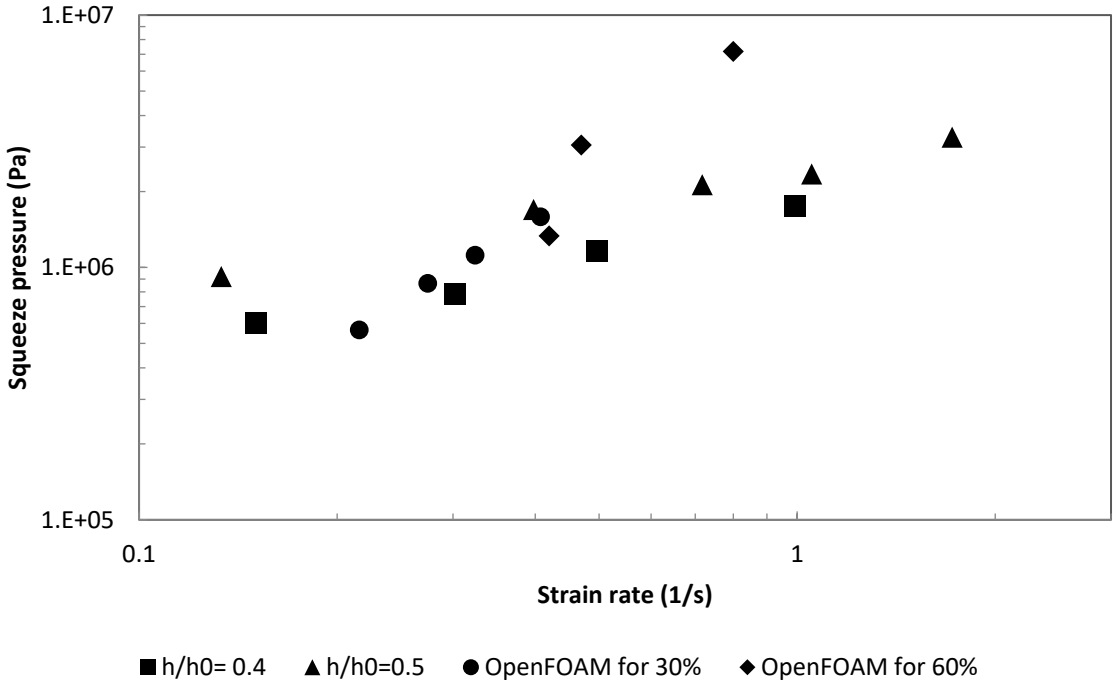

Figure 4-9 Compression molding pressure versus strain rate

Figure 4-9 shows the compression molding pressure over the plate separation for SMC and OpenFOAM simulation at the closing speed of 1mm/s. Kotsikos et al. [12] reported the pressure for compression molding of SMC charge to 0.25 initial charge thickness. Both data points are in agreement in terms of trend and value. The pressure increases when the mold is closing and being filled. Kau et al. [16] measured the higher value for pressure during compression molding of SMC.

4.4 **Simulation of single bundle deformation in the flow**

Compression molding provides a high quality of final parts because of highly concentrated fiber bundles. Bundles are randomly distributed in the plane of charge and in contact at multiple points along the bundle length. Detailed simulation of bundle deformation and orientation is a complex

phenomenon because bundles are relatively long (a few cm) and include hundreds of fibers. Bundles form a connected network, which cannot easily re-orient and rotate [30]. Image analysis of the final parts show that the bundle width changed due to compression, but there were no significant changes in overall orientation during molding [17].

Numerous entanglements of bundles because of the long length, and bundle impregnation with paste in the maturation zone cause bundles to move at the same velocity as the paste during mold filling. Moreover, plug flow and lack of a shear region support the assumption that bundles move along with the flow.

In the following simulations using the previously described model within OpenFOAM, bundles are assumed as a very viscous fluid with a kinematic viscosity of 500 m^2/s and density of 2.5 g/cm^3 (compared to the paste with the Carreau viscosity model and density available in Table 4-2) that could move and deform while mold filling. The major and minor axes of the bundles are measured 0.87 and 0.08mm, respectively, with a length of 2.5 cm. Using very fine mesh to distinguish the bundles in the domain causes the simulation time to increase dramatically. In addition, the difference in scale of mold (457.2 by 457.2 mm) and bundle dimensions causes instability in the Courant number and solution. Therefore, a smaller size of the mold (5 by 5 cm) and the same thickness is used defined in OpenFOAM. The *InterDyMFoam* cannot simulate more than two phases of fluid. Therefore, the whole open mold initially is already filled by a charge with bundles at different locations. The thickness of charge is 5mm and simulation starts by closing the mold. The fluid rheology is the same as equation (4-5). Such an approach was used in many simulations of squeeze flow [14,18].

The Paraview software visualizes the result of OpenFOAM simulation. The blue square represents the fluid and red regions represent bundles in different positions in Figure 4-10, Figure 4-11 and Figure 4-12. Figure 4-10a and Figure 4-11b show the initial single bundle position and after 1.2 seconds. The bundle moves according to the flow velocity (Figure 4-10c) and deforms a bit in the middle where the velocity is higher. The blue region in Figure 4-10c represents the lower velocity than red region. Two ends of bundle are in the blue regions follow the velocity of blue region and the center of bundle followed the velocity of red region. Therefore, the bundle is deformed in the middle.

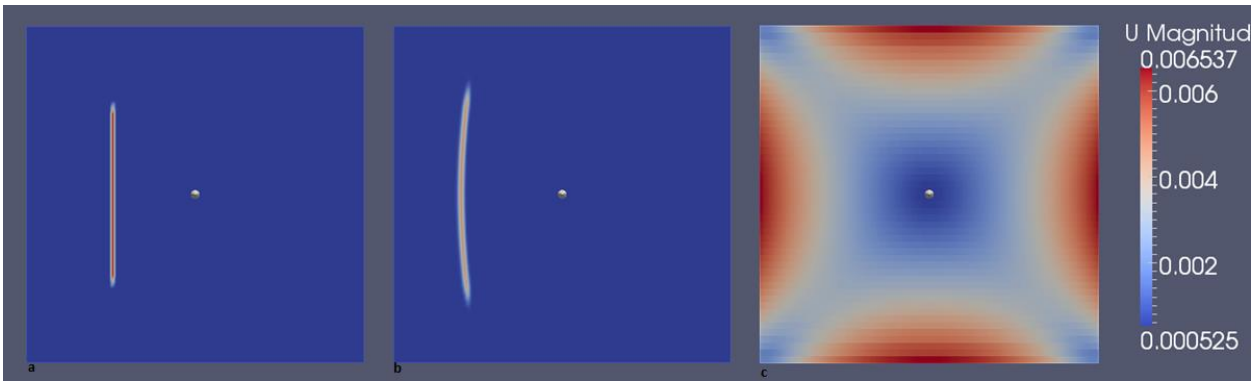

Figure 4-10 Single bundle movement in the mold with 5mm thickness a) initial position b) after 1.2 s c) velocity (m/s) at 1.2s

Another position of interest for the bundle is in diagonal of mold (position 3 or 6 in Figure 4-12). Therefore, the simulation was run for the quarter of mold with symmetry boundary condition on top and right side of the mold to reduce simulation time (Figure 4-11). The bundle stays straight although it re-orients slightly according to the velocity (Figure 4-11c).

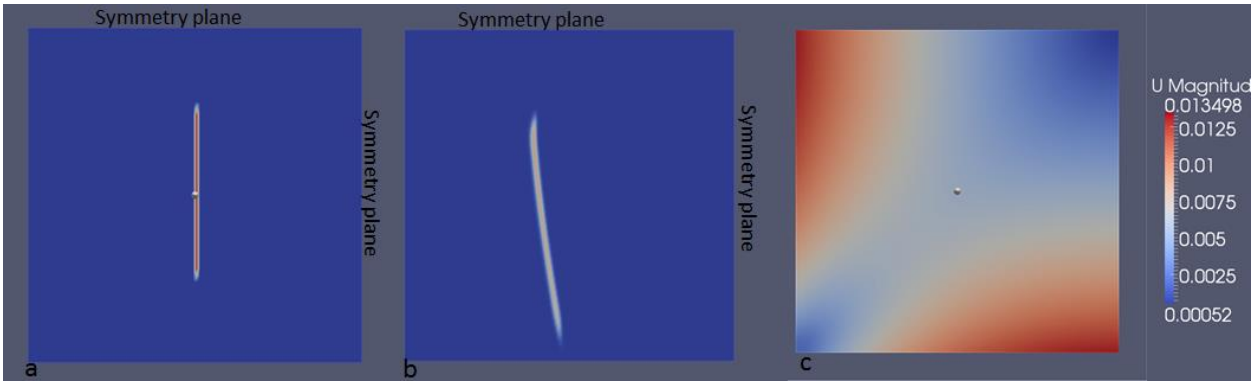

Figure 4-11 Single bundle movement in the mold with 5mm thickness and symmetry boundary condition a) initial position b) after 1.2s c) velocity (m/s) at 1.2 s

In the next simulation, the bundles have the major axis of 1mm and length of 25mm which are able to move during the process. The bundles are modeled with a higher major axis because of limitations in creating the true bundle regions in the system domain. The size of bundles is enlarged in the simulation to be able to track the movement distance and deformation through length in the process and compare the result to the experiment. The bundles placed in the middle, edge, perpendicular, and parallel to the fluid follow depending on the fluid velocity and deform accordingly.

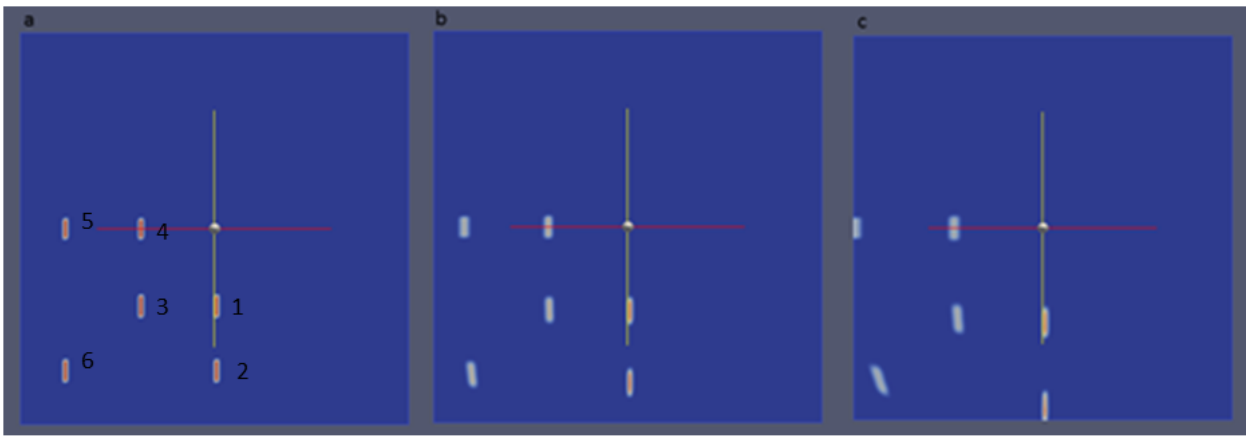

Figure 4-12 a) Initial positions of bundles b) After 0.5s c) After 1.2 s

4.5 Results for simulation of single bundle

Figure 4-12 shows the bundles in their initial positions and after 0.5 and 1.2 seconds. The bundle's movement depends on position and velocity profile. The bundles that are closer to the edges of the mold (positions 2, 5 and 6 in Figure 4-12) moves more quickly than the bundles in other positions. The bundles in the flow direction (positions 1 and 2) are less deformed compared to the bundles perpendicular to the flow. In Paraview, the measurement tool measures the movement distance of bundles. The values of the movement distance are available in Figure 4-14. The bundles perpendicular to the flow (positions 4 and 5) flatten more because of their less resistance to the flow direction. The bundle at position 6 follows the flow field similar to Figure 4-11 and reorients accordingly.

4.6 Experimental validation

The material used for the experiment is 20 percent volume glass fiber bundles chopped in 2.5cm length in polyester paste (Table 4-1). The mold has a square cavity with a dimension of 45.7cm width and length and adjustable thickness. The mold is mounted to a 4000 KN hydraulic press and a controlled mold temperature of 140 °C. The mold surfaces are flat and smooth. The initial charge is centered within the mold and covers 62 percent of the mold area. The initial charge is comprised of two stacks of charges with a thickness of 2.5±0.2mm to the sheet with a thickness of 2.8mm at the speed of 1mm/s. In another experiment, the initial charge is comprised of four stacks of charges covering 30 percent of the mold area. The exact filling time is not available for this process because the mold is kept closed to cure completely and enhance the quality of the sheet surface.

To experimentally visualize the movement of bundles, the glass bundles are colored using red fluorescent dye (Tracer Products TP34000601 UV Fluorescent Leak Detection Dye Supplied by Tracerline). The red bundles are added when the paste from the doctor boxes is about to cover the just chopped glass bundles on the bottom layer of the paste on the carrier film. It is not possible to stop the production line and put bundles exactly in the positions of interest. The colored and uncolored bundles are added randomly at the same time and the red bundles present the majority of bundles. The red individual bundles are found at parallel, perpendicular and diagonal to the flow directions in charge and sheet (as shown in Figure 4-13). The marked grid lines on the surface of the charge defined the relative locations of the bundles [19].

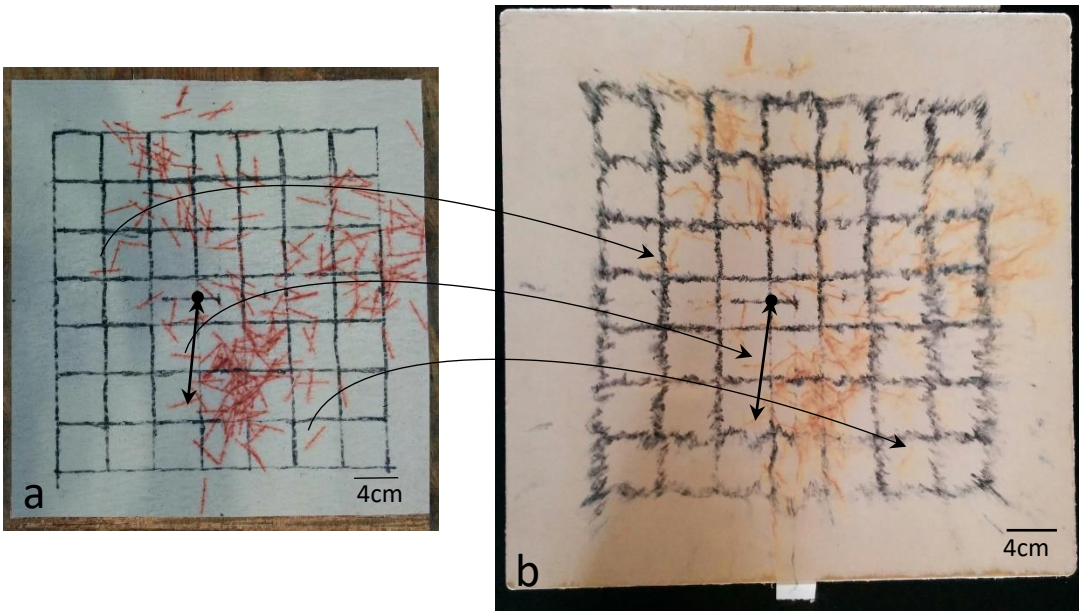

Figure 4-13 Bundle positions a) before compression b) after compression for 62percent mold coverage
Measured distance (↔) reference point (•)

Figure 4-13 shows the bundles at different positions on the charge before compression and on the sheet after compression. The figure confirms the fact that red bundles qualitatively did not rotate or orient significantly differently from their initial distribution. They also keep their shape and translate with the fluid. To calculate the movement distance, ImageJ software is used to measure the distance between the center of the length of a bundle and the reference point for the same bundle in the charge and sheet as shown in Figure 4-13. The reference point is located at the center

of the plane of charge and sheet as shown with dot symbol in Figure 4-13. The movement distance is the difference between these two values.

Figure 4-14 compares the movement distance of bundles at different positions from the OpenFOAM simulation and experiment. The results from the experiment and simulation are in agreement in terms of value and trend. The OpenFOAM simulation over calculates the movement distances. As shown in Figure 4-12, bundles located closer to the edge move more quickly because of less flow resistance ahead of them. Also, bundles closer to the center of mold move more slowly.

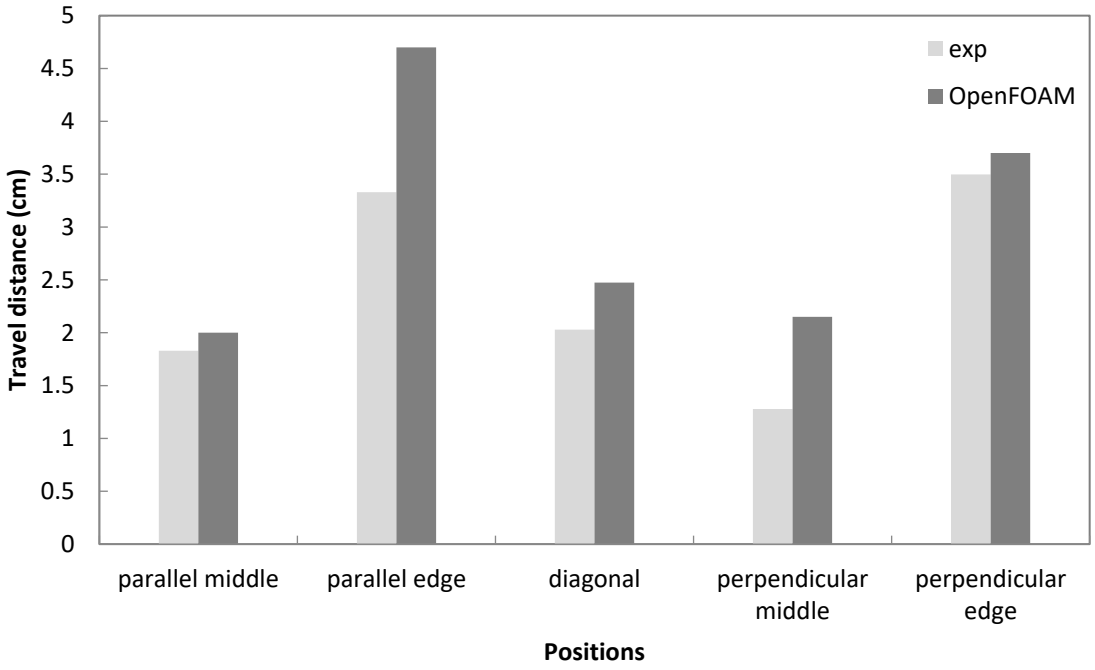

Figure 4-14 Travel distance of bundles at different locations (cm)

4.7 Flow patterns in the sheet cross section

Charges with different colors are used to visualize the flow pattern during the filling process in the mold. A fluorescent dye (Tracer Products TP34000601 UV Fluorescent Leak Detection Dye Supplied by Tracerline) is added to the paste to color the charges. The stack of charges cover 62 percent initial mold coverage and is placed at the center of the mold. Two charges are stacked for compression: one with a fluorescent dye and the other without. In another experiment, four charges are stacked, two with a fluorescent dye and the other two without dye, with 30 percent initial mold area coverage. After compression molding, the sheet is cut and the cross sections are polished

using different grades of sandpaper (SIC 800 to 4000). The difference between colors through the cross section is only visible when the area of interest is exposed to fluorescent light.

A Canon EOS digital camera on a tripod captures the images from the distance of 30 cm in front of the sample. There is a black piece of paper in the background and the ultra violet light (Lighting EVER 21 LED UV LED Flashlight, Blacklight, 395nm Utlra Violet) exposed the sheet cross section in a dark environment to cause the fluorescent region to become visible. The details of capturing images are available in appendix B [20].

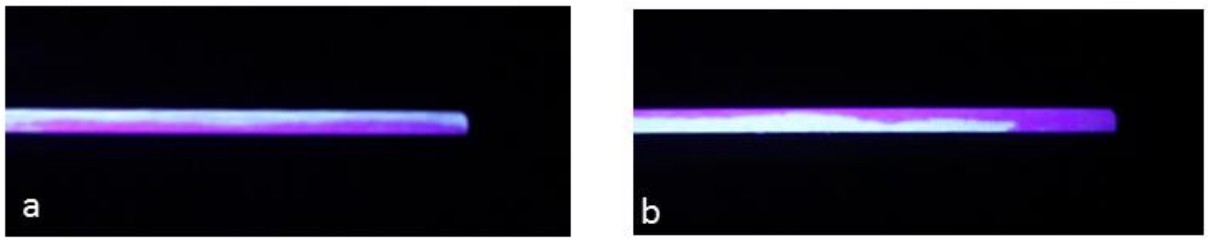

Figure 4-15 Cross section of the sheet a) two stacks of charges 62 percent initial mold area b) four stacks of charges 30 percent initial mold area (the flow is from the center of mold (left) to end of cavity (right)

Figure 4-15 shows photos of cross sections cut from the middle line (as shown in Figure 4-3) of plaque for the two cases of 62 and 30 percent initial coverage. The interface of the cross section with the fluorescent ink is visible in both cases. Barone and Caulk [21] reported the extensional flow of SMC with different closing speeds for several numbers of charges. Many studies have confirmed that the flow is predominantly extensional in squeezing the SMC with different closing speeds [12–14]. For the 62 percent coverage, layers extend uniformly to the end of the mold's cavity. When the charge covers 30 percent of the mold, the flow length is longer, extensional flow is dominant and the top fluorescent charges slip over the bottom layer. As the flow length is longer for 30 percent coverage, it takes longer for the fluid to fill the mold and any variation in the local volume of bundles could causes the different relative motion of layers. Also, the bottom plate of the mold is stationary so that the upper layers of charge first are exposed to move than the bottom layers. This is more significant in 30 percent mold area coverage because the initial charge has a higher thickness than 62 percent mold area coverage.

4.8 **Conclusion**

OpenFOAM simulates compression molding by introducing a rheology model for planar random orientation of fiber bundle in SMC. The result of the simulation shows extensional flow in the core

at all positions of the charge during filling for 30 percent and 62 percent of mold coverage. Using charges of SMC with different colors in the experiment and photography of sheet cross sections also confirms the extensional flow 62 percent mold coverage. OpenFOAM is also used to simulate single bundle movement in the compression process. The movement distance of the fiber bundles at different locations shows that bundles closer to the edges of the flow or mold wall move more quickly than the bundles closer to the center of the mold. The trend and values are in agreement with the experimental calculation of movement distance. The images of colored bundles in the charge and sheet show that the bundles flow along the SMC suspension and do not re-orient and rotate significantly because of fiber bundles networks that are highly in contact.

4.9 References

[1] (www.OpenFOAM.org). The OpenFOAM Foundation n.d.

[2] Versteeg Henk Kaarle MW. An Introduction to Computational Fluid Dynamics: The Finite Volume Method. 1995.

[3] Brackbill JU, Kothe DB, Zemach C. A continuum method for modeling surface tension. Journal of Computational Physics 1992;100:335–54.

[4] Silva-Nieto RJ, Fisher BC, Birley a. W. Predicting mold flow for unsaturated polyester resin sheet molding compounds. Polymer Composites 1980;1:14–23.

[5] Ekedahl E. 6-DOF VOF-solver without Damping in OpenFOAM 2009.

[6] Servais C, Luciani A, Månson J-AE. Fiber–fiber interaction in concentrated suspensions: Dispersed fiber bundles. Journal of Rheology 1999;43:1005.

[7] Toll S. Packing[1] S. Toll, “Packing mechanics of fiber reinforcements,” Polymer Engineering & Science, vol. 38, no. 8, pp. 1337–1350, Aug. 1998. mechanics of fiber reinforcements. Polymer Engineering & Science 1998;38:1337–50.

[8] Lee LJ, Marker LF, Griffith RM. The rheology and mold flow of polyester sheet molding compound. Polymer Composites 1981;2:209–18.

[9] Barone MR, Caulk DA. The effect of deformation and thermoset cure on heat conduction in a chopped-fiber reinforced polyester during compression molding. International Journal of Heat and Mass Transfer 1979;22:1021–32.

[10] Lee C-C, Folgar F, Tucker CL. Simulation of Compression Molding for Fiber-Reinforced Thermosetting Polymers. Journal of Engineering for Industry 1984;106:114.

[11] Lee C-C, Tucker CL. Flow and heat transfer in compression mold filling. Journal of Non-Newtonian Fluid Mechanics 1987;24:245–64.

[12] Kotsikos G, Gibson a. G. Investigation of the squeeze flow behaviour of Sheet Moulding Compounds (SMC). Composites Part A: Applied Science and Manufacturing 1998;29:1569–77.

[13] Collister J, Allen A. Sheet molding compound rheology. Compounds Science and Technology 1993.

[14] Gibson a. G, Toll S. Mechanics of the squeeze flow of planar fibre suspensions. Journal of Non-Newtonian Fluid Mechanics 1999;82:1–24.

[15] Servais C, Luciani A, Månson J-AE. Squeeze flow of concentrated long fibre suspensions: experiments and model. Journal of Non-Newtonian Fluid Mechanics 2002;104:165–84.

[16] Kau H, Hagerman EM. Experimental and analytical procedures for flow dynamics of sheet molding compound (SMC) in compression molding. Polymer Composites 1987;8:176–87.

[17] Guiraud O, Orgéas L, Dumont PJJ, Rolland du Roscoat S. Microstructure and deformation micromechanisms of concentrated fiber bundle suspensions: An analysis combining x-ray microtomography and pull-out tests. Journal of Rheology 2012;56:593.

[18] Leider PJ, Bird RB. Squeezing Flow between Parallel Disks. I. Theoretical Analysis. Industrial & Engineering Chemistry Fundamentals 1974;13:336–41.

[19] Corre S Le, Favier D, Dumont P, Orge L. Anisotropic viscous behavior of sheet molding compounds (SMC) during compression molding 2003;19:625–46.

[20] WESTON C. Nature Photography Insider Secrets from the World's Top Digital Photography Professionals. 2008.

[21] Barone MR, Caulk DA. Kinematics of flow in sheet molding compounds. Polymer Composites 1985;6:105–9.

5 Simulation of flow through the thickness direction in DSMC

This chapter was presented at the 2nd Annual ICRC/IRTG Summer Workshop and Symposium on Composite Materials

London, Canada, 2017

5.1 Objective

The combination of flow behavior with heat transfer during compression molding of D-SMC is studied by numerical simulation in the two-dimensional case through the thickness direction. Polyflow (Ansys) is used to solve the equations of motion and energy for two cases: I) two layers of charges with different viscosities, and II) core layer with paste/glass fiber behavior between two thin layers of paste adjacent to the mold walls. Polyflow is capable of solving the problems in polymer processing in two dimensional and for multiple phases.

In D-SMC, there is a viscosity variation through thickness because of temperature gradient and glass bundle volume fraction variation. The aim of simulation for the case I is to study the effect of viscosity variation on mold filling.

The charge is placed between two hot plates of mold which are then closed to squeeze the charge and filled the mold. The layers of charge close to the hot mold plates act as lubricant for layers of charge in center. Because of greater resistance of charge in the center to flow, the hotter lubrication layer may flow preferentially before core layers of charge. The simulation is run for case II to study the preferential flow.

The objective of this chapter is to examine the preferential flow of thin, paste rich layers close to the mold walls, and the interface evolution between the layers of charges. Images of cross sections from experimental samples are used to validate the simulation analysis.

5.2 Modelling

5.2.1 Mathematical modeling

Compression molding of a Non-Newtonian fluid between two plates is examined through a model and finite element implementation in a commercial CFD package (Ansys, Polyflow). The parameters $\boldsymbol{T}, u, p$ and T represent the total stress tensor, velocity, pressure, and temperature respectively. The momentum and continuity equations are given by

$$-\nabla P + \nabla . \boldsymbol{T} = \rho \frac{Du}{Dt} \qquad (5.2.15\text{-}1)$$

$$\nabla . u = 0 \qquad (5\text{-}2)$$

Where ρ is density. Inertia effects are taken into account because the stability of time marching scheme is improved [1].

The energy equation is given by

$$\rho C_p \frac{DT}{Dt} = k\nabla^2 T + T:\boldsymbol{T} \tag{5-3}$$

Where C_p and k are the specific heat and the thermal conductivity, respectively. Both parameters are assumed to be constant and the values are used from literature from the similar system of material and equal to 1000 J/kg.K and 0.53 W/m.K [2, 3].

5.2.2 Constitutive equation

A constitutive equation is needed in equation 5-1. Lee et. al showed that the viscosity of SMC paste follows the Carreau model [4], given by

$$\boldsymbol{T} = 2\left[\eta_\infty + (\eta_0 - \eta_\infty)(1 + \lambda^2\dot{\gamma}^2)^{\frac{n-1}{2}}\right] D \tag{5-4}$$

Where D is the rate of strain tensor with the shear rate of ($\dot{\gamma}$). The parameter η_0 and η_∞ are the zero shear viscosity and viscosity at infinite shear rate, and λ and n are time constant and power law index, respectively [5].

The sample of SMC paste is located between the parallel plates of rheometer (Rheometrics mode RDS-II) in a rotational mode. The shear rate varies between 0.01 to 100 (1/s) at 20 ℃, to measure the parameters of the Carreau model. The diameter of the plate is 25mm and gap was set to 0.75mm. The samples are a paste and a paste that includes 20 percent by volume in-plane random glass fiber (GF) bundle.

Figure 5-1 and Figure 5-2 show the experimental viscosities and model predictions for paste and paste including 20 percent by volume GF bundle. The parameters of the Carreau model are obtained by minimizing the sum of squares and summarized in Table 5-1. The presence of GF bundle increases the viscosity by an order of magnitude.

5.2.3 Boundary condition

The temperature dependence of viscosity is modeled by the Arrhenius form given by:

$$\eta = \eta_0 exp\left[E_a(\frac{1}{\theta^*} - \frac{1}{\theta_\alpha^*})\right] \tag{5-5}$$

where subscript * represents the absolute temperature scale in Kelvin degree. In equation 5-55-5, η_0 is the viscosity at reference temperature θ_α^* , while E_a is the activation energy. The activation

energy is used from the work by Dumont et al. [6] for the similar system of paste and the value is 4500 K.

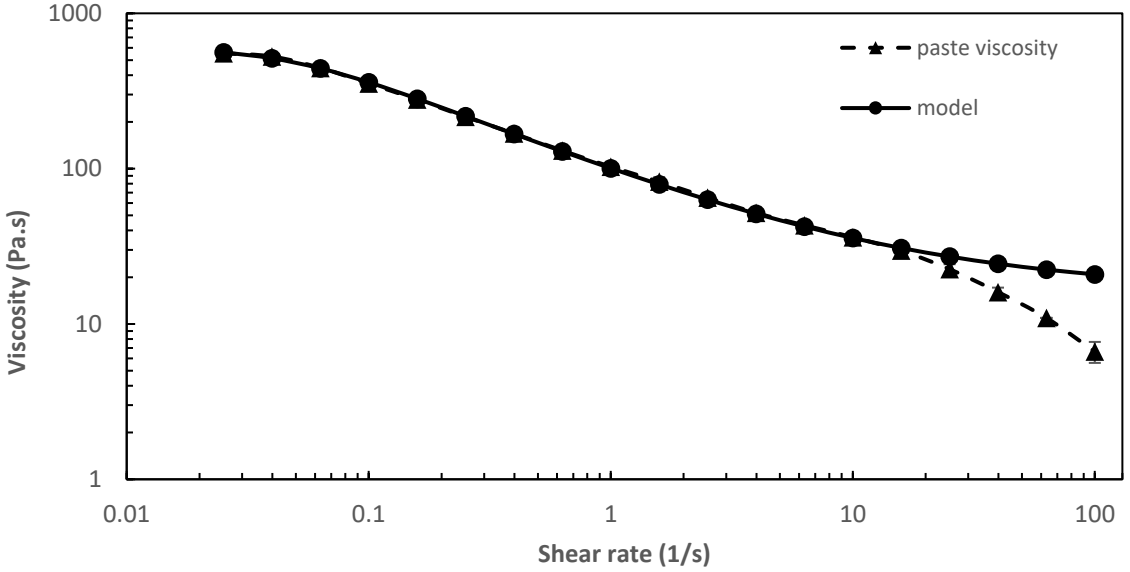

Figure 5-1 Shear viscosity of paste as a function of shear rate

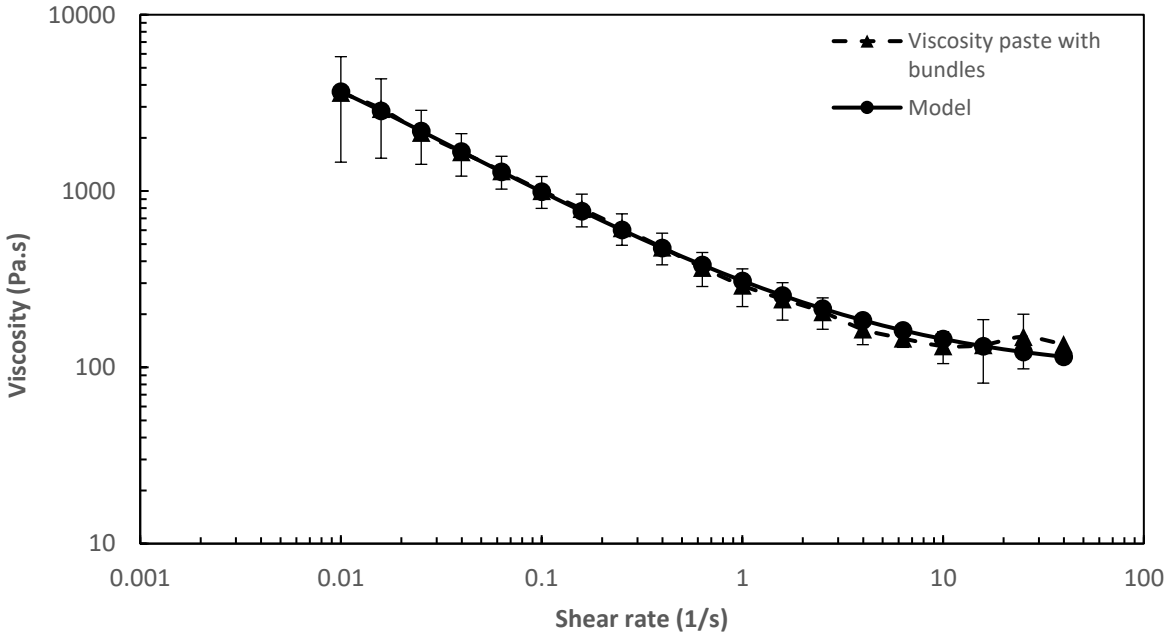

Figure 5-2 Shear viscosity of paste including 20 percent GF as a function of shear rate

Table 5-1 Parameters of viscosity model

	η_∞ (pa.s)	η_0 (pa.s)	λ (s)	n	ρ (kg/m^3)
Paste	16.4	606	21	0.362	1330
Paste/20GF	92.5	6832	261	0.38	1850

5.2.4 Computational domain and discretization

The finite element mesh generated by Ansys Meshing is displayed in
Figure 5-3. The finite element mesh is defined for both fluid and mold. In the simulation involving contact, the deformations undergone by the fluid is significant.

In this study, the geometric model is axisymmetric with respect to the center line. A mesh for two charges consists of 4500 elements. Note that the mesh is finer near the mold surfaces and interface where higher gradients of velocity and temperature are expected. A mesh for core charge with a paste layer on top and bottom consisting of 43000 elements because more elements are needed to verify the fluid on the thin layer.

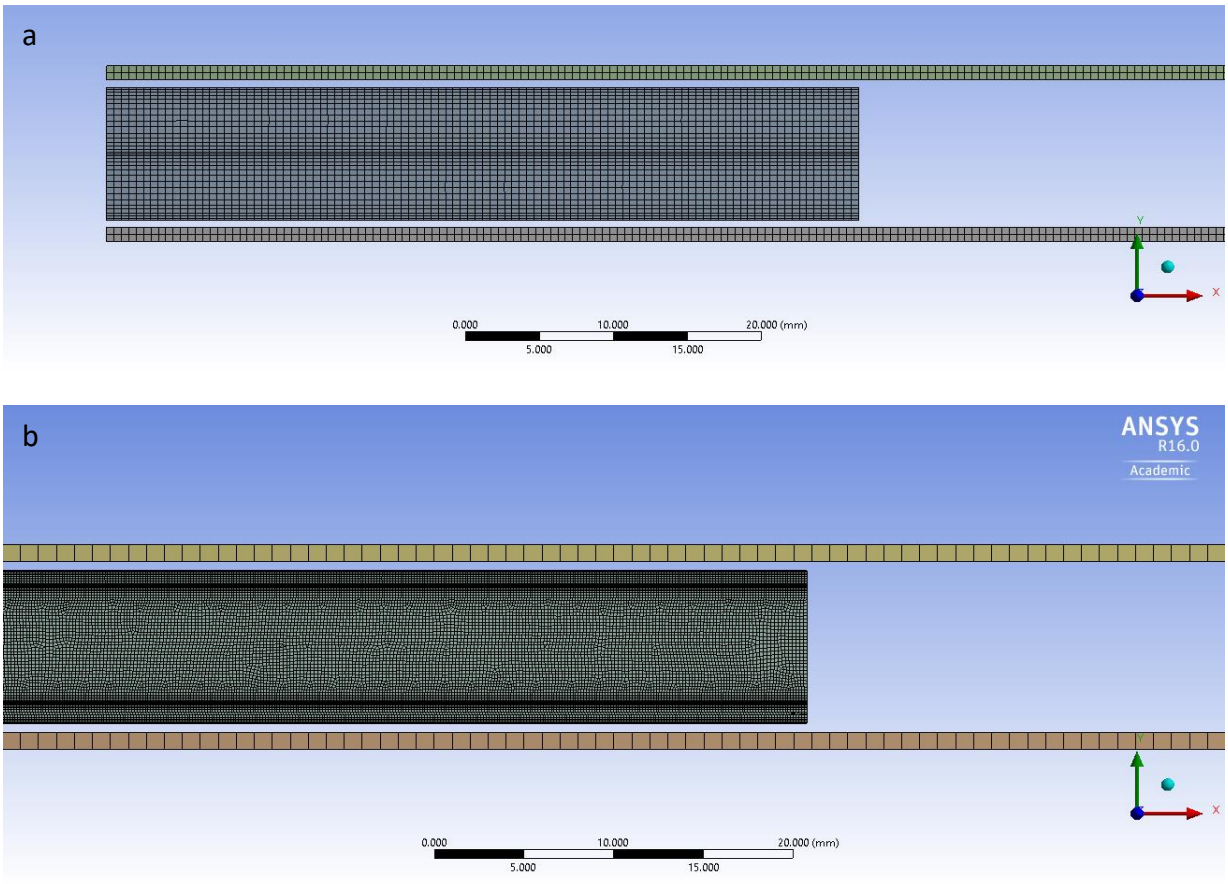

Figure 5-3 Finite element mesh of computational domain a) two charges with different viscosities b) core charge with two layers of paste on top and bottom

5.2.5 Boundary condition

The symmetry condition is applied on the left boundary. The free surface is applied for flow front. Polyflow calculates the free surface by imposing that, at the free surface, the velocity normal to the surface, whose location has been solved for, is zero ($u.n = 0$) and the stress normal to the fluid surface is also zero. The free surface condition states that no mass crosses the free surface [7–9]. When the upper plate of mold moves downward, it enters contact with the fluid. The treatment of fluid/plate contact is handled by penalty formulation, e. g. similar to blow molding problems [10]. At the contact of the fluid with mold plates, the fluid acquires the plate velocity, i.e. zero velocity at the lower plate and assigned velocity at the upper plate. Barone and Caulk [11] showed the slip occurs at the mold surfaces. Therefore, the slip condition is set at upper and lower boundaries. At the fluid-mold contact, the contact force, f_c, is given by

$$f_c = k_p(u - u_{plate}) \quad (5\text{-}6)$$

Where, u_{plate} is the velocity vector of the plate. A zero value is chosen for the penalty coeffiecient, k_p, so that the fluid velocity dominates the plate velocity at contact and guarantees the slip at the plates [8].

The initial temperature is 60 ℃ for the paste and a temperature of 140 ℃ at the mold plates.

5.2.6 Finite element algorithm

The finite element CFD software package Ansys Polyflow 16.0 is used to perform numerical simulations [8]. The system of equations (5.2.15-1) to (5-5) are characterized by non-linearities from the selected constitutive equations and deforming domains. In the interpolation scheme of the finite element discretization, the quadratic elements for velocities and temperature and linear elements for pressure are used. Newton iteration is used to solve the non linear discretized equations.

5.3 Experimental procedure

5.3.1 Material and process

Sheet molding compound includes a wide range of chopped fiber bundle reinforced thermosetting compounds used in compression molding. The charges of SMC used in this work consist of 20 percent by volume of GF bundles. The bundles have a nominal length of 25mm and are distributed randomly in the plane of charge. The charges have a thickness of 2.5±0.2mm.

The mold has a square cavity with dimensions of 45.7cm width and length and adjustable thickness. The mold is mounted in a 4000 KN hydraulic press and controlled mold temperature of 140 °C. The mold surfaces are flat and smooth. The initial charge covers 62 percent of the mold area and centers in the mold. In the first set of experiments, two stacks of charges are pressed to a final thickness of 2.8mm (the mold cavity thickness) at the mold closing speed of 1mm/s. In a second set of experiments, four stacks of charges initially covering 30 percent of the mold area are compressed. There is no measurement tool to indicate the end of mold fill.

Charges with different colors are used to visualize the flow pattern during the filling process. Fluorescent dye (Tracer Products TP34000601 UV Fluorescent Leak Detection Dye Supplied by

Tracerline) is added to the paste to change the color of charges. The stacks of charges initially cover 62 percent of the mold area and sit at the center of the mold. The mold presses two stacks of charges: one with the fluorescent dye and the other without dye. For 30 percent initial mold area coverage, the mold presses four stacks of charges, alternating colored and non-colored charges.As an alternative scenario, two stacks of colored charges on two stacks of non-colored charges are also used.

In another experiment four stacks of charge with a 30 percent initial mold area coverage are formed and a 10cm square hole is cut in the centre, with a colored charge inserted that exactly fill the hole.

After compression molding, the sheet is cut to expose the mold thickness plane and the cross sections are polished using different grades of sandpaper (SIC 800 to 4000). The difference between the colors through the cross section is only visible when the area of interest is exposed to ultra violet light (Lighting EVER 21 LED UV LED Flashlight, Blacklight, 395nm Utlra Violet).

5.3.2 Simulation result

Barone and Caulk [11] investigated the flow in compression molding by using the black and white layers of SMC (polyester/30 weight percent of GF) and inserting the white charge into the hole designed in black charge (segmented charge). Their images of their experiments showed the layers of charge extended uniformly with no relative motion in layers. Also, layers close to the mold surface moved faster than the core layers. In segmented charge, the boundary between the white and black confirmed the uniform slip at mold surfaces. Similarly, Odengberger et al. [12] visualized the flow front of SMC and showed that the upper and lower layers close to mold plates flow prior to other layers.

Figure 5-4 and Figure 5-5 show the simulation for the core charge, which 20 volume percent of glass bundles, with two layers of paste on the top and bottom for isothermal and non-isothermal cases at different time steps. The core charge has the viscosity of paste/GF and two layers have the viscosity of the paste (see Table 5-1). The low viscosity paste acts as a lubricant for the core charge, which undergoes extensional flow. In the non-isothermal simulation shown in Figure 5-5, the temperature effect in the thin layer of paste adjacent to the mold plates causes the affected layers move faster than the isothermal case. This effect is more significant at a later time (5.3s).

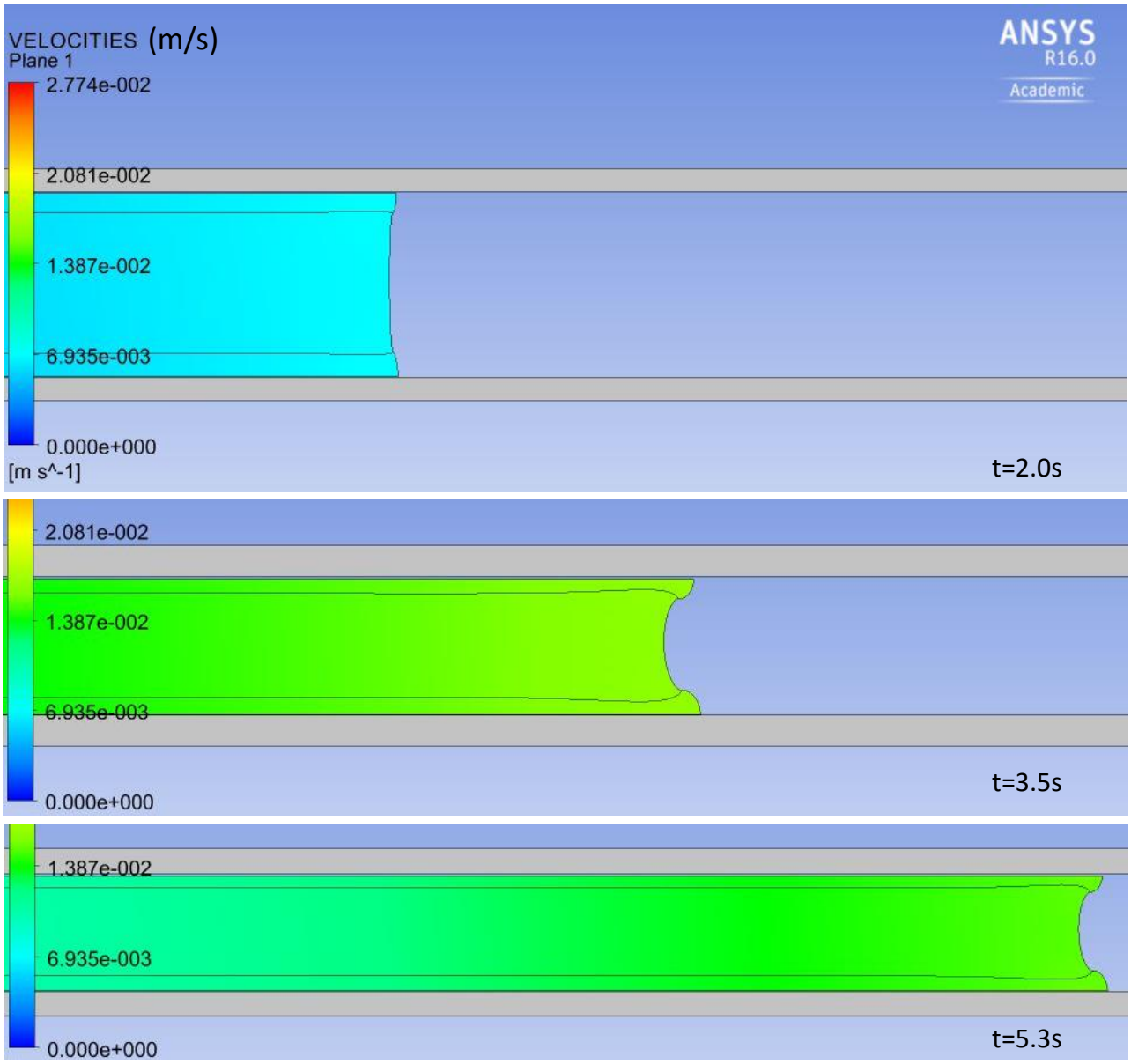

Figure 5-4 Isothermal flow over time for core charge with two layers of paste on top and bottom

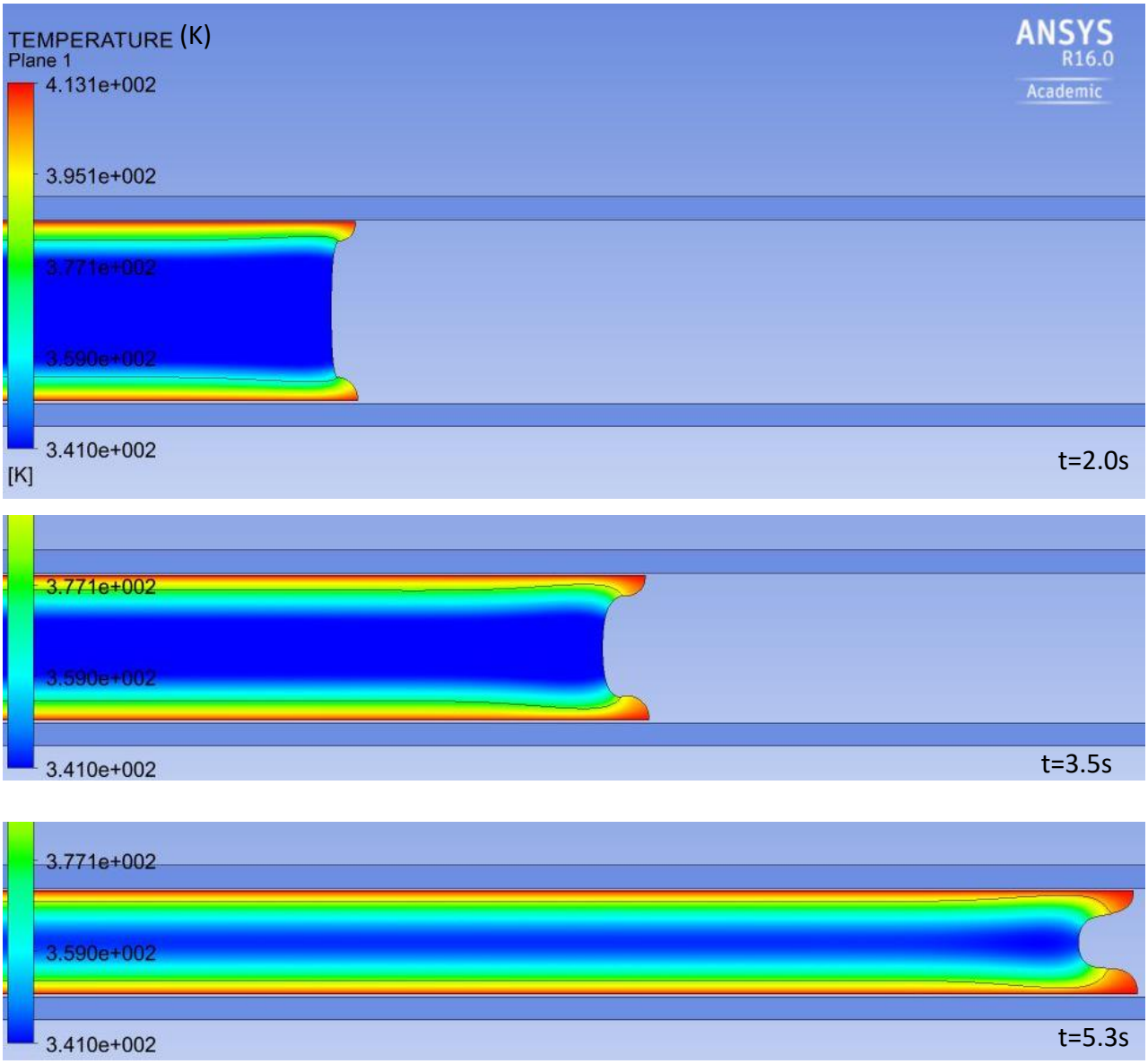

Figure 5-5 Flow and temperature development over time for core charge with two layers of layer of paste on top and bottom

Lee et al. [13] studied compression molding for two charges with different Newtonian fluids. The analysis showed the higher the ratio of maximum viscosity to minimum viscosity, the more significant the preferential flow is in the lower viscosity region.

There is a variation of viscosity through thickness due to temperature and glass bundle. To study the effect of viscosity on flow, two charges with different viscosity models are considered. The configuration includes the top charge with paste viscosity model on the bottom charge with paste/GF viscosity model. Figure 5-6 and Figure 5-7 show the simulation results for two stacked

charges in isothermal and non-isothermal cases at different time steps. The top charge moves ahead of the bottom charge and the interface is mainly affected in the regions close to the flow front. In the non-isothermal case, the temperature affects the upper and lower layers close to the mold plate and lubricate the movement of adjacent layers. The movement of the upper charge is more significant at later stages (5.3s). The viscosity variation through thickness causes an uneven interface especially in the regions close to the flow front. Moreover, in non-isothermal simulation (Figure 5-8), the temperature effect causes reduced viscosity and preferential flow near the mold wall.

The simulation starts when the temperature of the charge is initially 60°C and then squeezed between the hot plates of the mold. Simulation results in Figure 5-6 and Figure 5-7 show that the mold filling could be completed before the heat conduction causes the charge to become isothermal.

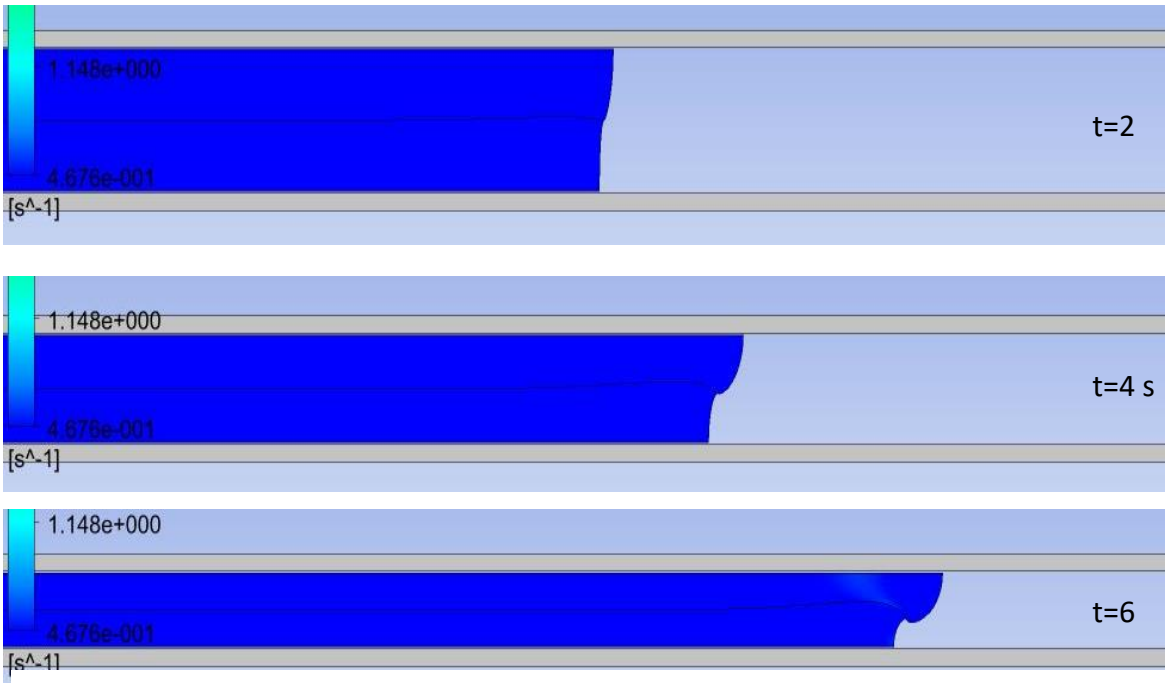

Figure 5-6 Isothermal flow development for two layers of charge with paste layer and paste with GF layer

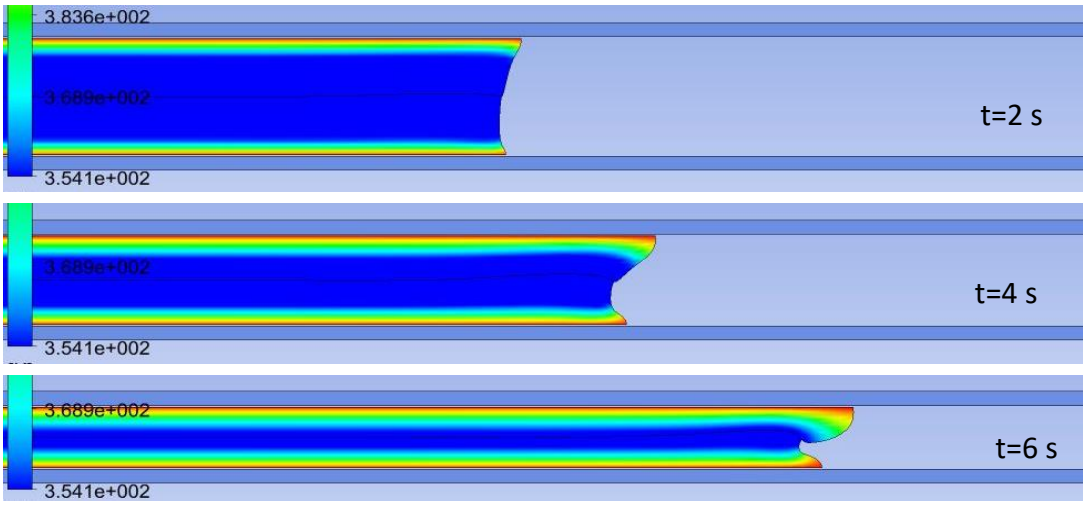

Figure 5-7 Temperature and flow development for two layers of charges with paste layer and paste with GF layer

5.3.3 Experimental result

The colored and non-colored charges are used to form a sheet and study the flow behavior. The flow pattern is examined for 30 percent initial mold area coverage in segmented and layered form and 62 percent mold area coverage in layered form.

Figure 5-8 shows the cross section of the sheet from 30 percent initial mold area coverage with a colored charge in the middle of a non-colored charge (segmented). In this arrangement, the preferential flow at the mold plates is observed otherwise the non-colored trace should be visible at mold plates. The simulation result shown in Figure 5-4 and Figure 5-5 also confirms the preferential flow is due to the reduced viscosity which can be result of paste rich layer and high temperature at this region. Moreover, in Figure 5-8 image 3 and 4, the upper two charges move ahead of the lower charges.

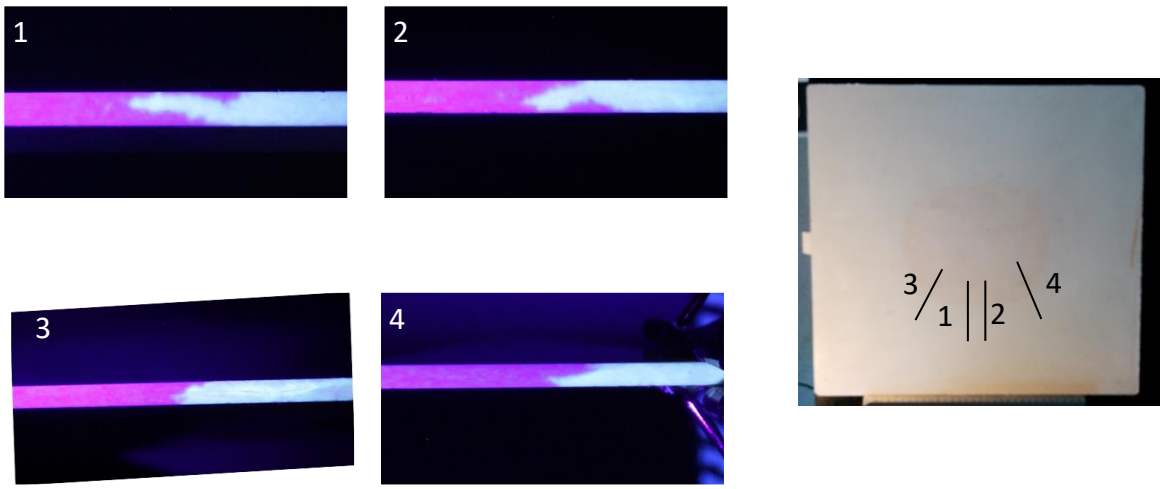

Figure 5-8 8 Images of cross section from 30 percent mold area coverage and segmented charge at different positions (1, 2, 3, 4 are images at the positions of right-hand side sheet)

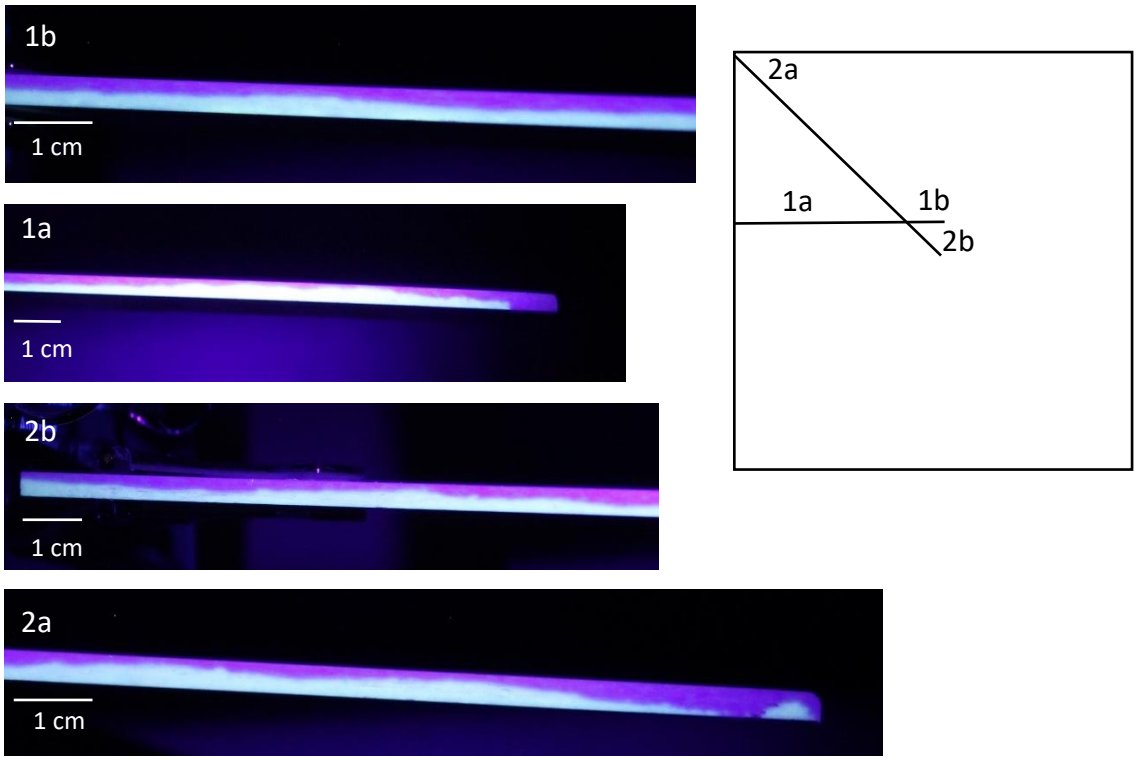

Figure 5-9 Images of 30 percent initial mold area coverage and layered with two layers of colored charges on top of two layers of non-colored charges at different positions (1a, 1b, 2a, 2b are images at the positions of right-hand side sheet)

The images of cross sections of the sheet from two colored charges on two non-colored charges for 30 percent mold area coverage are shown in Figure 5-9. The interface between colored and non-colored sections are even in 1b and 2b where they are close to the center of mold and less exposed to the flow. However, the uneven interface is more significant in the sections close to the

end of the mold cavity (1a and 2a). The upper charges reach the end of the mold cavity ahead of lower charges. The simulation result shown in Figure 5-6 and Figure 5-7 confirm that the interface is more affected while two charges are filling the mold at regions close to flow front. Also, dependency of viscosity models on temperature (non-isothermal simulation shown in Figure 5-7) intensifies the unevenness of interface and upper charge tends to move ahead of bottom charge like experimental images (Figure 5-9 1b).

Figure 5-10 shows the cross sections of four colored and non-colored charges alternatively placed on each other. Figure 5-10 1a shows the center of sheet cross section including four charges. In this section, all charges are visible due to less flow effect. In Figure 5-10 1b, all charges are not visible and charge thickness varies during filling process. At sections close to the end of mold cavity as shown in Figure 5-10 1c only two charges are visible and flow to the end of cavity. Uneven interfaces are significant at all sections of images. Also, the probable slip of charges on each other is more likely in the 30 percent mold area coverage as shown in Figure 5-10and Figure 5-8 image 4 because of a high number of charges as well as long flow length.

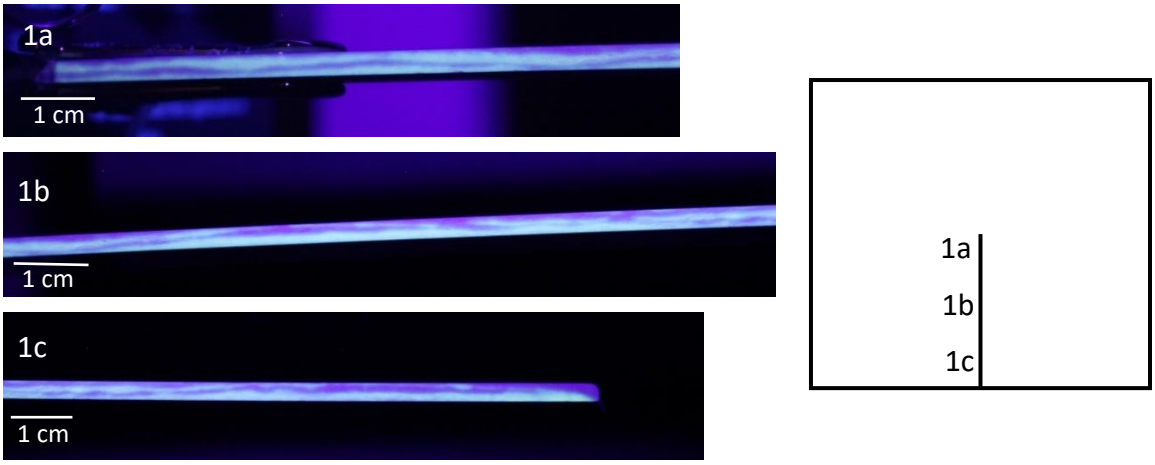

Figure 5-10 Images of 30 percent initial mold area coverage and layered with one layer of colored charge on top of one charge of non-colored charge (4 charges in total) at different positions (1a, 1b, 1c are images at the positions of right-hand side sheet)

Figure 5-11 shows the cross section of the sheet from two colored and non-colored charges at two different positions for 62 percent mold area coverage. At both positions, the interface is even. Both charges reached the edge of the mold cavity at the same time.

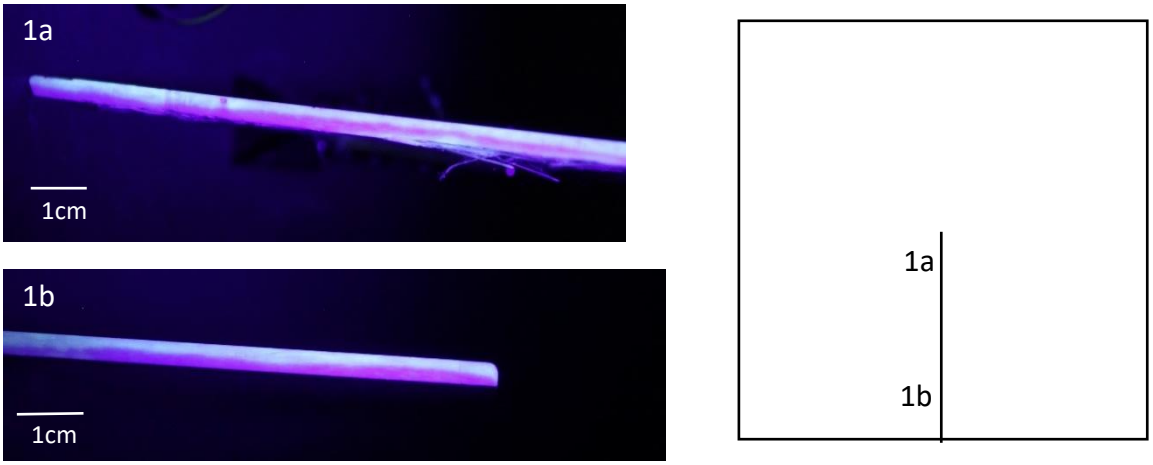

Figure 5-11 Images of 62 percent initial mold area coverage and layered with one non-colored charge on top of one colored charge at different positions

Figure 5-12 shows the distribution of fiber bundles in the cross section of charge. There are regions close to the upper or lower surface of charge where there are no fiber bundles. The thickness of the layers with no observable fiber bundles is estimated as 0.28±0.1mm.

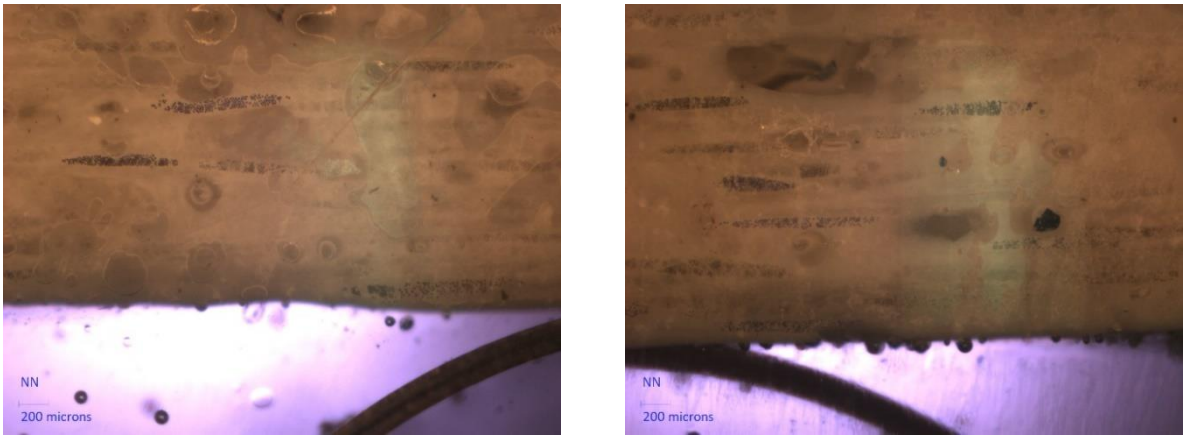

Figure 5-12 Microscopy of cross section of charge close to the upper and lower surface

5.4 Conclusion

The simulation result (Figure 5-4 and Figure 5-5) and experimental image (Figure 5-8) show the preferential flow of the layers close to the mold plates due to the lubricating effect of the paste rich layer and reduced viscosity. The layers close to the hot mold plates undergo greater deformation and act as a lubricant for the core charge.

The microscopy images of the cross section at the area close the surface of charge (Figure 5-12) confirms that some areas close to the surface consist of paste rich layer, which is less resistant to flow especially when heated. This layer is responsible for the preferential flow and facilitates the extension of the core charge.

In experimental images, uneven interfaces in 30 percent initial mold area coverage (Figure 5-9 and Figure 5-10) are more evident compared to 62 percent initial mold area coverage (Figure 5-11), which is the effect of long flow length in the former. Simulation result are also shows an uneven interface especially when the effect of temperature is included in the simulation (Figure 5-6 and Figure 5-7).

5.5 References

[1] Lee SJ, Denn MM, Crochet MJ, Metzner AB, Riggins GJ. Compressive flow between parallel disks: II. oscillatory behavior of viscoelastic materials under a constant load. Journal of Non-Newtonian Fluid Mechanics 1984;14:301–25.

[2] Barone MR, Caulk DA. The effect of deformation and thermoset cure on heat conduction in a chopped-fiber reinforced polyester during compression molding. International Journal of Heat and Mass Transfer 1979;22:1021–32.

[3] Lee C-C, Tucker CL. Flow and heat transfer in compression mold filling. Journal of Non-Newtonian Fluid Mechanics 1987;24:245–64.

[4] Lee LJ, Marker LF, Griffith RM. The rheology and mold flow of polyester sheet molding compound. Polymer Composites 1981;2:209–18.

[5] Bird RB, Armstrong RC, Hassager O. Dynamics of polymeric liquids, Vol. 1. Fluid mechanics. John Wiley & Sons, Inc, New York, NY ; 1987.

[6] Dumont P, Orgéas L, Favier D, Pizette P, Venet C. Compression moulding of SMC: In situ experiments, modelling and simulation. Composites Part A: Applied Science and Manufacturing 2007;38:353–68.

[7] Mavridis H, Hrymak AN, Vlachopoulos J. Transient free-surface flows in injection mold filling. AIChE Journal 1988;34:403–10.

[8] POLYFLOW User's Manual 2017;16.0.

[9] Ferziger JH, Perić M (Milovan). Computational methods for fluid dynamics. Springer; 1996.

[10] Debbaut B, Homerin O, Jivraj N. A comparison between experiments and predictions for the blow molding of an industrial part. Polymer Engineering & Science 1999;39:1812–22.

[11] Barone MR, Caulk DA. Kinematics of flow in sheet molding compounds. Polymer Composites 1985;6:105–9.

[12] Odenberger PT, Andersson HM, Lundström TS. Experimental flow-front visualisation in compression moulding of SMC. Composites Part A: Applied Science and Manufacturing 2004;35:1125–34.

[13] Lee SJ, Denn MM, Crochet MJ, Metzner AB. Compressive flow between parallel disks: I. Newtonian fluid with a transverse viscosity gradient. Journal of Non-Newtonian Fluid Mechanics 1982;10:3–30.

[14] Barone MR, Caulk DA. A Model for the Flow of a Chopped Fiber Reinforced Polymer Compound in Compression Molding. Journal of Applied Mechanics 1986;53:361.

6 Conclusion and recommendations

6.1 **Conclusions**

The work presented in this thesis contributes to the fundamental aspects involved in D-SMC processes such as maturation zone and compression molding. Different computational fluid dynamic packages have been used so that the physical process of interest become dominant and can be investigated. The contributions arising from this research are summarized below.

- The permeability of bundle calculated from simulation compared with the available model. The disagreement was related to the high ratio of major axis to minor axis and arrangement of fibers in the bundle.
- Simulation of flow in maturation zone revealed that the impregnation is mainly because of short distance movement of an interlocking chain of transforming belt. The opening and closing chains local knead of the paste and encourage impregnation.
- The microstructure of D-SMC parts was studied before and after processing. The bundles kept their cohesion in the maturation zone and during compression. The microscopy analysis of the charge bundles showed that they remained relatively straight and formed a network of highly connected bundles.
- Regardless of the position and initial charge mold area coverage, the bundles flattened in the compression molding process. The bundles flattened up to 37 percent of the initial width in the corner position of 30 percent initial mold area coverage.
- The measured deflection of bundles was not significant in the compression molding process. The length measurement confirms that bundles did not break during the process.
- Moldflow simulation predicted the resulting fiber tow orientation using the RSC model. Measured values of orientation from micro CT analysis confirmed final random orientation for 62 percent initial mold area coverage. The higher values of the first component of orientation tensor in 30 percent initial mold area coverage compared to 62 percent initial mold area coverage confirms the significant effect of flow length on bundle orientation. The high volume fraction of long bundles along with short flow lengths impeded bundle

orientation far from the random orientation, which is of crucial importance in the design of the complex parts.

- The OpenFOAM simulation of compression molding using a rheology model for planar random orientation of fiber bundle showed extensional flow in the core at all positions during filling for 30 and 62 percent mold area coverage.
- The single bundle movement in the compression molding was simulated in OpenFOAM. The trend and values of the movement distance of bundles at different locations calculated from simulation result and experimentally were in good agreement.
- The images of colored bundles in the charge and sheet showed that bundles flow along the D-SMC suspensions with no signification rotation and re-orientation because of the high contact in the network of bundles.
- The Polyflow simulation of flow and experimental images of cross section of sheet confirmed the preferential flow due to the resin rich layer and a reduced viscosity of paste.
- The images of cross section of sheet showed the more significant uneven interface between charges during filling for 30 percent mold area coverage than 62 percent mold area coverage. The Polyflow simulation result was consistent with the experimental images.

6.2 Recommendations for future work

The result obtained from this research can be extended to the suggestions;

- The degree of impregnation of a fiber bundle has a significant influence on the quality and performance of final product. Three-dimensional simulation of permeability for in-plane random bundles can be simulated computationally and validated by experiment.
- Experimentally measurement of permeability of different fiber bundles such as glass bundles and carbon bundles can give a more precise insight about the impregnation.
- Experimentally measurement of pressure in the different section of maturation zone can help to predict what paste and bundles experience in this zone.
- Development of a code to measure the microstructure properties such as orientation, deflection, bundle width in a highly concentrated network of bundles facilitate the analysis and can be used for statistical analysis of samples especially with complex geometry.
- Sliding plate rheometer due to rectilinear geometry can provide homogenous shear field and may be constructed to give various gaps (0.5-3mm). Study of the rheology of a paste

containing in plane long fiber bundles in sliding plate rheometer provides a better understanding of the microscopic behavior in compression molding. A rheology model can be developed for viscosity as a function of bundle volume fraction and orientation.

- Investigation of thermal behavior of D-SMC such as thickening and cure reaction can be differentiated this process from conventional SMC.
- Investigation and simulation of orientation in highly concentrated in-plane random bundle suspensions considering the physical properties of bundles such as flexibility, the contact point with the neighboring bundle, minor and major axes of bundles can lead to the better prediction of mechanical properties.
- Moldflow simulation of fiber orientation and validation by micro-computed tomography can be done for the industrial complex part.
- Polyflow simulation of compression molding of charges considering the slipping of charges on each other can provide a better understanding of the flow between charges during filling.

Appendix A

Supplementary information

A1 to A8 show the second component of orientation tensor though thickness for the samples at different positions of 30 and 62 initial mold area coverage.

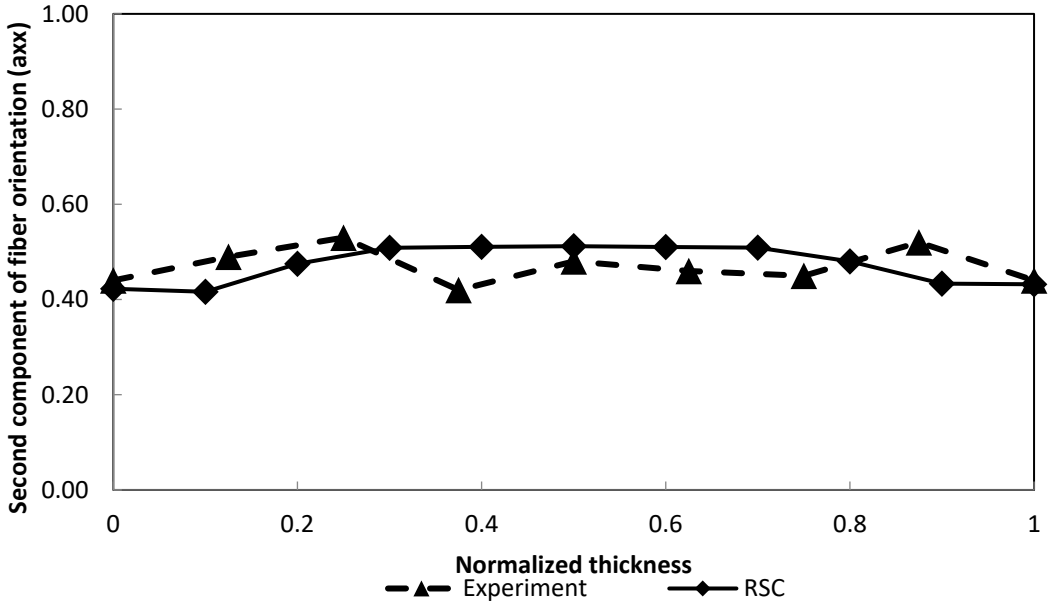

A 1 Second component of fiber orientation for sample M of 62 percent of initial mold area coverage

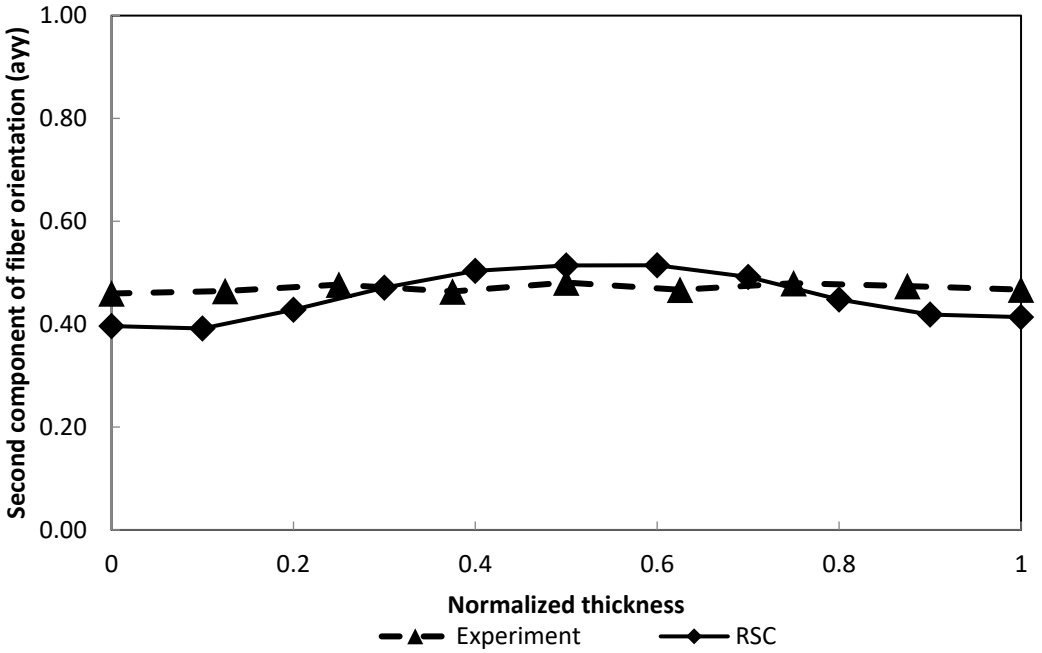

A 2 Second component of fiber orientation for sample M of 30 percent of initial mold area coverage

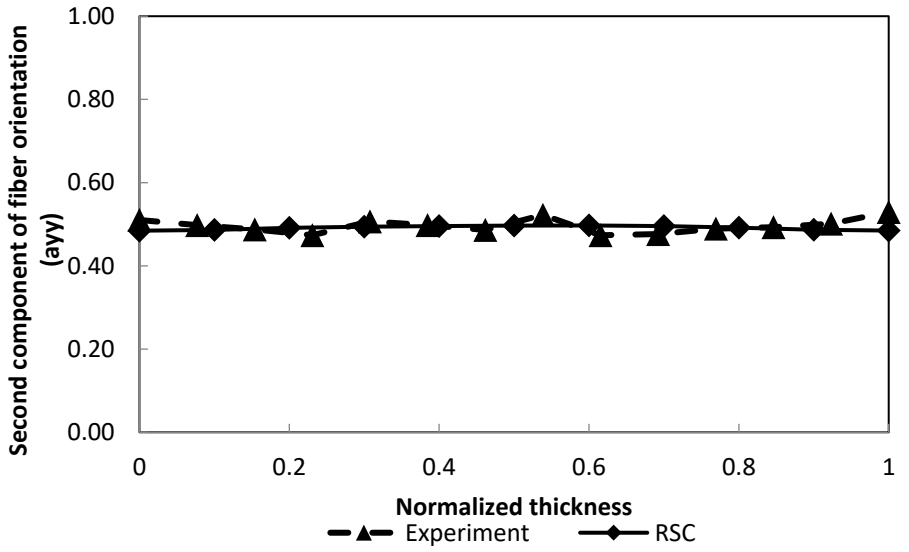

A 3 Second component of fiber orientation for sample D of 62 percent of initial mold area coverage

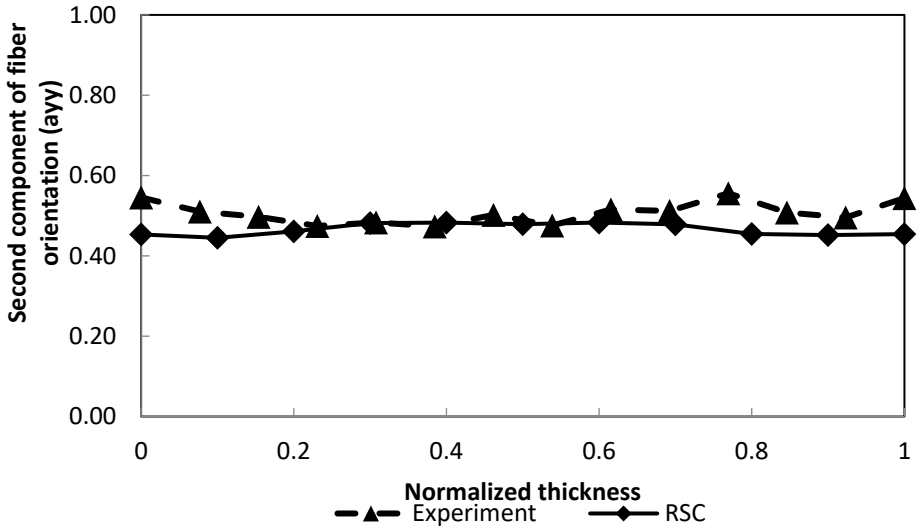

A 4 Second component of fiber orientation for sample D of 30 percent of initial mold area coverage

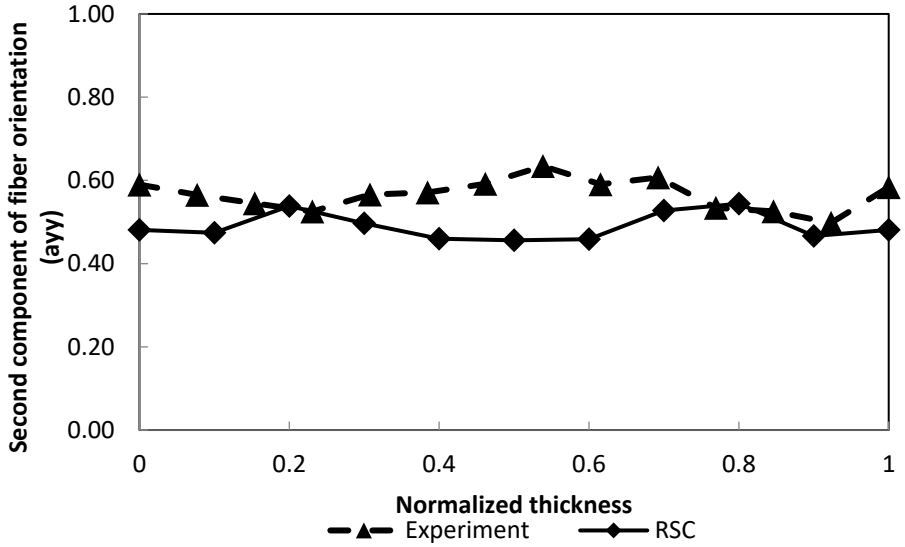

A 5 Second component of fiber orientation for sample E of 62 percent of initial mold area coverage

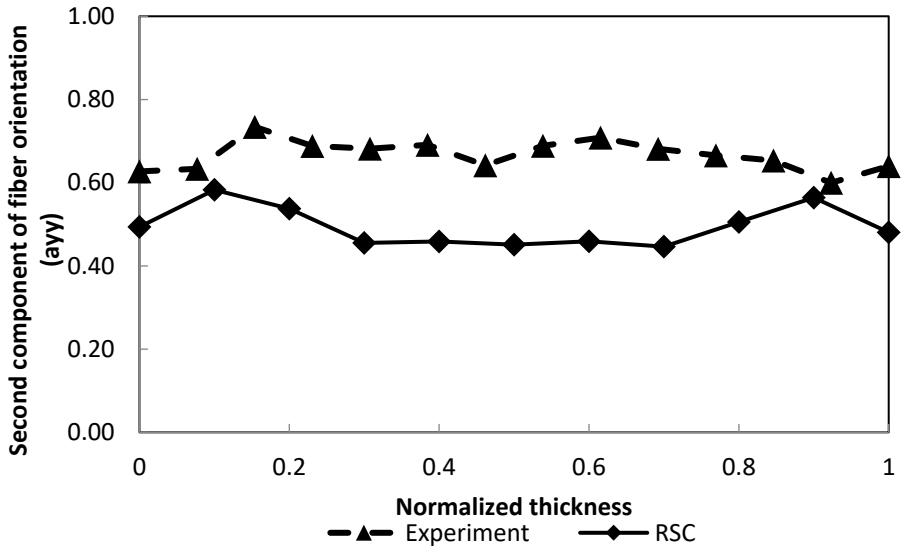

A 6 Second component of fiber orientation for sample E of 30 percent of initial mold area coverage

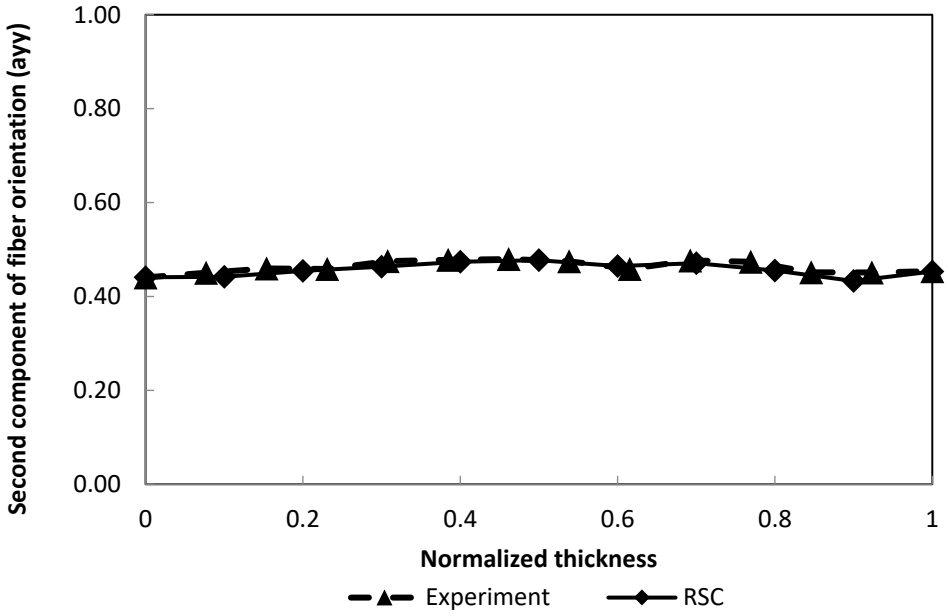

A 7 Second component of fiber orientation for sample C of 62 percent of initial mold area coverage

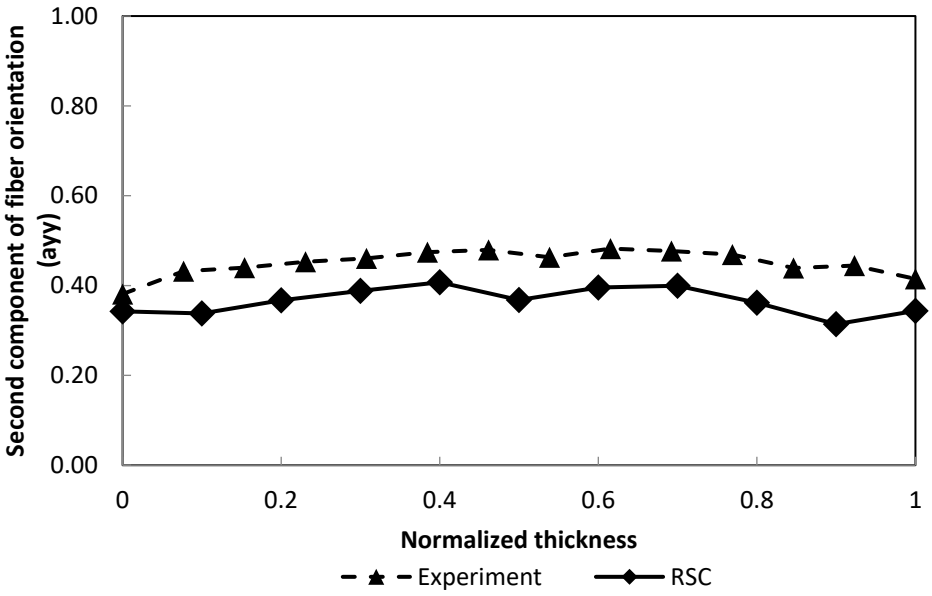

A 8 Second component of fiber orientation for sample C of 30 percent of initial mold area coverage

Appendix B

Details of photography of cross section of sheet

A Canon EOS digital camera on a tripod captured the images from the distance of 30cm in front of the sample. There was a black piece of paper in the background and the fluorescent light exposed the sheet cross section in a dark environment to cause the fluorescent region to become visible. The camera was set to Aperture Value (AV) and ISO of 1600. Then, the camera set a shutter speed so the picture was properly exposed. ISO is the level of sensitivity to available light. The camera is set to low ISO if the scene is less sensitive to light and set to high ISO if the scene is highly sensitive to light. At high ISO, the camera can capture images in low light environments without using a flash. The ISO value of 1600 best fits the image quality for this work. Because the cross section of the sample was surrounded by darkness, the camera guessed the photo was falsely lit. Setting the evaluation value (EV) will make sure the photos are always correctly exposed. The camera automatically adjusts to expose images precisely for each scene combining darkness and lightness. On Auto mode, the camera set a brightness somewhere between the brightest and darkest areas. This causes problems when the entire image is very bright, or very dark. To fix this, the EV was set manually to the value at a higher or lower setting than was automatically set. For very bright settings, the EV should be a positive number and for very dark scenes, the EV should be a negative number. In this work, the negative EV worked better and after trying different values the optimum value was set to -2. Another option is Metering, which is how the camera coordinates the correct shutter speed and aperture, depending on the amount of light that goes into the camera and the sensitivity of the sensor. The Evaluative Metering mode divides the entire frame into multiple regions and analyses each of them based on lightness and darkness. One of the key factors, other than the above-mentioned factors, affecting the matrix metering is the camera focus point. After gathering the information from all individual regions, the metering system highlights the box at the focus point and emphasizes it over all other zones. The focus point was always on the sample cross section. An auto white balance (AWB) setting was chosen to automatically adjust the white balance when capturing a photo.

Name:	**Atieh Motaghi**
Post-Secondary education and degrees:	Amir Kabir University of Technology (Tehran Polytechnic) Tehran, Iran 1998-2002 B.Sc. University of Tehran Tehran, Iran 2009-2011 M.Sc. The University of Western Ontario London, Ontario, Canada 2012-2018 Ph.D.
Related work experience	Teaching Assistant The University of Western Ontario 2011-2017 Research and Development engineer Karan Abar Baspar Engineering Materials Co. Tehran, Iran 2004-2007 Quality Control Engineer Saipa Azin Co. Tehran, Iran 2003-2004
Publications	A. Motaghi, A. N. Hrymak Microstructure characterization in direct sheet molding compound Polymer Composites July 2017 A. Motaghi, A. N. Hrymak, G. Hashemi Motlagh Electrical conductivity and percolation threshold of hybrid carbon/polymer composites Journal of Applied Polymer Science Vol. 132, Issue 13, 2015